Politecnico di Milano

School of Industrial and Information Engineering

Master of Science in Nuclear Engineering

The PuO_2 – Fe_3O_4 system melting behaviour: an experimental analysis

Author:

Luca Casini

Matr. 901450

Supervisor:

Prof. Lelio Luzzi

Co-supervisor:

Luka Vlahovich

Academic Year 2020/2021

October 2021, Milan

Non chi comincia,
ma quel che persevera.

Contents

Acknowledgements

As for every journey there is no possibility of success without support from many people, each person that I encountered gave his contribution to this day, so I will start by saying thank you to all of those people who are not explicitly mentioned here.

Firstly, I am grateful to the European Commission which trough the INSPYRE project 2014 – 2018 (#754329) has financed this research and my experience at the Joint Research Centre of Karlsruhe (JRC-KRU) in Germany, it was a pivotal point in my career, a milestone I'm very proud of, and a period of my life that I will never forget.

Then I would like to say a sincere thank you to all my mentors. The first being prof. Luzzi for his guidance and his trust in me, he was an invisible hand guiding my steps towards the goal I set for myself. In the troublesome journey I had in university he really felt like a safe dock in times of storm.

I'm also extremely grateful to my German supervisors, Luka Vlahovich and Davide Robba. The amount of faith they had in me is beyond describable, I had both the privilege to choose myself which mistakes to make, and the luck of having them helping to fix them.

Next, is time to show my gratitude to all my family for the never-ending support I received through these years, especially my parents. More than the economic one, the moral encouragement, the constant push not to surrender, and the unfadable examples of honesty and diligence were a beacon of light I always aimed towards in these years. Then I'd like to say thank you to my brother for the countless teachings he gave me in life, whose determination and perseverance against challenges were an inspiration more often than what he thinks. Not only, his moral sustain in times of troubles was an essential step on this ladder, and something I wish one day to pay back. To my grandparents, my

uncles and aunts, who were an example of integrity, and to all the rest of my family, thank you.

Now it's time for all the people I met in this long journey. Starting from where this journey began, 26 years ago, thank you Giancarlo for being on my side since we were born, I had to wait 5 days for you, but I've almost forgiven you for that, we went through everything together and I'm grateful of this every single day. I have an immense debt of gratitude with Francesca, with her constant presence and support (especially in the form of food) she quite literally pulled that leafed crown on my head. I always say that bad luck walks with me, but you were truly a gift I'm not sure yet I deserve, thank you for everything. To my dear friends, Ale, Zano, and Otta, our friendship was as much unexpected as it was a blessing. With you I had the time of my life and felt the joy of being your truly self and accepted for that. It really is something everyone should experience once in life, and surely not something distance could kill, some of you are oceans apart, but our bond will never fade. One special thank goes to Mattia, the number of dumb decisions we made together is countless, yet your friendship and support to me was as precious as a Mutti can in times of need.

To all of you, and to all of those I forgot or omitted for brevity go my most sincere and deep gratitude on this wonderful day.

Abstract

The main purpose of this thesis work is the experimental determination of the phases that would form at high temperature following nuclear fuel – steel cladding interaction. The main driver to this research project was the lack of specialised literature in such a relevant area of development of Gen IV nuclear reactors. This goal was pursued by means of laser – optical thermometry at JRC – Karlsruhe, resulting in the phase diagram experimental determination for the PuO_2 – Fe_3O_4 system reported in this work.

The first result consisted in the successful fabrication of pellets containing various concentrations of Pu and Fe over the whole composition range. Sample characterisation was performed both on fresh and molten samples to investigate structural changes following melting experiments via SEM and XRD.

The experimental setup was then assembled, calibrated, and aligned together with a precise estimation of experimental uncertainties. Another fundamental result obtained in the framework of this thesis is the successful implementation and exploitation of an oxygen analyser during melting point assessment. This device allowed for the first time to determine the influence of atmosphere during measures and enhanced our understanding of relevant undergoing phenomena related to oxidation states.

This influence was shown to be non-negligible during melting, thus data collected in this work will pave the design stage of future nuclear reactors against accidental scenarios.

Sommario

Lo scopo principale di questo lavoro di tesi è la determinazione sperimentale delle fasi che si formerebbero ad alta temperatura in seguito all'interazione del combustibile nucleare con la guaina in acciaio. Il motore principale di questo progetto di ricerca è stata la mancanza di letteratura specializzata in un'area così rilevante per lo sviluppo di reattori nucleari di IV generazione. Questo obiettivo è stato perseguito per mezzo di termometria laser - ottica al JRC di Karlsruhe, con conseguente determinazione sperimentale del diagramma di fase per il sistema PuO_2 - Fe_3O_4 riportato in questa tesi.

Il primo traguardo di questo lavoro è consistito nella fabbricazione con successo di pastiglie contenenti varie concentrazioni di Pu e Fe nell'intero intervallo di composizioni. La caratterizzazione dei campioni è stata eseguita sia su pastiglie fresche che fuse, per studiare i cambiamenti strutturali in seguito alle alte temperature, tramite SEM e XRD.

L'apparato sperimentale è stato poi assemblato, calibrato e allineato insieme a una stima precisa delle incertezze di misura. Un altro risultato fondamentale ottenuto nell'ambito di questa tesi è l'implementazione e lo sfruttamento con successo di un rilevatore di ossigeno durante la fase sperimentale. Questo dispositivo ha permesso per la prima volta di determinare l'influenza dell'atmosfera durante le misure, e ha migliorato la nostra comprensione dei fenomeni di ossidazione e riduzione durante il cambiamento di fase. Influenza che si è dimostrata non trascurabile, e i cui dati raccolti in questo lavoro svolgeranno un ruolo chiave durante la fase di progettazione dei futuri reattori nucleari, per via dell'importante riduzione del punto di fusione osservata.

Symbols and abbreviations:

EDS	Energy Dispersive x-ray Spectroscopy
I.S.	International System for units of measure
JRC	Joint Research Centre
n	Moles
NPP	Nuclear Power Plant
MOX	Mixed Oxide
PD	Phase Diagram
p	Pressure
$p(O_2)$	Partial pressure of oxygen
P&I	Piping and Instrumentation
PT	Phase Transition
PTT	Phase Transition Temperature
Pu	Plutonium
PuO_2	Plutonium Dioxide
RLS	Reflected Light Signal
SA	Severe Accident
SEM	Scanning Electron Microscopy
SS	Sum of Squares
T	Temperature
TD	Theoretical Density
TEM	Tunnel Effect Microscopy
XRD	X-Ray Diffraction
v	Volume
wt%	Weight percentage

List of figures

List of tables

Estratto in italiano

Introduzione

Il ruolo dell'energia nucleare nel panorama energetico mondiale, sin dalla sua creazione, è sempre stato di primaria importanza. Oggi più che mai essa è un fulcro di ricerca, soprattutto nel contesto dello sviluppo di reattori nucleari veloci di IV generazione [1]. Il principale tipo di combustibile che ci si aspetta possa operare all'interno di questi reattori, infatti, è il *Mixed OXide fuel* (MOX), la cui caratteristica principale è la presenza di plutonio come elemento fissile [1]. Data l'assenza di una letteratura dettagliata riguardante le proprietà del MOX, la Commissione Europea, in concerto con il *Joint Research Centre* (JRC) di Karlsruhe, ha commissionato un'indagine a questo proposito nell'ambito del progetto H2020 INSPYRE (http://www.eera-jpnm.eu/inspyre/). L'obbiettivo ultimo di questa tesi consiste pertanto nella determinazione sperimentale delle proprietà termodinamiche del sistema PuO_2 – Fe_3O_4, al fine di fornire dati sull'interazione tra combustibile e guaina ad alte temperature, fondamentali per lo sviluppo e il progetto di reattori innovativi in un'ottica di prevenzione e contenimento di eventi incidentali [2] [3].

Preparazione dei campioni

Il primo traguardo di questa tesi consiste nella fabbricazione di pastiglie idonee alla sperimentazione. Al fine di indagare l'intero spettro di composizioni sono state fabbricate 4 serie di campioni a differenti concentrazioni, rispettivamente 20, 40, 60 e 80 at% Pu dove la percentuale è stata calcolata come rapporto il numero di atomi di Pu rispetto al totale di soli atomi pesanti (Pu + Fe) presenti nel campione. Questa scelta è stata dettata dalla necessità di ridurre gli effetti della forte riduzione prevista nei campioni sottoposti ad alte temperature. Essendo obbiettivo ultimo di questa tesi il diagramma di fase della miscela in

considerazione, la scelta menzionata riduce al minimo eventuali incertezze sulla composizione in fase di misura in caso di interazione ossidante o riducente con l'atmosfera [4] [5].

La fabbricazione dei campioni è avvenuta tramite pressatura delle relative polveri all'interno di una scatola a guanti in ambiente inerte (N_2), all'interno della zona controllata dell'istituto JRC - Karlsruhe. Al fine di migliorare le caratteristiche meccaniche dei campioni si è reso necessario un processo di sinterizzazione ad alta temperatura, il quale ha permesso di ottenere campioni stabili e idonei alla sperimentazione. I campioni sono stati inoltre sottoposti a caratterizzazione pre- e post- fusione tramite XRD e SEM, al fine di identificare i cambiamenti di struttura nella pastiglia.

Apparato sperimentale

Un altro importante traguardo di questo lavoro di tesi consiste nel perfezionamento dell'apparato sperimentale presso il JRC – Karlsruhe, descritto in [6].

Questo apparato, utilizzato per la misura del punto di fusione di composti alto-fondenti tramite termometria ottica e laser, è stato ammodernato tramite l'aggiunta di un nuovo impianto di misura in grado di quantificare anche la presenza di ossigeno nell'ambiente sperimentale. Quest'ultima, come accennato, è una grandezza di primaria importanza data la sua forte influenza sulla misura [7] [4].

Pertanto, l'apparato sperimentale era costituito da un laser ad alta potenza, uno a bassa potenza, uno spettrometro a 256 canali, un pirometro ultraveloce a due canali, il rilevatore di ossigeno, la relativa catena di acquisizione elettronica e un contenitore in acciaio con finestre di trasmissività nota. La procedura sperimentale consisteva nel fornire energia al campione tramite brevi impulsi del laser ad alta potenza, e la successiva misura delle proprietà termodinamiche

tramite lo spettrometro, il pirometro e il laser a bassa potenza. Il primo ha fornito informazioni sull'emissività del campione, mentre il secondo ha registrato le variazioni di temperatura del campione con risoluzione sufficiente ad evidenziare i fenomeni d'interesse. Il laser a bassa potenza è stato usato per determinare con precisione il punto di transizione di fase all'interno del termogramma fornito dal pirometro sfruttando il cosiddetto *Reflected Light Signal method* [8] [9].

Risultati sperimentali

La misura dei punti di transizione di fase è stata effettuata su tutte le composizioni sia in ambiente ossidante (aria), sia inerte (argon), al fine di determinare l'influenza dell'atmosfera sperimentale sulla misura stessa.

Ciò che è risultato subito evidente è che mentre la rilevazione dei punti di transizione di fase risulta ripetibile in aria, questo non accade in argon, il motivo è stato attribuito ad una riduzione del campione ad alta temperatura in ambiente povero di ossigeno. Quello che si osserva è un andamento strettamente decrescente dei punti di *liquidus* e *solidus* misura dopo misura, fino a una stabilizzazione dopo 4 – 5 impulsi. In particolare, è stato osservato che l'effetto della riduzione dipende dalla concentrazione del campione. Campioni ricchi di plutonio hanno mostrato forti variazioni del punto di *liquidus* dopo ogni rilevazione, mentre il *solidus* è stato alterato in misura minore. Viceversa, campioni poveri di plutonio e ricchi di ferro hanno evidenziato variazioni più marcate nella misura del punto di *solidus*, mentre il *liquidus* ha subito scostamenti di minor entità.

Il rilevatore di ossigeno ha quindi giocato un ruolo fondamentale nello spiegare questo fenomeno nel dettaglio. Esaminando le misure della pressione parziale di O_2 nell'atmosfera della camera si osserva chiaramente un picco in corrispondenza di ogni misura, ciascuno ad intensità minore del precedente e maggiore del

successivo, fino a un valore che diventa ripetibile. Il rilascio di ossigeno da parte del campione è stato quindi appurato sperimentalmente e quantificato andando a calcolare la quantità di ossigeno emessa sfruttando l'area del picco. Questa stima ha permesso di evidenziare un altro dato interessante: l'andamento del rilascio segue un profilo quasi esponenziale impulso dopo impulso, fino a un valore stazionario, ripetibile e indipendente dalla concentrazione del campione. Questo sembra suggerire una dinamica di rilascio dell'ossigeno influenzata maggiormente dalla breve permanenza ad alta temperatura, piuttosto che dalla composizione chimica del campione. Inoltre, questo comportamento è coerente con la variazione osservata nella temperatura di transizione di fase, che si osserva stabilizzarsi dopo poche misure.

Conclusioni

Il risultato principale di questa tesi consta nella determinazione sperimentale del diagramma di fase per il sistema PuO_2 – Fe_3O_4, un punto chiave per lo sviluppo dei reattori di IV generazione [1]. In particolare, si è rilevata la presenza di un punto di eutettico, identificato anche al SEM, intorno al 10 at% Pu, coerentemente con la letteratura di sistemi simili [5] [4].

Rilevante traguardo è inoltre la rilevazione del contenuto di ossigeno nell'ambiente di misura e della relativa valutazione dell'influenza data dall'atmosfera all'interno della camera nella determinazione del punto di fusione con tecniche di termometria ottica e laser.

I risultati delle analisi sperimentali sono raccolti nel diagramma di fase riportato di seguito.

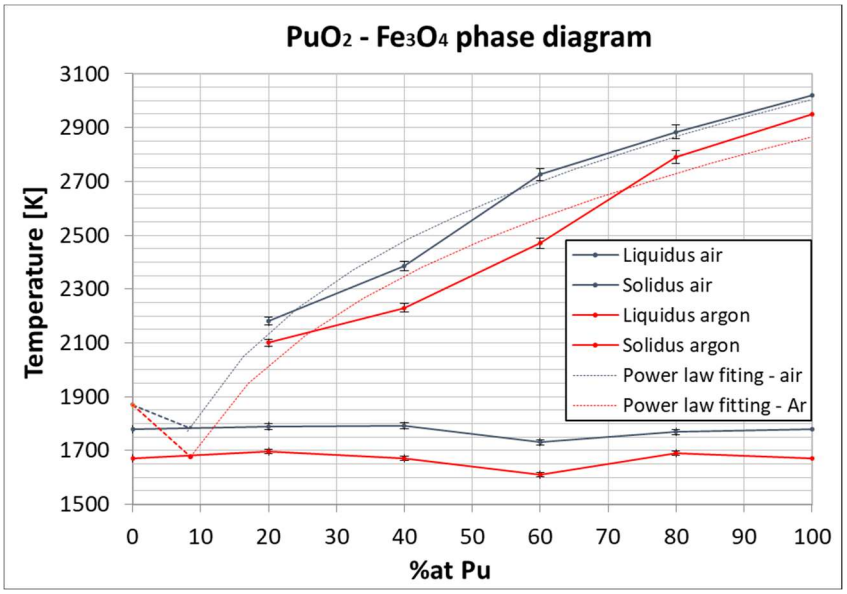

Figura 2: Diagramma di fase sperimentale per il sistema PuO_2 - Fe_3O_4

È opportuno notare l'effetto non trascurabile della riduzione dei punti di transizione di fase, con uno scostamento verso il basso dell'ambiente riducente di diverse decine (talvolta centinaia) di K. Si osserva anche la presenza di un punto di eutettico, la cui esistenza è stata anche confermata dall'analisi SEM, che ha mostrato la presenza di strutture eutettiche caratteristiche, come lo sviluppo di solidificazione dendritico e una disposizione lamellare delle fasi al suo interno. Questo era un risultato atteso, data la similitudine con altri sistemi già trattati in letteratura [5] [4]. È doveroso inoltre sottolineare che il presente diagramma di fase rappresenta principalmente un aiuto visivo per l'identificazione del comportamento generale del sistema in considerazione. Data la presenza di riduzione considerevole nel campione una rappresentazione più adeguata sarebbe data da un diagramma ternario Pu - O – Fe ottenuto per via numerica e validato dai dati sperimentali di qui riportati. Proprio questo punto presenta notevoli opportunità di sviluppo futuro di questo lavoro di tesi.

Extended Summary

Abstract

The main purpose of this work is the experimental characterisation of the Pu – Fe – O system under the INSPYRE project for the European Commission at JRC Karlsruhe. This proved to be a subject of primary importance in the development of generation IV nuclear reactors [1], especially for deeper understanding and prevention of severe accidents [2] [3]. Particular focus was given on the phases that would form in case of melting between the MOX nuclear fuel and the steel cladding investigated by means of laser – optical thermometry, since the interaction of steel and common fissile material was already assessed [5] [4]. The detailed declination of this task will be explained briefly in the present summary and extensively in the thesis's body, where the description of the experimental process as well as the most relevant results will be carried on.

Sample preparation

In the framework of this thesis, round shaped thin pellets were produced by intimately mixing iron oxide and PuO_2 powders in different relative concentrations. The obtained specimens had to be tough enough to withstand numerous repeated laser shots during laser melting experiments. Since plutonium and iron oxides have very different microscopic structures and thermal properties, simultaneous sintering would induce stress because of different relative shrinking effects, which would overcome the enhanced strength due to increased density. Particularly, Fe_2O_3 is expected to modify its structure during sintering from rhombohedral to the close packed cubic lattice typical of spinels. In order to minimize these effects, and obtain sufficiently dense and resistant samples, Fe_3O_4 powder to be pressed was produced at first, by pre-heating pure Fe_2O_3 in a furnace under Argon flux. Almost stoichiometric Fe_3O_4 was obtained, with only a negligible amount of over-reduction in FeO, as estimated using XRD.

The pure Fe_3O_4 powder was then mixed in suitable proportions with PuO_2 to obtain four different sample batches having compositions of 20, 40, 60 and 80 at% of the ratio Pu/(Pu+Fe) in metal form. Samples belonging to the different batches will be shortly indicated in the following as 20Pu, 40Pu, 60Pu and 80Pu. The choice of relying on metals

at% and not mol% of oxides was dictated by the high amount of reduction expected in the samples during heating [7], thus ensuring much lower uncertainties on composition during phase diagram determination because of the smaller volatility of metals compared to oxygen.

After mixing and milling in a mortar, in order to reduce inhomogeneities and decrease particle sizes to the order of tenths of microns, about 250 mg of mixture for each sample was pressed. Zinc stearate was added in small amounts as a lubricant in the mixture before pressing, so to reduce friction during pellet movement in the channel. This process delivered pellets stable enough to be handled and moved to the adjacent oven for sintering in Ar atmosphere for 3 hours. The zinc stearate completely evaporated at this stage, leaving no trace of contamination, as checked with XRD. After sintering, the recorded density proved to be around 90% of the theoretical density for all disks, at the end of the process disks appeared to be solid and almost black, even if some small cracks could be spotted by eye on the surfaces. Preliminary SEM microscopy characterization confirmed the presence of porosities and small cracks inside the sintered pellets. Sample characterisation was performed both on fresh and laser molten samples by means of SEM analysis as described later in section 2.2.1.

Laser melting experimental set-up

Laser melting experiments were performed in the laboratories of JRC Karlsruhe using the experimental set-up showed in Ch. 2 and described in detail in [10].

Inside the N_2 - filled glove box, a stainless-steel containment vessel was designed to accommodate the sample and maintain it in a constant gas flux of Ar or clean air during the experiments, at about 3 bar overpressure, in order to partially suppress evaporation during melting. A highly pure sapphire window and an optical window (BK7 optical glass) were installed on the pressure vessel and on the glovebox wall respectively.

A Nd:YAG laser model TRUMPF HD 4506 was connected with fibre optics to deliver laser pulses at 1064 nm (minimum duration of 1ms) through suitable optics, aiming directly at the sample. A power of 1 kW with a spot diameter of 4.8 mm for a duration of about 500ms was sufficient to produce a molten pool of about 2 mm -3 mm diameter at the center of the sample. In order to attain self-crucible conditions on the samples,

specific graphite sample holders with graphite screws were used. An HD camera featuring x10 optical zoom was used to follow the experiment from the control room, permitting to view variations of the molten area after each laser shot. Because of the intense power delivered on the sample, the intensity of the reflected light beams cannot be neglected and graphite absorbers must be properly positioned, both outside and inside the glove box in order to prevent damages at the facility.

A second "probe laser" emitting with a lower power at 488 nm (bright blue light) was aimed to the sample and reflected by its surface. This reflected laser signal was used to detect changes induced by phase transitions occurring on the surface during the experiments as described in section 2.3.2.

The radiation emitted by the sample and the reflected blue beam are detected at the same time using a two-channels fast pyrometer, whose main channel (λ = 650 nm) was calibrated up to 2500 K using standard reference tungsten ribbon lamps.

The second channel was set at 488 nm, matching the wavelength of the blue laser and thus allowing to monitor the relative intensity of the signal reflected from the sample surface. Using the so-called Reflected Light Signal method (RLS) it is possible to precisely relate the derivative of such signal to the instant of occurrence of a phase change on the sample surface, as described in [10] [8]. Temperature was then obtained via Plank's law of radiation, corrected properly with the relative emissivity.

In the present work emissivity of the sample at the melting point was measured using a multi-wavelength spectrometer, similarly to previous works [11]. Data analysis is performed by exploiting the linearity of the inverse of radiance temperature as a function of wavelength λ, i.e. using Wien's approximation of Planck's law:

$$\frac{1}{T_\lambda} = \frac{1}{T} - \frac{\lambda}{c_2} ln(\tau\varepsilon)$$

Where c_2 is the second radiative constant, T is the true temperature, T_λ is the radiance temperature at wavelength λ and τ is the optical path transmittance. This approximation has been demonstrated to be acceptably accurate in refractory materials [12], like those usually present in a nuclear reactor, for which emissivity can be assumed to be wavelength-independent (grey body hypothesis) on a broad spectral range, a detailed dissertation can be found in section 2.3.2.

Nonetheless, the true melting temperature T_m was then obtained directly from the first channel of the fast pyrometer rather than the linearization process, which has a much lower time resolution and was used solely for emissivity estimation.

An additional feature of the experimental set-up used in this work consists of the capability of monitoring the variations of oxygen content in the autoclave atmosphere during laser melting measurements performed in an Ar flux. To this purpose, an O_2 monitoring device (Setnag Gen'Air) was used, which is capable of detecting small oxygen partial pressure ($p(O_2)$) changes in the gas exiting from the pressure vessel. It is thus possible to investigate whether the sample is gaining or losing oxygen in the specified environment and estimate the amount of oxygen evolved during the melting process.

The working principle of the instrument is based on Nernst equation (below), that gives the voltage at the two sides of an oxygen ion conductor, separating two environments with different $p(O_2)$.

$$\Delta E = \frac{RT}{4F} ln\left(\frac{p_{O_2}}{pref}\right)$$

Where:

ΔE is the induced voltage,

R the gas constant,

T the temperature,

F the Faraday constant,

P_{O2} and P_{ref} are the two O_2 partial pressures (the second taken as reference).

$P(O_2)$ profiles were recorded for about 20 to 40 min after each laser shot, until the complete return to the base $P(O_2)$ level. An estimation of the total relative oxygen release during sample melting was then obtained by integration of the $P(O_2)$ profiles and available in section 3.4.2.

Experimental results

Emissivity of the PuO_2-Fe_3O_4 system

In figure 0.1, a thermogram measured during a laser melting experiment (in air) of sample 40Pu is reported together with the surface emissivity profile obtained by linear fitting of the simultaneously acquired multi-wavelength spectrum described previously. Two different regions are evident, in which emissivity assumes different values: the first at higher T, when the sample surface is completely melted, and the second after the ending of laser heating. The two regions are separated by some scattered values, corresponding to the end of the laser shot, when the temperature is decreasing too quickly for the multi-channel spectrometer to yield meaningful emissivity data.

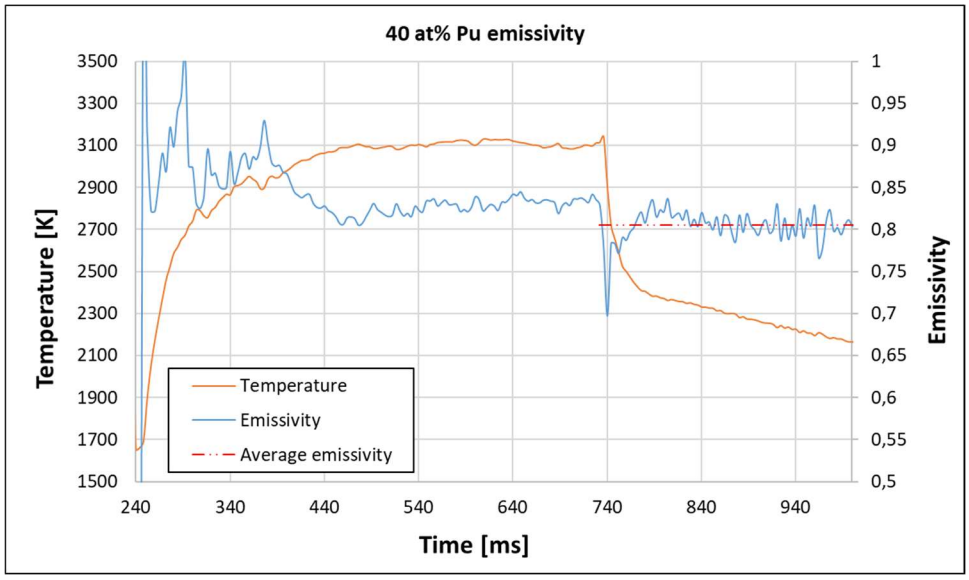

Figure 0.1: Temperature and emissivity of the 40 at% Pu recorded by the spectrometer.

It is important to notice that after the first thermal plateau and during the whole-time range of solidification, the sample emissivity assumes almost constant values, until the temperature reaches values lower than about 2000 K and consequently the emissivity profile starts to become too noisy and therefore unreliable. Constant emissivity values during solidification have been steadily observed throughout this work, also for samples having different concentrations, both for treatments in air and in Ar. Accordingly, the reference value was obtained as the average measured after the end of the laser pulse, this value has been taken as representative of the emissivity of that sample in the whole solidification temperature range. This procedure delivered repeatable results

throughout the entire measurement process, with statistical deviations coherent with the uncertainties estimations, reported in section 2.4.

From these measurements the PuO_2-Fe_3O_4 system has shown an almost linear dependence of emissivity with Pu concentration, with intermediate concentrations having intermediate values of emissivity compared with the pure oxides, coherently with a linear Vegard's law interpretation.

Laser melting experiments in air

Figure 0.2 shows the thermograms of the 40Pu sample exposed to air flux during laser melting. A laser pulse of 0.5 sec was used to produce a rapid temperature increase, which led to melting of a small area at the center of the sample. After the laser shot, during the rapid cooling of the sample two successive solidification transitions can be observed at around 2400 K and 1800 K, which are assigned to the liquidus and the solidus point, respectively.

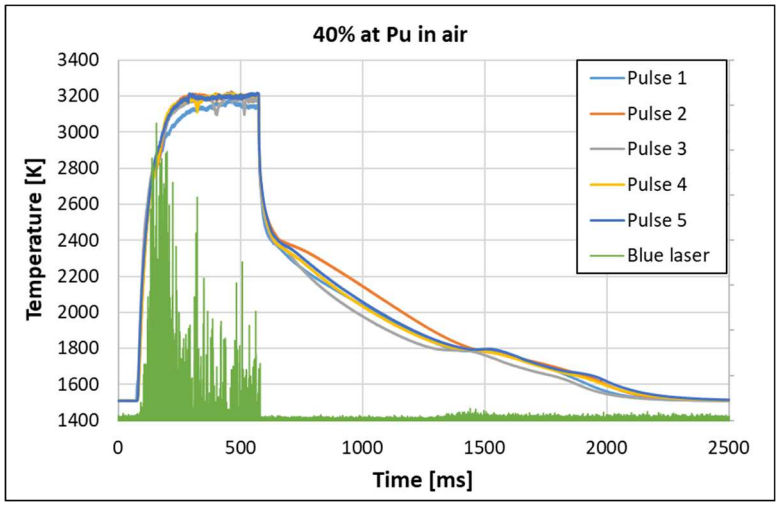

Figure 0.2: Thermograms relative to 40Pu recorded in air, the blue laser signal is also reported.

In order to precisely determine the two-phase transition temperatures (PTTs) three different methods have been used in this work as described in section 2.3.2 and 2.4 as advised by literature [10]. Wherever a horizontal plateau or even an undercooling shoulder was well visible, its position was taken as the best reference for a PTT determination. This maximum often corresponds to an evident peak of the blue laser derivative, further identifying the same transition with the RLS method. This approach aimed at identifying the instant of phase transition exploiting the sudden change in

reflectivity between different phases. This variation in reflectivity will appear as a sharp change observed in the reflected light signal intensity in correspondence of the PTT. Therefore, when an undercooling shoulder was not clearly evident, the RLS method alone was used, which showed high sensitivity, too. Unfortunately, the RLS technique is strongly affected by unpredictable surface reflectivity changes, thus is not always able to provide accurate results for all laser shots. In all cases, the point of first slope change of the temperature versus time curve was used to determine the corresponding PTT (generally a solidus transition).

In the same figure, the thermograms obtained with five subsequent laser shots in air on the same 40Pu sample are reported. It can be observed that the shapes of these thermograms are not exactly identical, primarily due to the sample surface modifications induced by laser melting itself, like the increasingly growing dimension of the melted zone (which is obviously not present for the first shot) and the possible onset of small cracks in the sample. Other thermal kinetic effects, like small variations in the thermal resistance at the contacts with the graphite screws, can easily distort the recorded signal too.

Despite these differences, the thermal profiles magnifications shown in figure 0.3 are almost coincident in correspondence of the two thermal arrests, that fall inside relatively narrow scatter bands, regardless of the pulse order, thus making the PTT determination, for samples melted in air, closely repeatable for consecutive laser shots.

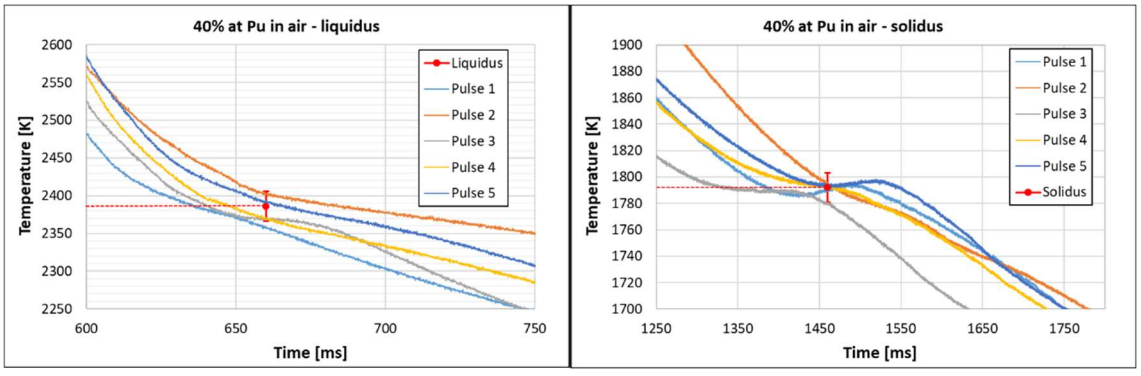

Figure 0.3: Solidus and Liquidus PTT relative to the 40Pu composition in air.

Practically, the PTTs measured from all the shots of 40Pu sample in air have the same value, within the measurement precision. Dashed lines in the figure help identifying the

PTTs relative to the small undercooling shoulders: for liquidus point 2386 K ± 17 K is considered to be the PTT reference value, while for solidus point a value of 1792 K ± 11 K is obtained.

For all the four different compositions measured in air (20, 40, 60 and 80Pu) analogous results have been obtained, where PTT values, measured by repeated consecutive shots, were found identical within the experimental error for both thermal transitions. All PTT values measured in air have been reported in Table 0.1, together with the summary of the more complicated results obtained by laser melting in inert Ar atmosphere, which are described in the next paragraph and section 3.4.2.

It is worth noting here that error values reported for melting experiments in air, when repetition of consecutive measurements does not essentially alter the result, have been calculated as standard deviation of repeated measurements. On the contrary, for melting experiments in Ar, where single laser pulses showed to be non repeatable, the error values are the theoretical uncertainty, calculated as a function of T, by using the standard error propagation theory.

Laser melting experiments in Ar

Fig. 0.4 shows six consecutive thermograms recorded during laser melting in Ar flux for a sample with the 40Pu composition.

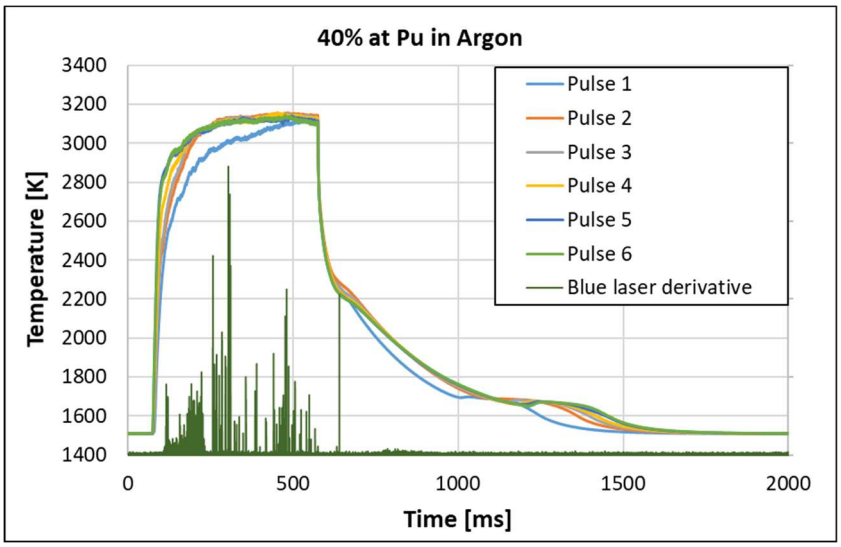

Figure 0.4: Thermograms relative to 40Pu recorded in argon, the blue laser signal is also reported.

Although the overall outgoing is close to the one measured in air, several interesting differences appear, firstly, evident systematic variations can be observed between the different consecutive thermograms in close proximity of both PTTs. This observation is further evidenced in figure 0.5, where the solidus PTT is reported. It appears that in inert atmosphere the undercooling shoulders are not randomly scattered, the first one being instead at a higher temperature than the following ones, with a strictly decreasing order, until a "stationary PTT" is reached, usually after 4-5 laser pulses. The difference between the first and the last pulse is 30 K (varying for each composition, as reported in table 0.1), and is not negligible compared to the experimental uncertainty. Moreover, since the thermal arrest temperatures were repeatable only once equilibrium was reached, only the last laser pulse was taken as representative of a fully-reduced sample.

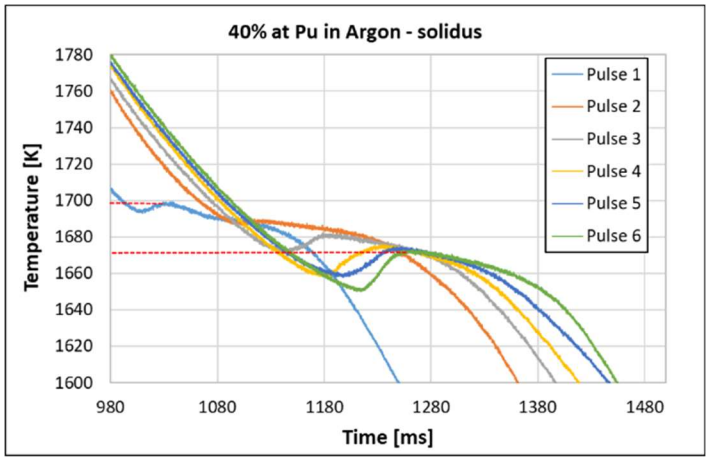

Figure 0.5: Solidus PTT relative to the 40Pu composition in Ar.

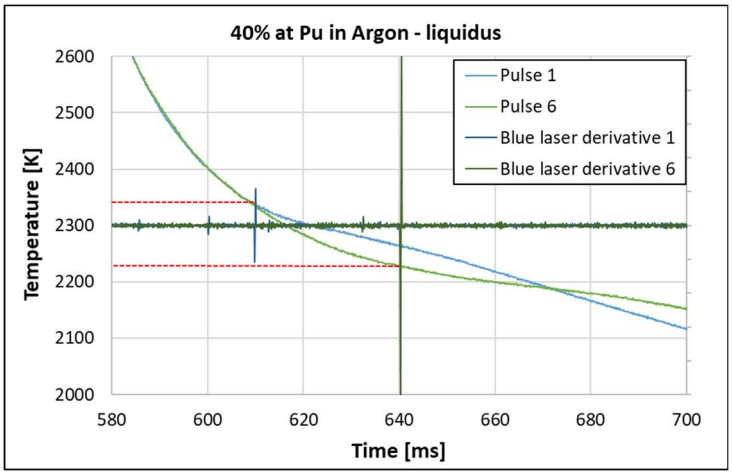

Figure 0.6: Liquidus PTT relative to the 40Pu composition in Ar, obtained exploiting the RLS technique.

Analogous results were obtained for the liquidus point, as shown in Fig. 0.6, where, for the sake of clarity, only the thermograms of Pulse 1 and 6 are plotted together with their respective RLS signals. In this case PTT values have been evaluated by exploiting the RLS method, due to the lack of evident undercooling shoulders. Using all the RLS peaks, the progressive decreasing of PTT can be highlighted also for the liquidus point, with almost 100 K of difference between the first and last laser shot.

The same effect was also observed for all the other compositions as reported in section 3.4 and appendix A. The intensity of the PTT value decrease in successive laser shots was found to be greater on the liquidus or on the solidus PTTs, depending on the Pu concentration of the sample. Pu richer batches show remarkable reduction effects in liquidus point, with lower influence on the solidus; conversely, Pu poorer samples show considerable reduction effects on solidus point, with smaller impact on the liquidus.

The observation of progressively decreasing PTT values after successive laser shots in Ar suggests that, due to the low oxygen potential of the inert environment, the melted portion of the sample is losing oxygen atoms, thus modifying its stoichiometry and progressively undergoing a chemical reduction until a more stable reduced phase is formed, which is characterised by a lower PTT.

The hypothesis of a progressive sample reduction during successive laser heating and cooling cycles has been confirmed by the analysis of oxygen content in the Ar flux performed here for the first time and reported in figure 0.7.

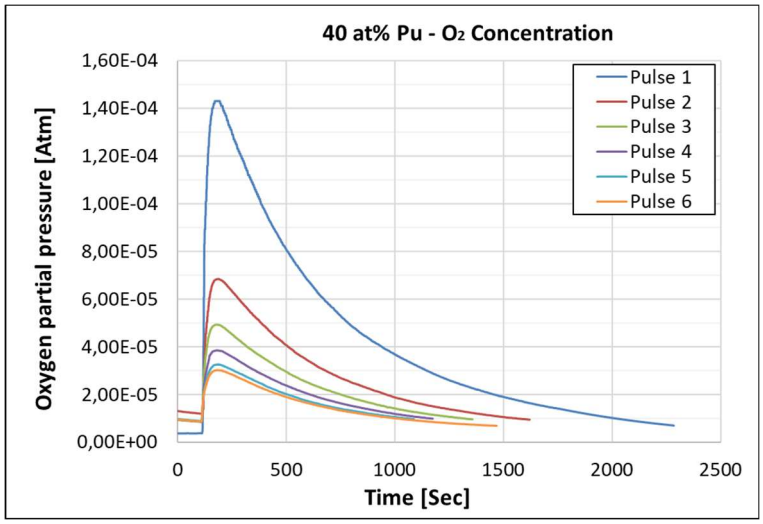

Figure 0.7: collection of the oxygen partial pressure profiles shortly after each laser pulse in argon.

Oxygen partial pressure was recorded after each pulse, showing a clear peak after each shot, with a fixed time delay. The intensity of the maximum of $P(O_2)$ profiles shows a strictly decreasing behaviour down to a stationary value, analogous to the behaviour observed for the temperature shift of PTTs. The presence of oxygen in the flow has been attributed to a release of oxygen due to chemical reduction of the sample surface at very high temperature. The intensity of the total amount of oxygen released during each shot has been estimated by calculating the area of the $P(O_2)$ peaks. The outcome is very close to a decreasing exponential, where the reducing effect is decreasing until is almost no longer observable. The same qualitative behaviour of oxygen release is shown for all experiments in Ar atmosphere, regardless of sample composition. In particular, similar saturation values were observed, close to 5 ÷10 μg of oxygen released, suggesting a fast, time-driven mechanics, rather than chemical dependence only.

It was observed that as soon as equilibrium is reached in the sample, measurements could be repeated, delivering reproducible results representative of the reduced effect of the environment on the sample. For this reason, in inert atmosphere, only the last pulses are considered as relevant for the PTT determination.

Conclusions

The present work represents the first step into deeper understanding of the interaction between fuel – cladding interaction at high temperatures for Gen. IV nuclear reactors.

PTTs of a wide range of composition were assessed by means of optical thermometry, while introducing for the first time the analysis on the influence of atmosphere on melting point assessment.

All the experimental results were gathered here and reported in table 0.1. It is important to point out that figure 0.8 reports a plot of the current experimental points on an isopleth PuO_2-Fe_3O_4 plane, for an optimised readability.

Table 0. 1: Summary of PTTs for all composition in both atmospheres.

Transition point	Sample [at%Pu]	melting in **air**		Melting in **argon**		
		PT temperature [K]	N° shots	PT temperature [K]	ΔT max [K]	N° shots
liquidus	20	2180 ± 14	3	2100 ± 14	10	4
	40	2386 ± 17	5	2230 ± 15	100	6
	60	2725 ± 22	6	2470 ± 18	135	6
	80	2884 ± 25	4	2790 ± 23	95	5
solidus	20	1790 ± 10	3	1696 ± 9	70	6
	40	1792 ± 11	5	1671 ± 9	30	6
	60	1731 ± 10	6	1610 ± 8	20	6
	80	1769 ± 10	4	1690 ± 9	10	5

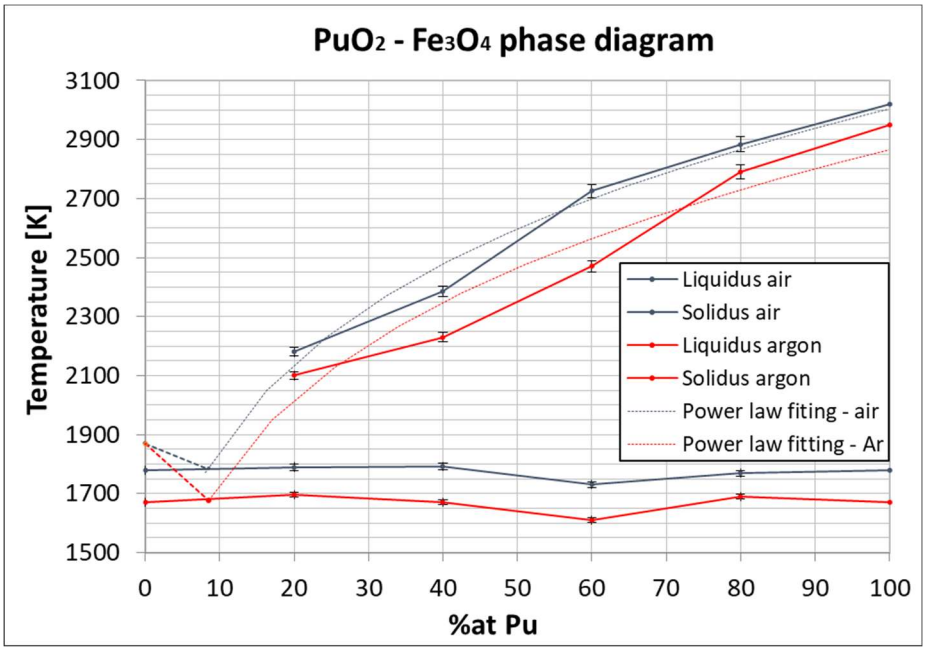

Figure 0.8: Preliminary phase diagram for the PuO_2-Fe_3O_4 system.

Since oxidation changes were actually observed in the laser heated samples, the present experimental points would be more accurately represented in the ternary Pu-Fe-O diagram. To obtain a more precise and accurate description, further developments of this work would take advantage of thermodynamic calculations in order to determine a ternary diagram for the Pu – Fe – O system.

1. Introduction

The general objective of this research project is to predict the phases that form during the chemical interaction between the mixed-oxide (MOX) fuel and the fast reactor steel cladding beyond 1700 K, including therefore melted steel. The project is part of a broader initiative named INSPYRE constituted by the European Commission, aimed at understanding the interactions occurring between MOX fuel, B_4C and steel at temperatures close to the melting transition. The most exhaustive study in this domain was performed by Kleykamp on the phase equilibria in the UO_2-austenitic steel system up to 3000°C [13]. However, no data exist on the MOX-Fe system, which, besides their intrinsic scientific interest, are essential for the safety assessment of fast neutron reactors. Reactors of this kind are actually envisaged as Generation IV nuclear plant systems [1], with particular advantages in terms of fuel efficiency, plutonium and minor-actinide burning and, as a consequence, a large reduction of the long-term nuclear waste radioactivity. Fast-neutron reactors will burn fuel elements containing between 10 mol % and 30 mol % of Pu, i.e. up to ten times as much plutonium as thermal reactor fuels. The oxide fuel option in particular is currently more advanced and viable for the near future compared to other fuel concepts, like for example carbide, nitride or metal fuels.

The most common severe accidents (SAs) that can occur in a water-cooled nuclear power plant (NPP) stems from a leakage of coolant, resulting in overheating and melting of the reactor core [2] [3]. This can result in the formation of a liquid, lava-like mixture of nuclear fuel, cladding and structural materials usually referred to as “corium”. This hot, highly radioactive mixture can diffuse outside the primary containment if the steel wall is melted through and end up reacting even with the concrete constituting the most external barrier. The extreme heat and the high reactivity of the species present in corium can lead

to water dissociation and the production of hydrogen. This might result in an additional risk of steam and hydrogen explosions, but also to heavy oxidation of the corium mass and the NPP structural materials, and obvious possible release of highly radioactive materials into the environment. Major SAs of this type have occurred three times in NPPs, in Three Mile Island (USA, 1979), Chernobyl (former USSR, 1986) and Fukushima (Japan, 2011). Hence, NPP SAs are the focus of considerable research, in a few facilities worldwide, encompassing many challenging phenomena, complicated by very high temperatures (often exceeding 3000 K) and the presence of radioactive materials. Compared to this scenario, fast neutron reactors present radically different boundary conditions, in that the reactor is cooled by liquid metal (typically Na or Pb) and not by water, in order to remove the larger amount of heat produced. Moreover, the cladding layer separating the fuel from the primary coolant is made of steel as opposed to the zirconium-based alloy (Zircaloy) used in more traditional thermal reactors. Therefore, although several studies are available in the literature about the material interaction leading to corium formation in thermal nuclear reactors [2] [14], considerable extra research is needed for the material safety assessment in fast neutron reactors, whereby different material systems play a key role. Starting from the inner fuel element, it is then obvious that the first material system of interest in this context, besides the pure fuel itself, is the one based on the Pu-rich fuel-steel cladding interaction, which is indeed the object of the present research, with particular focus on the interaction between oxide fuel and steel cladding. Since the interaction between uranium dioxide and steel has already been addressed in the past [13] [5] [4], this thesis work focusses on high-temperature interactions between plutonium dioxide and iron oxides representing important components of steel. The melting behaviour of such systems has never been

experimentally studied, and therefore the present results will certainly pave the way to a novel material safety assessment for fast neutron reactors.

In order to tackle the difficulties inherent to investigating highly radioactive samples at elevated temperatures and strongly sensitive to the environmental atmosphere, a controlled-atmosphere laser-heating and fast radiance spectro-pyrometry facility [15] [16] was implemented at the European Commission's Joint Research Centre's Institute for Transuranium Elements. Thanks to the limited sample size (typically on a cm and 0.1 g scale), the high efficiency and remote nature of laser heating, this approach permits fast and effective high temperature measurements on real nuclear materials, including plutonium and minor actinide-containing fission fuel samples. This technique was already applied to the study of various refractory materials, including MOX and other types of fast reactor nuclear fuel [17] [18] [19], and the interaction between oxide fuels and zirconium-based cladding materials [20]. This is the first time that such experimental approach is employed to study the direct interaction between plutonium dioxide and steel components. In the present investigation, the technique is also improved by the addition of a zirconia-based oxygen probe system, yielding reliable data about oxygen release from the sample during the laser-heating experiments. Details about the current experimental approach are reported in the next sections. The oxygen balance of the investigated sample constitutes in fact an essential parameter determining the chemical stability of the material phases produced during the laser-induced thermal excursions. From the viewpoint of real accident simulations, availability of oxygen data permits a more accurate analysis of the material behaviour under conditions that may be produced during a mishap, such as for example, air or inert gas accidental ingress inside the reactor core.

This work means to provide new reference material data on the Pu-Fe-O system and consistent indications on when and how low-melting or highly volatile phases are produced under different conditions of temperature and chemical environment.

2. Materials and methods

2.1 Introduction

In the present chapter a complete description of the sample preparation and of the experimental setup, together with the involved analysing methods, is reported. Moreover, the instrumentation and its calibration are described, reporting the thermodynamic model used during results evaluation, describing the main equations and the basic hypothesis. At the end of the chapter an overview of the estimation of the relative uncertainties on the resulting data is reported.

2.2 Sample fabrication

The first goal of this work consisted in the fabrication of suitable samples for the planned analysis and characterization. As the final objective of the project was the phase diagram (PD) determination for the PuO_2-Fe_3O_4 system, it was of primary importance to characterize the whole composition spectra, thus it was decided that several batches were to be fabricated at different concentration of the two species. Since the context of the present study is to investigate the behaviour of the nuclear fuel in case of high temperature interaction with the cladding, where complete (or only partial) mixing could take place, it was decided that the different compositions had to be taken considering the atomic percentage (at %) of each specie in metallic form, instead of the simple molar percentage. Doing so avoids one of the main issues of PD determination, which is the clear definition of each measuring point on the x axis (i.e. concentration). In fact, if stoichiometry changes can't be excluded a priori, in case of oxides the oxidation state can be significantly affected by many factors (like temperature, chemical potentials and surrounding atmosphere [9] [7]) and subsequently the relative molar abundancy, while it is considered to be negligible the amount of

metallic substance lost, mainly because of direct evaporation. Actually, stoichiometry changes were expected during the planned experiments because of the thermodynamic conditions that were supposed to be withstood by the sample, thus, considering atomic percentage of metals could help reducing the uncertainty on composition, delivering more consistent data. In order to analyse the whole spectra, 4 batches were planned with 20, 40, 60 and 80 at% of metallic Pu with respect to the totality of metals (Pu+Fe).

Before starting to process the material, it was important to establish which were the criteria to be followed during fabrication. It was of primary importance that the resulting pellets could withstand a certain degree of mechanical stress induced by manipulation, so to be mounted on the sample holder. In order to achieve this goal, sample density should be at least 85% of its theoretical value for the mixture. The theoretical density (TD) was calculated as:

$$TD = \frac{1}{\left(\frac{wt_1\%}{TD_1} + \frac{wt_2\%}{TD_2}\right)} \qquad (2.1)$$

Where TD_1 and TD_2 represent the theoretical densities of pure PuO_2 and Fe_3O_4 and $wt_1\%$ and $wt_2\%$ are the relative weight percentages in the mixture for the two species. Moreover, the sample thickness had to be kept under control in order to save material while fulfilling the requirements of the experiment. The geometrical constrains induced by the laser-flash technique, although not as demanding as other measurements [6](i.e. thermal conductivity or diffusivity), still require the sample to have certain characteristics to be correctly performed. As mentioned, a minimum of 1.5 mm thickness was estimated to be suitable for the present work, not only because it allowed decent mechanical stability and good resistance to thermal shocks, but also because of the good compromise with material availability requirements. Nonetheless, in the present experimental setup a 4.8 mm laser spot was used, thus it was necessary for the sample to be at least 5 mm to completely absorb all the energy delivered by the laser and to keep

a portion of it always solid. This is necessary in order to prevent the sample to collapse because of complete melting and to avoid external contamination in the chamber. If this was not the case, the laser could heat up the graphite holder screws, very likely inducing chemical interaction at high temperatures at contact boundaries, ruining the measure. Actually, one of the main advantages of laser heating is (apart from the high temperatures reached) the extremely reduced portion of sample involved, down to 1.8 mm spot. This characteristic can be exploited to obtain what in literature are called "self-crucible conditions" [8], in which sample contamination induced by the crucible is prevented by making the sample itself the crucible, so that no external chemical interaction is possible apart from surrounding atmosphere. To fulfil these geometrical constrains calculations were done considering several effects, a 75% TD was estimated to be resulting from pressing with 1% radial expansion from the matrix dimensions, thus obtaining predicted height and radius. Unfortunately, completely comply with the abovementioned requirements by means of cold pressing only showed to be unfeasible, requiring a further step of sintering after pressing. These values were then corrected for the foreseen shrinking effect of the sintering, which was estimated to be isotropic, varying from 8% to 15%, depending on PuO_2 abundancy. Indeed, the shrinking effect was expected to be mainly dependent on the plutonium oxide rather than Fe_3O_4, because, as it will be explained, the iron oxide was already annealed in argon, thus it was supposed to be more stable at high temperatures. The iron rich disks resulting from cold pressing proved to be very fragile, the reasons behind this are still uncertain. In order to investigate the pressing properties of the iron oxide, cold pressing was performed also on pure powder of Fe_3O_4 only in another press with electronic controls that resulted in stable pellets. The poor green pellets mechanical stability was then attributed mainly to the impossibility of controlling all the pressing parameters, in fact, due

to high sample radioactivity, fabrication was performed exploiting an in-glovebox Lauffer hydraulic press (model VIUG 16, figure 2.1), in the Pu-line at JRC.

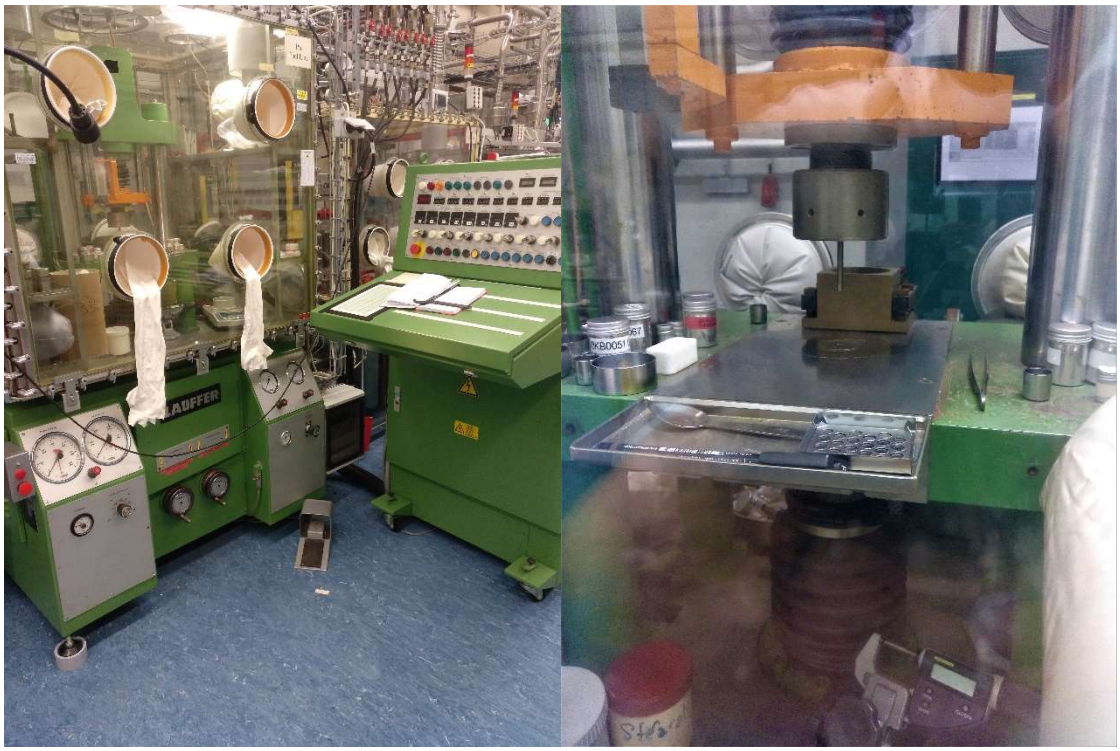

Figure 2.1: Lauffer hydraulic press, model VIUG 16, in the Pu-line at JRC Karlsruhe.

Unfortunately, the latter was limited in certain parameters (i.e. pressing velocity, minimum axial force, piston motion control etc) by its constitution, complicating the fabrication process. In order to improve sample's quality from the Pu-line pressing, as already mentioned, sintering was performed. If on the one side this process was expected to increase the pellets density (thus their mechanical stability), on the other side the shrinking effect could induce residual stresses while also reducing their thickness below threshold. Moreover, the two compounds had very different properties and structures, making them unsuitable for simultaneous sintering. Particularly, Fe_2O_3 is expected to modify its structure during sintering from rhombohedral to the close packed cubic lattice typical of spinels, thus, it was decided to reduce this latter effect by obtaining the

Fe_3O_4 powder to be pressed by pre-heating pure Fe_2O_3 (99.5% purity with 325 mesh) in a Degussa VSL 10/18-Molybdenum cold wall furnace (figure 2.2). The powder was heated at 1400°C for 4 h, exploiting 200°C/h ramps for heating and cooling, in inert atmosphere (argon).

Figure 2.2: Degussa VSL 10/18-Molybdenum cold wall furnace in the Pu line at JRC Karlsruhe.

This process delivered almost stoichiometric Fe_3O_4, as it will be shown in the following paragraph, with all the Fe_2O_3 completely reduced and a slight over-reduction in FeO, which was measured to be negligible compared to the other species. The Fe_3O_4 powder was then moved to the Pu-line glovebox press, where it was mixed in suitable proportions to obtain the composition requested, each batch was milled and mixed in a mortar, so to reduce inhomogeneities and decrease particulate size to the order of 10~100 μm. Zinc stearate was also added as a lubricant in the mixture before pressing in small amounts, so to reduce friction during pellet movement in the channel. After mixing, the powder was

pressed for 5 seconds in a 5.8 mm steel matrix under 15 kN of force distributed biaxially, each time feeding ~250 mg of mixture. In order to decrease the mechanical stresses induced by after-pressing expansion, the steel matrix upper edge was modified so to have a 1% vertical slope in the last 10 mm, preventing the sample from dilatating abruptly with a 90° edge while leaving the pressing channel.

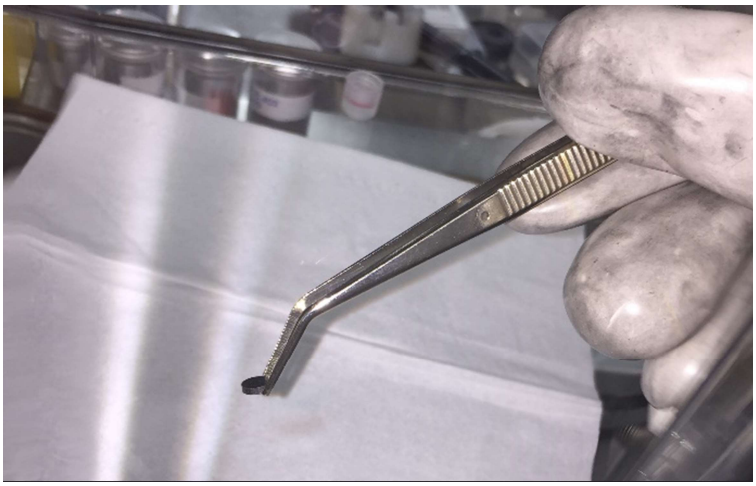

Figure 2.3: Typical sample after sintering.

This process delivered pellets not resistant enough to allow pre-sintering geometrical measurements but sufficiently solid to be handled and moved to the adjacent oven for sintering at 1200°C in inert atmosphere. Zinc stearate completely evaporated at this stage, leaving no trace of contamination, as it was proved by pre-melting characterisation with XRD. After sintering the recorded density proved to be around 90% of the TD for all the disks, with average diameter of 5.65 mm and 1.62 mm height for all the batches, fully satisfying the initial criteria. A typical example of produced pellet is shown in figure 2.3. At the end of the process pellets appeared to be sturdy and almost black, but still some cracks could be spotted by eye on the surfaces. For this reason, it was decided that melting point only was to be performed on the specimens regardless of the thermal conductivity experimental set-up availability. In fact, preliminary

characterization showed the presence of porosities and cracks inside the pellets, missing one of the main requirements for thermal conductivity assessment (TD > 95%) [6]. After manufacturing the samples were labelled and moved to the experimental setting for measurement performing.

2.2.1 Preliminary characterization

As stated in the previous paragraph, although the melting point assessment is not as demanding as other techniques, it is still of primary importance to check the validity of the major hypothesis of the considered model. Since the present work's main goal is the PD determination for a two-species system, the primary requirement for a good melting point measurement (alongside with the geometrical ones) is ensuring homogeneity in all cross sections of the specimen for all batches. This latter issue was faced by means of SEM analysis, as shown in figures 2.4 and 2.5, after appropriate preparation where samples were embedded in a silicon matrix by means of a special glue and polished against a fine sand brusher (an example is shown in figure 3.21). When dealing with oxides of different weights and structures problems of mixing are very frequent. Because of powder size, agglomerates are very likely to form, delivering unbalanced concentrations throughout the cross section, especially when cold pressing is exploited. This is due to the high mechanical force used, that favours the formation of larger (and heavier) agglomerates in the central region while leaving small clusters dispersed in the matrix in the outer regions. As it appears clear from figure 2.4, this was not the case, with homogeneity being attained to a good extent, showing grains of different sizes of Fe_3O_4 evenly scattered in the PuO_2 matrix. The reported compositions shown were chosen in order to prove consistency of the results both radially and axially, even at very different relative abundancies.

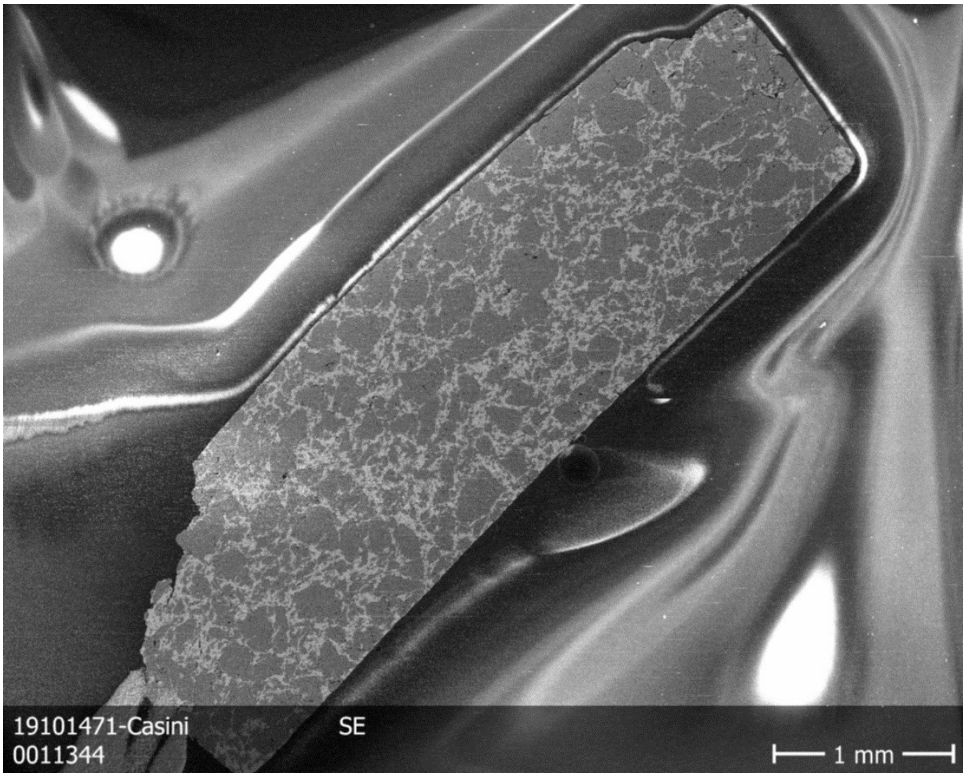

Figure 2.4: SEM picture with 25x magnification of the 20 at% Pu sample. As it appears clear, homogeneity is attained to a good extent in the axial direction, with grains of different sizes of Fe_3O_4 (black) evenly scattered in the PuO_2 matrix (white).

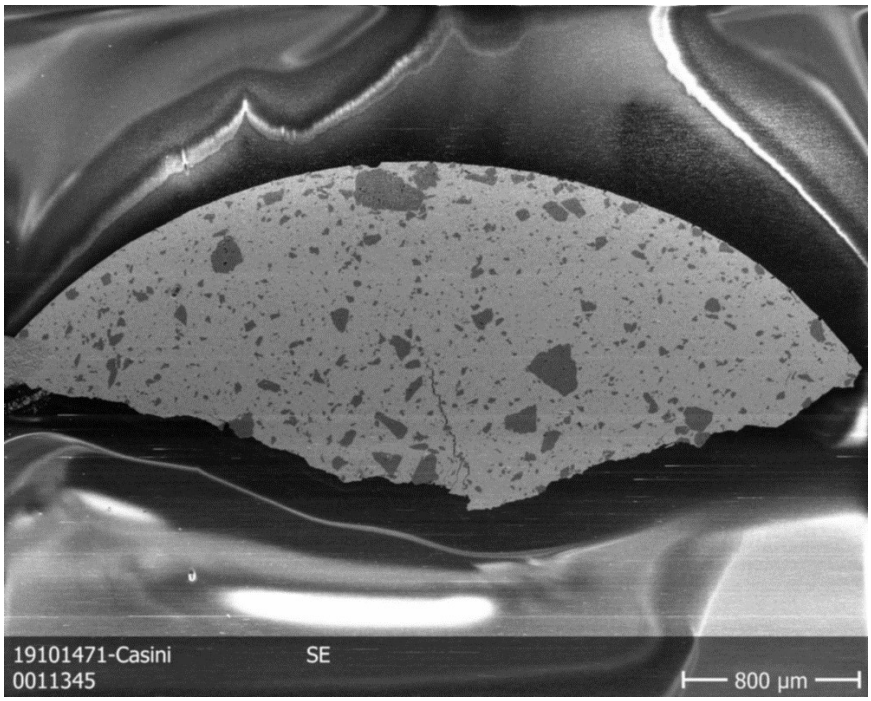

Figure 2.5: SEM picture with 25x magnification of the 80 at% Pu sample. Once again, homogeneity is attained to a good extent also in the radial cross section, with grains of different sizes of Fe_3O_4 (black) evenly scattered in the PuO_2 matrix (white).

This further confirms that homogeneity is attained throughout all the sample volume, with no evident concentration gradients, especially in the close vicinity of the surfaces, which are the part directly exposed to melting and atmosphere. Cracks and porosities are present in the sample preventing high densities (>95% TD), therefore making the sample unsuitable for thermal conductivity measurements. A typical example is reported in figures 2.6 and 2.7. Although the presence of porosities is to be considered almost certainly linked to the manufacturing process, it is impossible to assess whether the cracks were induced by the sample fabrication or the preparation polishing.

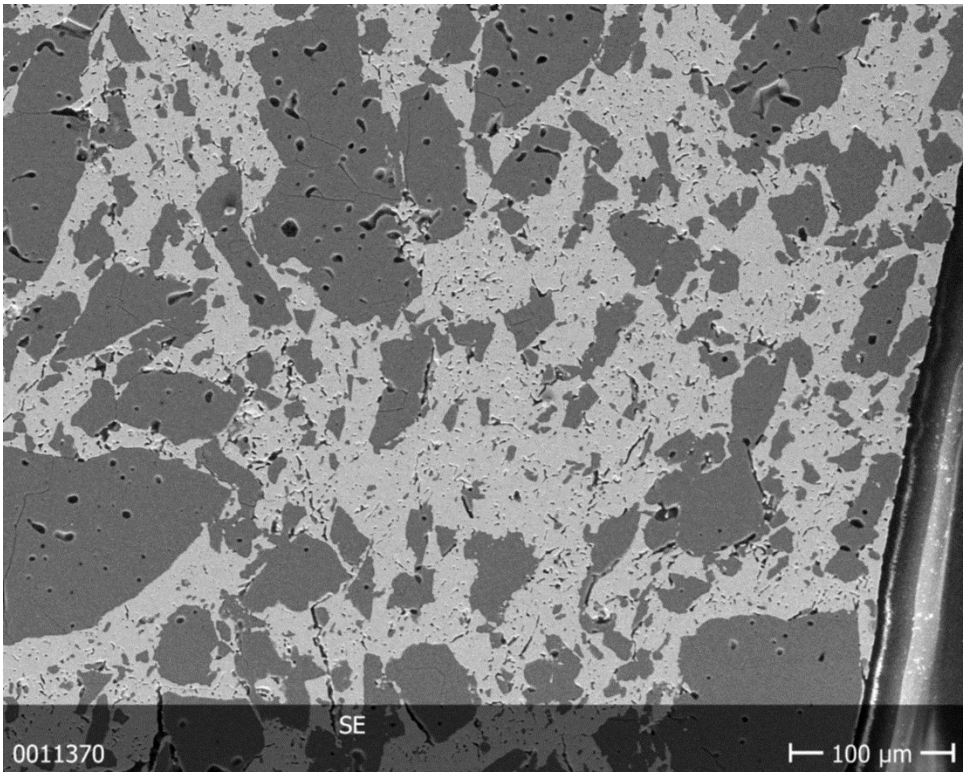

Figure 2.6: Increasing magnification at 200x of the 40 at% Pu sample. Once again homogeneity is attained but cracks and pores are present in the whole structure, both in the embedding matrix and in the iron grains.

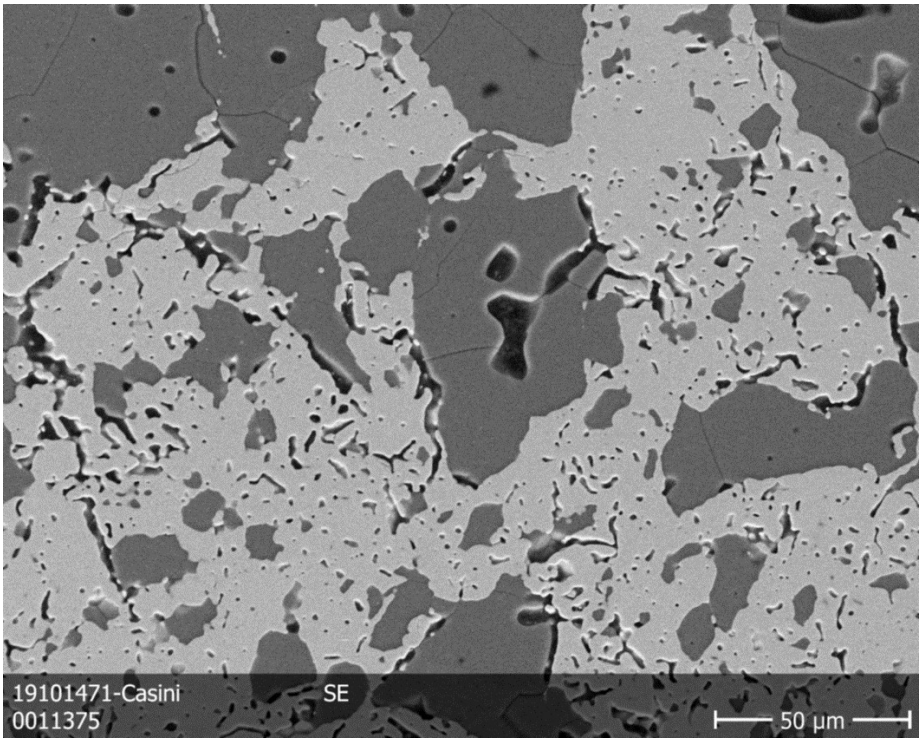

Figure 2.7: Increasing magnification at 500x of the 40 at% Pu sample. Once again homogeneity is attained but cracks and pores are present in the whole structure, both in the embedding matrix and in the iron grains.

Another major concern during pre-melting characterisation is the determination of the chemical composition during measurement, so to clearly define the PD abscissa in consideration. The experimental setup exploited in the present work took advantage of the so called "self-crucible conditions", by which the melted portion of the sample doesn't get in contact with any external media, preserving the initial composition from contamination. Of course, in-vacuum measurements were excluded in order to avoid excessive evaporation induced by low pressures and subsequent obscuration of the optical path [21], it was therefore impossible to prevent contact with the atmosphere gas, thus chemical interaction is to be expected.

Unfortunately, technical difficulties related to arranging an experimental set-up capable of recording at the same time both melting point and composition changings induced by the environment are stringent, so very often in literature constant composition is hypothesized [9] [21].

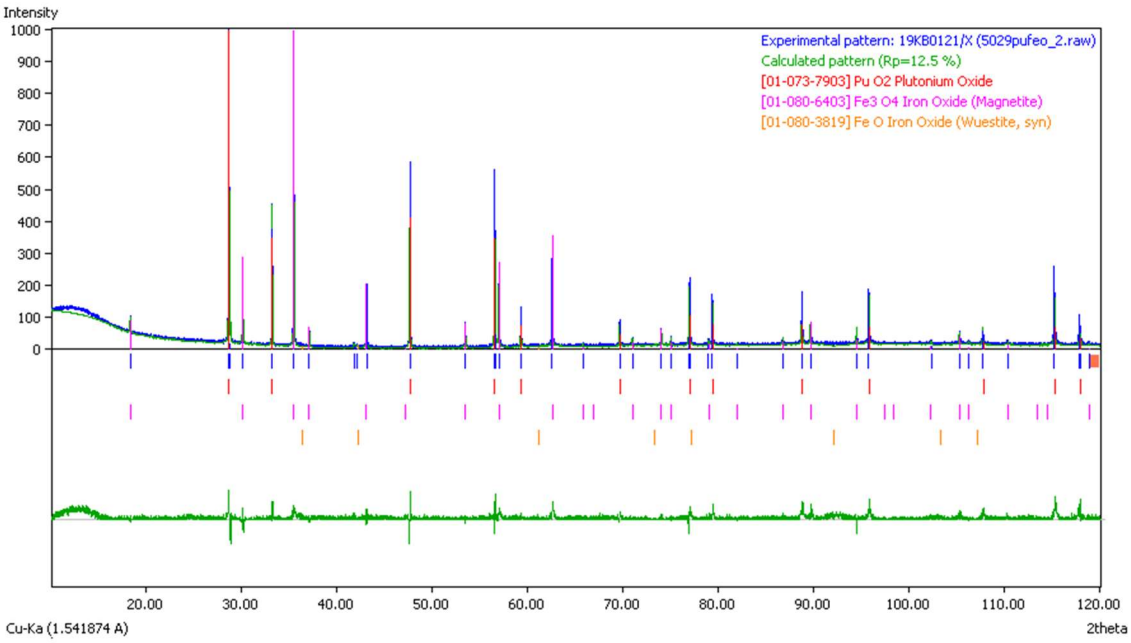

Figure 2.8: XRD analysis on the 20 at% Pu sample. The recorded spectrum is reported in blue, while the element characterisation is shown with the different colours.

That is the reason why chemical characterisation of the system in question with suitable methods (XRD, EDS and similar) is of primary importance before and after the measure. This is done in order to obtain a cross-check that the initial hypothesis of non-relevant composition changings is attained and to what extent, furthermore it is also a valuable tool to gain a clearer overview of the results for data interpretation. In the present work XRD analysis was exploited to acquire information on composition before and after melting on all batches. One example is reported in figure 2.8.

Unluckily, the XRD instrument available at JRC Karlsruhe is furnished with a copper emission tube, producing x-rays that induce fluorescence in iron rich samples. This phenomenon is very well known in literature [22], due to the wide diffusion of this kind of instruments (because of their economic availability) and the large presence of iron in engineering-related research samples. The most adopted solution to this problem, excluding the replacement of the radiogenic emitter with a more suitable (and expensive) material, is adjusting the energy window of detection. In fact, the main drawback of fluorescence is the intense

background signal that is delivered, that makes the distinction of peaks in the diffractogram almost impossible. By re-calibrating the XRD detector in a suitable way, it is possible to cut-off background noise to a good extent, producing a decent resulting spectrum. The main drawback of this method is the relevant reduction of sensitivity induced on the instrument, in fact, a complete XRD spectrum is constituted of many peaks, the position of which is characteristic of one element only. The diffractogram obtained during measurement is compared with spectra relative to pure substances known in literature, matching not only the peaks positions (depending on the diffraction angle), but also their intensities (which is directly proportional to atomic abundancy), obtaining a complete characterisation of the chemical composition. In the present case this process was unfeasible because of the impossibility to detect low intensity (but relevant) peaks, hidden by the reduced energy window detection efficiency. This effect can be observed in figure 2.8 where, by means of coloured lines, the expected peaks are highlighted, reporting also their projected intensities. As it can be seen, most of the major peaks are matched in position, but some of the proposed lines are not paired to any detection. Moreover, it can be seen that no proportionality is detected between the measured peaks and the expected ones. From that we can deduce that all the XRD analysis obtained this way are representative only of a qualitative estimation of the composition, solely identifying the presence or absence of certain elements and cannot deliver accurate information on their abundancy. Nevertheless, the resulting diffractogram shown in figure 2.8 can be exploited to obtain useful information. Although the oxidation state of the sample cannot be investigated this way because of what reported above, the presence of PuO_2 and Fe_3O_4 is detected in large quantities in the sample, confirming that the manufacturing process worked correctly. Especially, the presence of magnetite is a relevant result, proving the reducing effect of the pre-

sintering annealing on the Fe_2O_3 powder in argon. On that regard, it is interesting to note the presence of FeO, highlighted by the peak detected at 2theta close to 40. The presence of this specie in the sample was not expected but still hypothesised for several reasons. Firstly, FeO represents the further reduced step of Fe_3O_4, thus it is reasonable to assume that even if annealing time was well estimated, a small portion of the initial Fe_2O_3 could have reached the minimum oxidation state. Secondly, Fe_3O_4 is a spinel, and therefore a chemical compound formed by two specie with different oxidation states but similar structures, sharing an anion in order to form a stable compound. In the present case Fe^{+2} and Fe^{+3} bond together with O^{2-} in a face centered cubic lattice, so it is reasonable to expect traces of contamination from both Fe_2O_3 and FeO following a high temperature annealing and a successive sintering, where partial structural recombination phenomena could have taken place. Nevertheless, although the XRD reported is not representative of quantitative measurements, it is evident that only traces of FeO have been detected, for no more than two out of eight expected peaks were matched in position, suggesting that the presence of this specie is barely measurable and therefore negligible for the present application.

2.3 Experimental set-up

In the present paragraph the experimental set-up used during melting point measurements will be described. Although the implemented techniques are known and well established in literature [15] [16], some improvements were introduced in the experimental scheme and will be shown.

It was necessary to arrange a measuring set-up capable of satisfying some criteria in order to obtain useful data. The first criterion to be fulfilled was safety, in fact, the system in consideration is known to be highly radioactive and therefore extremely toxic in case of prolongated exposition or direct inhalation. For this reason, the experiment was designed to take place inside a sealed glovebox

(figure 2.9) in the contamination area at the JRC – Karlsruhe, where high safety standards could be granted during the whole duration of the experiment against normal and accidental scenarios. On that regard, the glovebox was operating in nitrogen atmosphere, so to suppress any possibility of fire accident, and constantly kept at a lower pressure than the laboratory, in order to prevent any leakages. The glovebox walls were designed so to absorb a portion of the radiation emission that builds-up inside which, in general, is not sufficient to fully shield the operator when handling Pu, thus a lead apron is usually employed as further protection.

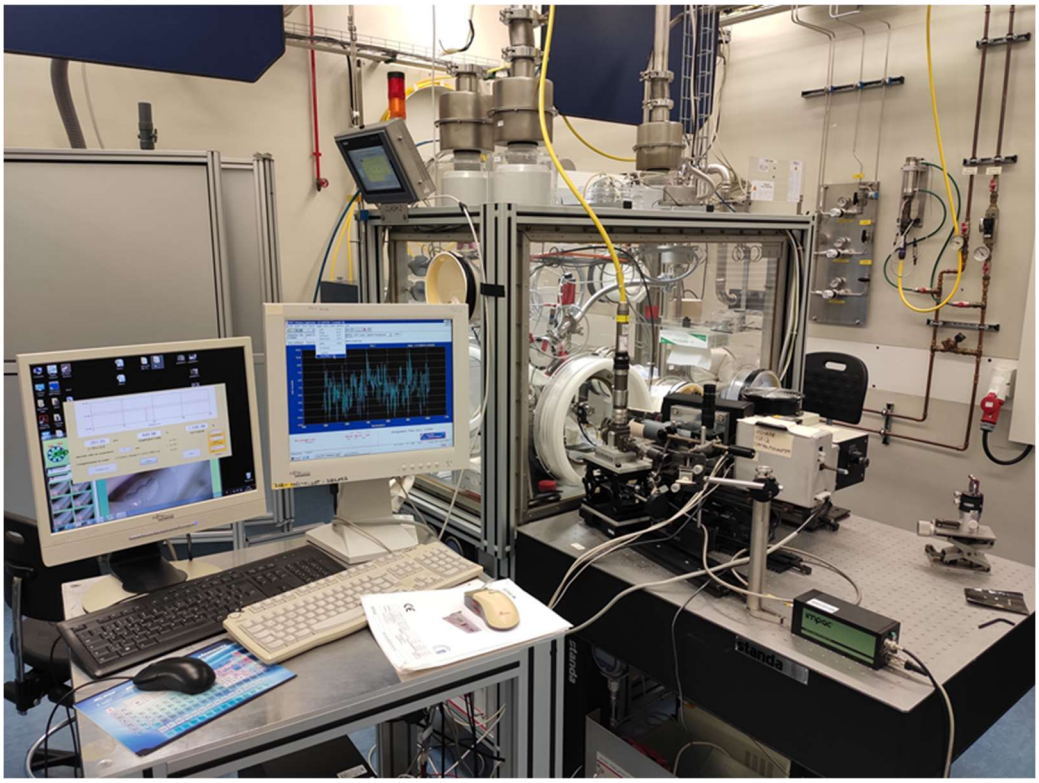

Figure 2.9: The experimental set-up arranged inside the sealed glovebox. On the left it can be seen the acquiring system for the spectrometer and the oxygen gauge.

Nevertheless, since the glovebox was new, and therefore the activity level was relatively low, it was not necessary to exploit further protection devices apart from the ones described above. Nonetheless, the activity levels inside and outside the glovebox were monitored periodically, so to ensure adequate exposure levels to its operators.

The second criterion to be satisfied was the necessity to record phenomena like PTs involving very small time scales at extremely high temperatures, thus the need for adequate instrumentation. As it can be seen in figure 2.9, many devices were set inside and outside the glovebox in order to fulfil this task. Inside the glovebox a stainless-steel containment vessel was set, directly linked to the gas line of the institute, allowing for several gases to be used as atmosphere during the experiment. In particular, the steel vessel could be filled with argon, nitrogen, or a mixture of argon and hydrogen, moreover an external valve allowed for inlet of any gas coming from a suitable pressure bottle. For the present work this will be a fundamental feature since the experiments were designed to be performed both in argon (coming from the line) and in air (from a pressurized bottle). Given that the measures were expected to be carried out by means of radiation thermometry, the two sides of the pressure vessel facing the recording equipment were constituted of a highly pure sapphire window of known transmissivity at the operative wavelengths (0.86 between 450 and 1064 nm). The presence of a glass window strongly reduces the possibility to operate at high pressures, nevertheless, the vessel could be brought in pressure up to 5 bars or resist high vacuum up to E-08 hPa. The slight overpressure is a preferable condition compared to atmospheric pressure because it suppresses evaporation during the experiment [21]. This latter fact is vital since the temperature is recorded by means of optical thermometry, it is therefore fundamental to cut off all the phenomena affecting optical path transmissivity (such as material evaporation from the sample) that would lead to high uncertainties or erroneous measurements. For the same reason, a highly pure optical window (BK7 optical glass) was installed also on the glovebox walls (0.92 transmissivity) so to avoid optical path disturbances as much as possible and for his high resistance to temperature and mechanical stress. Although the transmissivity of these glasses

is very high, because of the intense power delivered by the laser (from 300 W to more than 1 kW), intensity of the reflected light could not be neglected. Since the semi-transparent media were more than one, multiple reflections of the laser beam raised from both glasses' sides, and even if this light is not properly focused, it can be very dangerous, especially in presence of sealed gloves that can be damaged easily. This is the reason why it was necessary to take care that the relative position of other instruments was not matching the direction of the laser reflections, that were blocked as soon as possible with graphite absorbers as shown in figure 2.10. In order to attain self-crucible conditions, a specific sample holder was fabricated, as shown in figure 2.11.

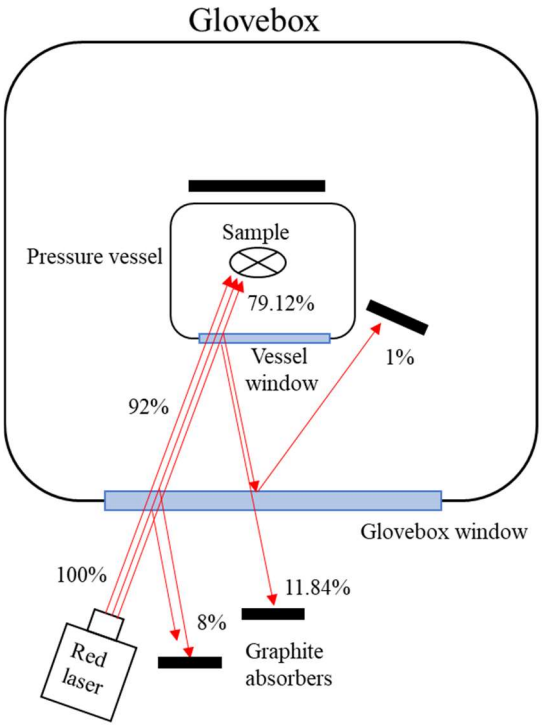

Figure 2.10: Scheme of the reflections inside the glovebox. The intensity of the beam is reported as fraction of the initial power output, graphite absorbers are placed so to absorb any fraction of reflected light.

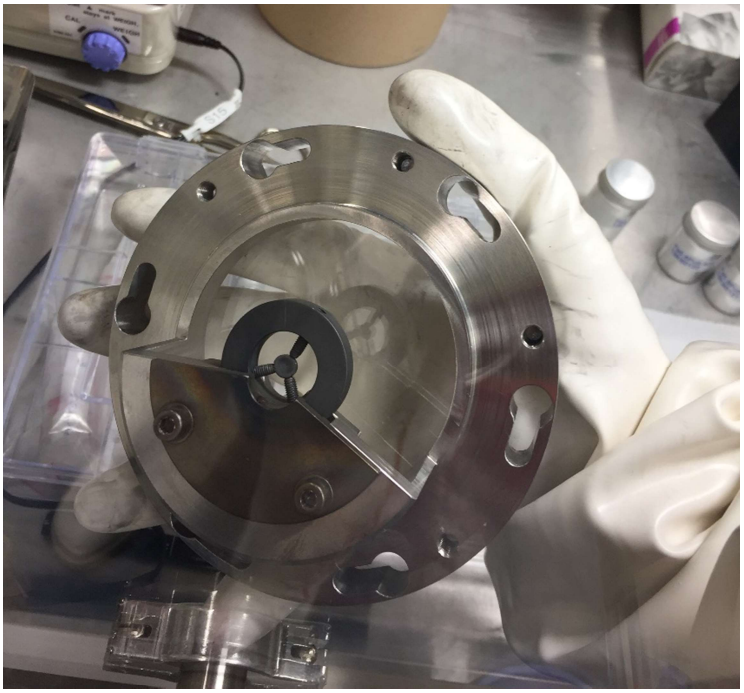

Figure 2.11: Sample holder with the graphite crucible mounted and a sample screwed.

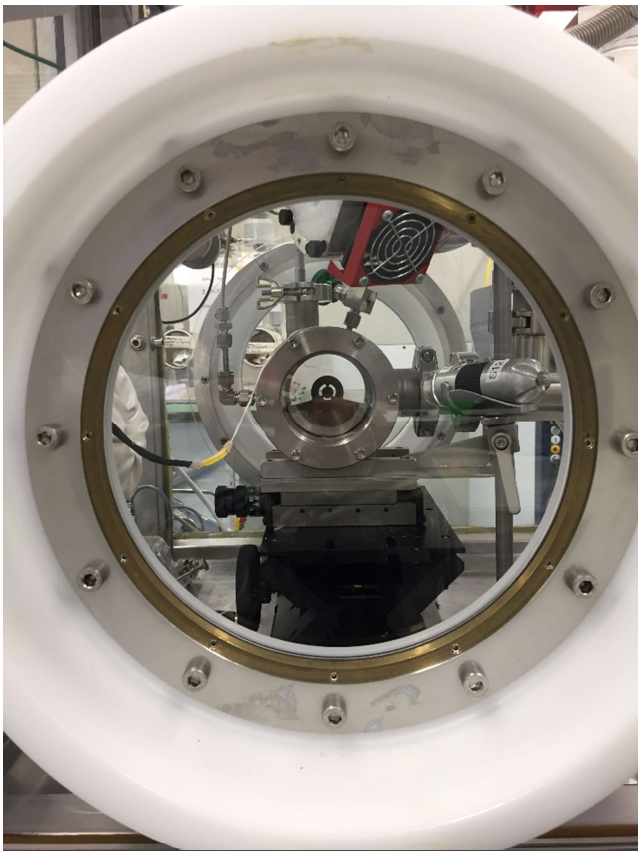

Figure 2.12: Frontal view of the pressure vessel trough the glovebox BK7 window. The vessel window (sapphire) can be observed as well, inside which the sample is mounted on the graphite holder.

The main holder consisted of a semi-cylindrical steel frame in which a smaller crucible of different materials could be tightened. In the specific application it was decided to use graphite both for the circular holder and the adjusting screws. The reason behind this lay in the extremely high melting point of this material, that makes it suitable for this kind of applications, whereas metal alloys have to be disregarded because of their high thermal conductivity that would cause unacceptable temperatures on the pressure vessel. In figure 2.12 the pressure vessel with the graphite sample holder mounted is shown, together with the adjustable support for the vessel and an HD camera featuring a x10 optical zoom, useful to control the experiment from the control room.

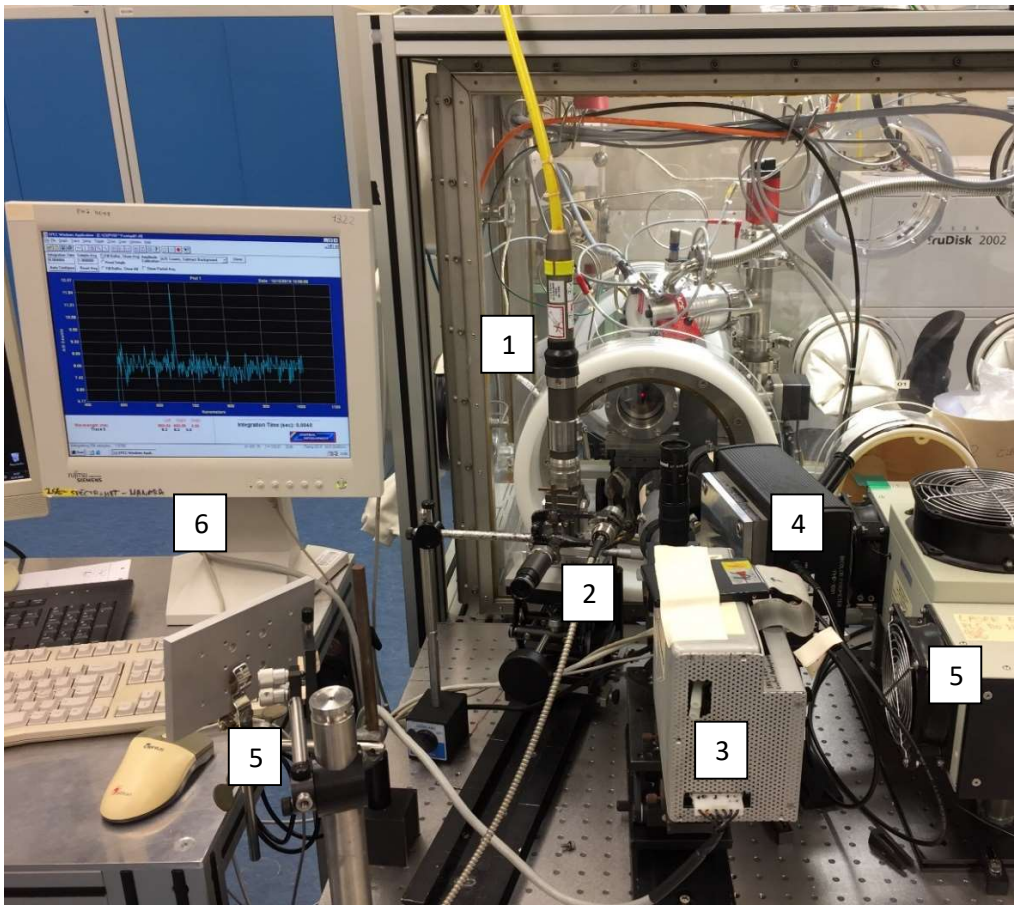

Figure 2.13: Acquiring and triggering system. 1) optical fiber for the laser, 2) low temperature pyrometer, 3) 256 channels spectro-pyrometer, 4) high temperature pyrometer, 5) blue laser source and mirror, 6) triggering system for the spectrometer.

On the outside of the glovebox all the necessary apparatus for triggering, recording and data analysing are set as shown in figure 2.13.

The optical fiber *(1)* is connecting the laboratory to a Nd:YAG laser model TRUMPF HD 4506 that was delivering laser pulses at 1064 nm down to 1 ms long. The fiber is then connected to a suitable optic with focal distance of 48.9 cm aiming directly at the sample, which is going to be heated to the desired temperature by the incoming light. Aside the laser beam is placed a linear low temperature pyrometer *(2)* model IGA740-lo (former Lumasense inc., now Advanced Energy Industries inc.) with operative range between 800 K and 2600 K. The sensitivity of this instrument is not as good as the other pyrometer deployed (OLGA) and no PTs are expected to be found below 1500 K, still its low temperature range is useful to have a double confirmation of eventual points recorded by OLGA in close vicinity of its lower working limit (1500 K) where linearity of the instrument is no more granted by its manufacturer (Joint Research Institute for High Temperature, Russia). In the central region is placed the 256 channels spectro-pyrometer *(3)*, this position was chosen because the main purpose of this instrument was obtaining the spectral emissivity of the sample during the experiment, as it will be explained in paragraph 1.3.2. It is known in literature that emissivity of heavy oxides is only slightly affected by angle up to 30° deviation [23], still a central position is always preferable, thus it was attained. The equation used to convert the photodetector counts in radiance temperature is:

$$\frac{1}{T_\lambda} = \frac{\lambda}{c_2} ln\left[1 + \frac{s_{cal}}{s_\lambda} \cdot \frac{t_{int}}{t_{cal}}\left(e^{\frac{c_2}{\lambda T_{\lambda,cal}}} - 1\right)\right] \qquad (2.2)$$

Where λ is the wavelength, c_2 is the second radiation constant defined in paragraph 2.3.2, s_{cal} is the number of counts obtained during calibration of the spectrometer, $s_\lambda$is the number of counts of the recording, t_{int} is the integration time used in the measurement, t_{cal} is the integration time during calibration and

$T_{\lambda,cal}$ is the radiance temperature during calibration relative to the considered wavelength. The 256 channels of this device were calibrated in order to obtain suitable information over a wide range of wavelengths, spacing from 400 nm to 1100 nm, this can prove useful in order to check wavelength dependence of the computed emissivity (i.e. checking the validity of grey body assumption). Although this spectrometer could also deliver information on the detected temperature, its time resolution is quite poor, with a minimum sampling time of 4 ms only, making almost impossible to distinguish small PTs like those generated with the current method. For this reason, on the right-hand side *(4)* a 2-channel ultra-fast pyrometer (OLGA) was placed, which is the primary temperature reference of this set-up. The minimum sampling time for this instrument is 10 μs, which is more than what is necessary for the present application, for this reason the sampling time was set at 100 μs, thus reducing the noise, but maintaining a much faster sampling rate than the spectrometer mentioned before. Two channels were set with different aims, the first one was used for temperature measurements, it was calibrated at 650 nm so to be fairly in between the effective range of the emissivity calculation of the spectrometer, and since this wavelength is close to the maximum energy emittance for a black body at the same temperature of the ones expected (~3000 K). Moreover, this wavelength is considered a standard in radiation thermometry for instrumental calibration against lamps. This pyrometer was mounting a logarithmic amplifier, thus its conversion law is:

$$T = \frac{B}{V + \beta \, log_{10}(\tau\varepsilon) - A} \qquad (2.3)$$

Where A, B are calibration constants and β is the offset of the amplifier, V is the recorded voltage, τ is the transmissivity of the optical path and ε the sample emissivity. The second channel was set at 488 nm, this specific wavelength was chosen because it was matching the emitting wavelength of the blue laser as it

will be explained later. The effective range of OLGA is known to be from 1500 K to more than 5000 K, although the very high precision of the device, the logarithmic amplifier can show some deviations when close to its operative limits. For this reason, the IGA pyrometer was set as secondary check of low temperature measures of OLGA; nevertheless, results showed matching temperatures in the common operative range, so it was chosen to rely solely on OLGA, given its higher precision and resolution. Both devices were connected to the same signal converter, a USB-6366 NI, used for I/O signal management. As already mentioned, another laser of a different wavelength was set in the experiment, featuring a 488 nm emitter that appeared as a bright blue light. The main purpose of this device was delivering useful information on the PT exploiting optical properties of the sample during the experiment. In particular, the idea is to detect changings in reflectivity of the investigated surface and to directly link them to the PT as it will be shown later. In order to do so, careful alignment was done so to have the blue laser beam directed on the sample's surface in such a way that its main reflection was perfectly aimed at the second photodiode of OLGA. Since the space on the table and the glovebox window dimensions were limited, it was necessary to use adjustable mirrors *(5)* to deviate the optical path and obtain the desired geometry. As it can be seen in figure 2.13 a metallic shield was placed behind the second mirror, this was done to protect On the left hand-side the triggering system for the spectrometer is shown *(6)*. On the screen, the on-line recorded spectra is reported, in the picture a sharp peak can be observed, relative to the pilot laser of the Nd:YAG laser (diode laser at ≈633 nm), used only for alignment and reflection detection.

Figure 2.14: Gen'Air oxygen gauge and detector, together with the vacuum turbopump controls, its relative manometers, the valve-control plate (ventilplatte) and the manual inlet-outlet valves.

The most interesting feature of the experimental set-up in this work consists in the capability of estimating the effect of the environment on the melting point measure. To do so, the Gen'Air device showed in figures 2.14 and 2.15 was used, which is capable of detecting small changes in the oxygen partial pressure in the gas exiting from the pressure vessel. Thus, knowing the recording temperature is possible to obtain information on the concentration of oxygen in the flow, therefore investigating whether the sample is gaining or losing oxygen in the specified environment. The Gen'Air working principle is based on the Nernst equation (2.4), following which we obtain the resulting voltage at the extremities of an oxygen ions conductor, separating two environments having a different concentration of O_2.

$$\Delta E = \frac{RT}{4F} ln\left(\frac{p_{pO_2}}{p_p ref}\right) \qquad (2.4)$$

Where E is the induced voltage, R is the gas constant, T is the temperature, F is the Faraday constant, p_{pO2} and p_{pref} are the partial pressure of oxygen measured and of the reference gas. This principle is applied in the Gen'Air by means of a

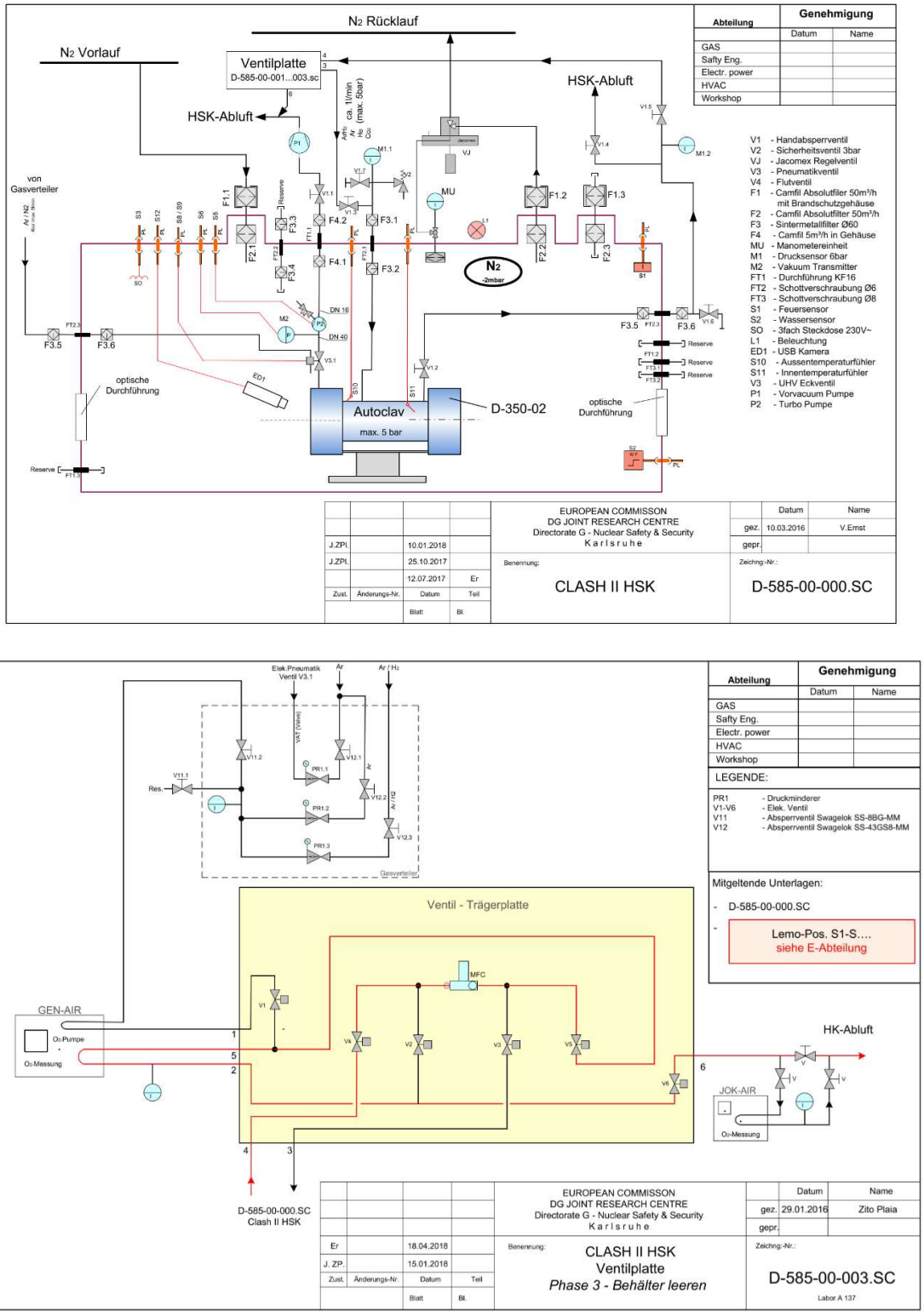

Figure 2.15: Glovebox P&I schemes. Of particular interest is the piping system relative to the gas flow in the control plate ("ventilplatte") highlighted in red, together with the mass flow controller and the oxygen pump.

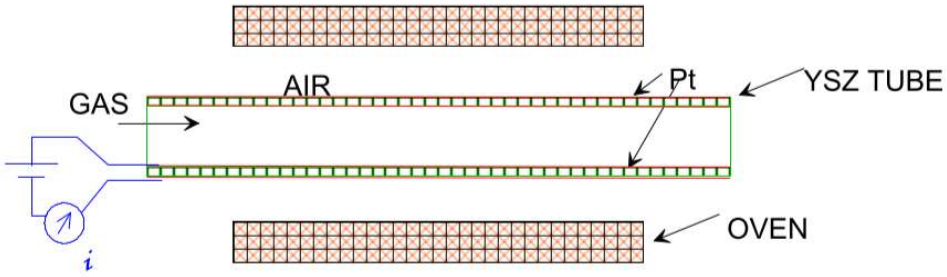

Figure 2.16: Summary scheme of the Gen'Air structure. The flowing gas partial pressure induces a voltage that is detected or, conversely, a fixed voltage from the operator induces a known partial pressure in the flow.

sealed tube of zirconia stabilized with yttria oxide, inside which a known oxygen reference value is delivered by a metallic plate of known oxygen potential as shown in figure 2.16. The tube inside and outside is coated with platinum, when the device is turned on the tube is heated to a known temperature by an oven Nonetheless, the device can operate in both directions, if a fixed voltage is applied to the zirconia tube, oxygen is going to be released (or absorbed) from the flow until the concentration that would induce that voltage is reached. This is possible because zirconia is an electrolyte and therefore at high temperatures allows for the migration of oxygens ions in its structure, permitting enrichment of the flow. Although this is a very useful feature it was never used in the present work, for time constrains and since partial pressure investigation alone proved to be demanding, nonetheless, future works may exploit further this feature. Even if this analysis can deliver very accurate results, it is based on the hypothesis of stationarity, this means that in order to perform any measurement it is necessary to wait a certain amount of time, so to let any transient behaviour to extinguish. The more stringent the accuracy requirements, the longer the period to be waited, so it is important to establish a threshold value that is to be considered the end of the transient behaviour. This must be sufficiently low in order for accurate measurements to be taken, and high enough to reduce the waiting time to a reasonable value. Activating the oxygen pump could have

increased the precision of the measurement of a small extent but it would have increased considerably the waiting time, reducing the number of measures that could be taken, so it was decided that the improvement was not justified because of time availability. In the present work this device was coupled to the argon line of JRC Karlsruhe, in which the experiment was designed to be performed, so a reasonable threshold value was assessed to be 1E-05 atm of O_2, that is the partial pressure relative to the maximum amount of oxygen granted in the line.

2.3.1 Instrument calibration

Whenever dealing with experimental projects, instrument calibration is of primary importance in order to obtain reliable and useful results. In the present work, particular care was dedicated to instrument calibration so to reduce the predicted uncertainty to the smallest extent. Given the different types of instrumentation involved in the measurements, it was necessary to adopt different types of calibration procedures that will be described in the present paragraph.

The first step taken in this sense was performing an overall check of the calibration of all the instrumentation by setting a trial measure of melting point of stoichiometric UO_2. Since both emissivity and PTT of this compound are well known [24] [5] the measurements were compared to literature, the results showed very accurate values for the ultra-fast pyrometer OLGA, which, fed with the right emissivity, delivered exactly 3118 K ± 28 K, perfectly agreeing with previous results. Obtaining a good result at high temperature is suggesting that the instrument might be well calibrated but is not enough to assess its linearity in its whole range, especially because optical pyrometers tend to exhibit criticalities at low counts (i.e. low temperatures). For this reason, a point check close to the lower operative limit was foreseen to exclude any kind of non-linear behaviours. Unfortunately, the spectrometer was unable to record the right value

of emissivity for UO_2, which is known to be around 0.83 ± 0.02. This fact suggested that a complete recalibration of this instrument was therefore necessary. To do so a separate set-up was arranged installing a current-controlled tungsten ribbon lamp as shown in figure 2.17 [25]. This is a very accurate calibration purpose device, built and previously characterised by a national calibration lab (PTB) in order to know the exact dependence of radiance temperature of the ribbon (at a specific height and direction) as a function of current. Since the accuracy of the calibration is directly dependent on the precision of this temperature, it was vital to perfectly control the latter by a flawless trimming of the current, that was obtained using an amperemeter featuring a fine tuning with precision of 1 milliampere. Since the spectrometer has 256 channels it is not enough to know the radiance temperature at one wavelength but a complete characterisation throughout the whole wavelength range is required. Once the λ-T curve is known, the recorded spectrum from the spectrometer is compared to that curve to obtain the radiance temperature relative to each number of A/D counts.

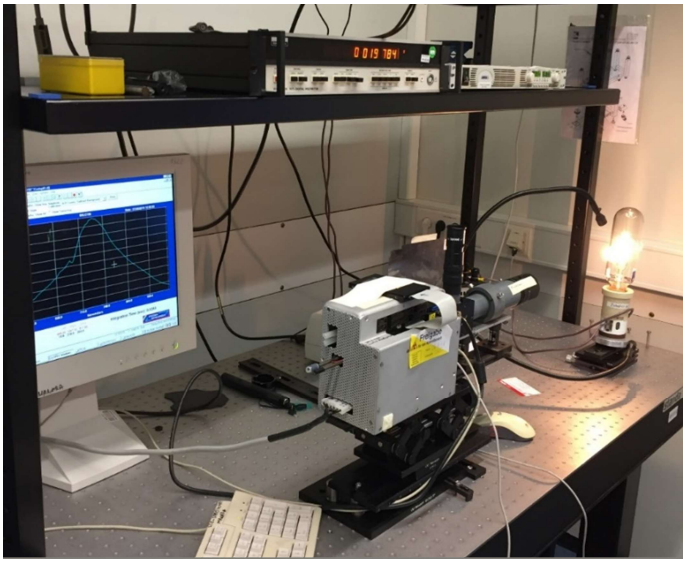

Figure 2.17: Spectrometer re-calibration using the tungsten ribbon lamp. On the monitor the recorded spectrum is shown while on the top the ampere meter is reporting the current flowing through the lamp.

From that and from the number of counts at a known radiance temperature the emissivity calculation could be calibrated as shown in eq. (2.2).

To reduce statistical uncertainty two solution were adopted, the first was increasing the integration time up to 24 ms, thus increasing the number of counts improving statistics. The second was setting the spectrometer in average mode, by which the inner computer of the instrument was performing 5 independent measures and averaging them to deliver one result. This latter method involves very long overall integration times, thus eliminating any kind of long-period transients in the lamp. The calibration was done at different temperatures (from 1800 K to 2400 K) and integration times (from 4 ms to 24 ms) so to have a double check of the linearity of the instrument through the whole range.

After that, a low temperature point check was performed on the OLGA pyrometer, setting the tungsten lamp at 1800 K, close to the lower range limit of the instrument. The detected radiance temperature was within uncertainty of the instrument obtained during the previous calibration, so linearity was considered preserved and no further action was necessary for that device. The last optical device to be controlled was the "low temperature" pyrometer, which was coming directly from the manufacturer and used for the first time in the institute. In order to perform a complete calibration and check the manufacturer data it was decided to use the graphite black body furnace available at JRC, showed in figure 2.18. Exploiting the black body furnace, multipoint calibration was possible, checking both for linearity and the saturation limit, found to be around 2500 K. The resulting calibration was fairly close to the one suggested by the manufacturer and presented the same statistical uncertainty, nevertheless it was decided to adopt it as official one, for consistency with the other devices.

Parallel to this work, testing on the Gen'Air oxygen gauge was performed in order to assess the instrument accuracy. To do so, high vacuum was made in the

pressure vessel and a 24 h flushing was performed with argon coming from the JRC gas line.

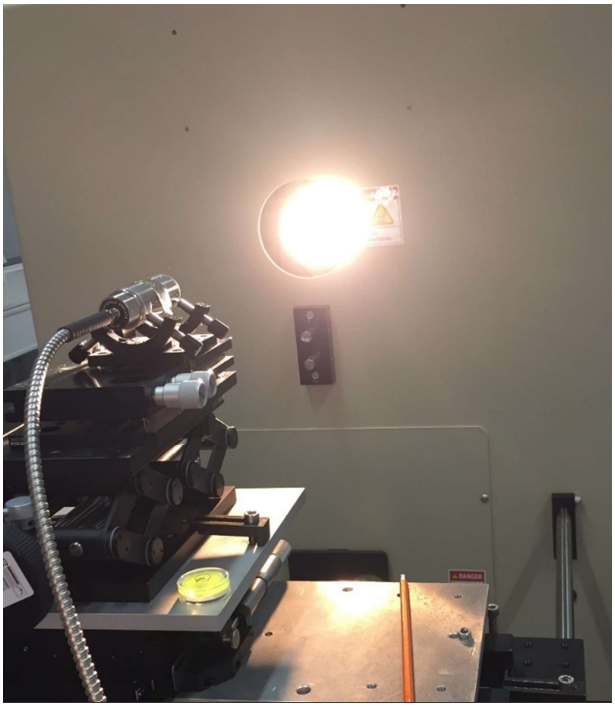

Figure 2.18: Low temperature pyrometer during calibration against the graphite blackbody furnace available at JRC

The previous calibration was done long before and the resulted value was considerably higher than the expected one, thus it was decided that recalibration was necessary. A two-point calibration was prescribed by the Gen'Air manufacturer, so, after high vacuum, another long period flushing was performed with gas coming from a certified 5% O_2 pressure bottle. After recalibration on that value, a one-point check was performed with a 1% O_2 pressure bottle, delivering good results (within 1% relative error) and confirming the new calibration.

2.3.2 Data analysis

The precision in PD determination of the PuO_2-Fe_3O_4 system was directly depending on the data acquisition technique and on how those data are analysed

in order to obtain useful results. In the present paragraph will be presented how and on which assumptions the experimental instrumentation has been used.

As already mentioned, optical thermometry was exploited in order to obtain information on the PTTs of the system. In fact, to correctly measure the temperature with optical pyrometers it is fundamental to have detailed information on:

a) the optical path

b) the relevant optical properties of the sample (i.e. its emissivity).

Luckily, the optical path was perfectly known, for all the windows to be passed trough have well defined transmissivity factors and air/nitrogen refraction index is very close to 1. This is not the case for emissivity, that is a priori unknown and had to be experimentally determined. Notwithstanding, certain hypothesis could be done, for example since both compounds are oxides it is reasonable to assume that the emissivity is not depending on wavelength (grey body assumption) [25], nonetheless it will be vital to assess whether or not this fact is true. Actually, optical properties of PuO_2 are well established in literature [26] [27], and it's known to follow the grey body behaviour, nonetheless, in the present samples iron oxide was also present, the behaviour of which is strongly unpredictable in our experimental conditions. Thus, emissivity of the mixture was very hard to guess a-priori but, starting from the data acquired as described in paragraph 2.2, something could be inferred. Since emissivity of the two species are so different, it is reasonable to assume that a linear behaviour is to be expected depending on relative abundancy. This is coherent with the emissivity being a superficial property and thus influenced by the amount of each compound present on the surface of every batch. This assumption is called Vegard's linear dependence and will be subject of further analysis in the following chapter. Still, even if emissivity was assumed to be linear, experimental investigation was necessary since the

temperature data directly depends on it, thus a high uncertainty on emissivity would result in high uncertainty on temperatures, making the PD determination pointless. To experimentally define this fundamental optical property the 256 channels spectro-pyrometer described in the previous paragraph was used. The main idea was exploiting the linear dependence of $\frac{1}{T_\lambda}$ on λ, valid whenever working with high temperatures (i.e. high frequencies), and if emissivity is proven to be independent from λ (grey body assumption). This property can be easily derived starting from Plank's radiance equation (2.5):

$$B_\nu(\nu, T) = \frac{2h\nu^3}{c^2} \frac{1}{e^{\frac{h\nu}{k_B T}} - 1} \tag{2.5}$$

In which B_ν is the spectral radiance, ν is the frequency, T is the absolute temperature, h is the Planck's constant, c is the speed of light in the medium and k_B is the Boltzmann constant. This formulation can be easily converted to wavelength dependence by using the relation:

$$B_\lambda(\lambda, T) = -B_\nu(\nu, T) \frac{d\nu}{d\lambda}$$

and exploiting $c = \lambda\nu$ one obtains:

$$B_\lambda(\lambda, T) = \frac{2h^{\ 2}}{\lambda^5} \frac{1}{e^{\frac{hc}{\lambda k_B T}} - 1} \tag{2.6}$$

Which is easier to handle to exploit linearity on λ. It is known that temperature is detected by a pyrometer tuned at 650 nm and from figure 2.19 results evident that this wavelength is close to the maximum of the energy emission density, as stated by Wien's law. So, if this is the case, to find the maximum eq. (2.5) can be derived and equating to zero, posing $x = \frac{h\nu_{max}}{k_B T}$ we obtain:

$$x = 3(1 - e^{-x}) \tag{2.7}$$

Which can be easily solved graphically, as shown in figure 2.20:

$$h\nu_{max} = 2{,}8214 k_B T \tag{2.8}$$

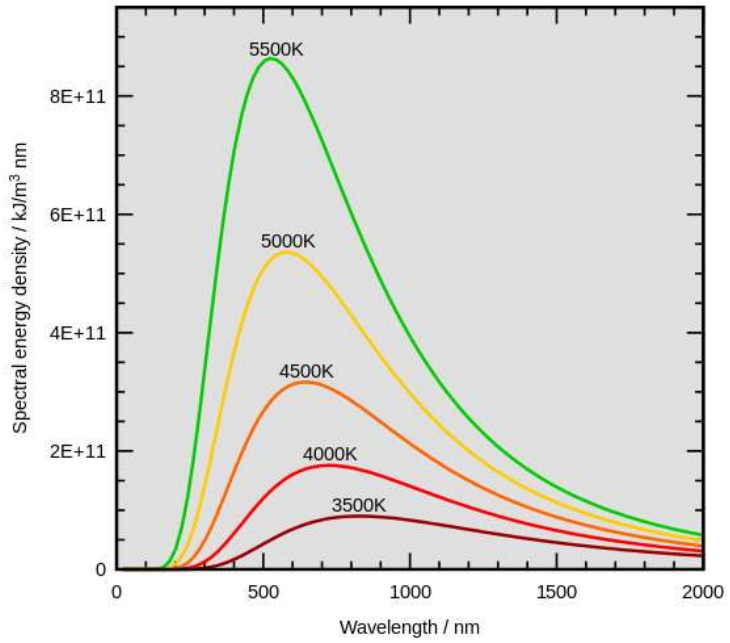

Figure 2.19: Wien's law for spectral energy density. It can be seen that, 650nm is fairly close to the maximum relative to the expected temperatures (~3000 K)

Which is proving that, if the recording device is in close vicinity of the energy emission density maximum, we have:

$$e^{\frac{h\nu}{k_B T}} \gg 1 \qquad (2.9)$$

Now, defining $c_1 = 2\pi hc^2$ and $c_2 = \frac{hc}{k_B}$, equation (2.6) can be converted to:

$$M(\lambda, T) = \frac{c_1}{\lambda^5} \frac{1}{e^{\frac{c_2}{\lambda T}} - 1} \qquad (2.10)$$

Where M defines the total radiance exitance from the surface. If we divide by π, the specific radiance is obtained, defined here by the letter L instead of B for consistency with the I.S.:

$$L(\lambda, T_\lambda) = \frac{C_{1L}}{\lambda^5} \frac{1}{e^{\frac{C_2}{\lambda T_\lambda}} - 1} \qquad (2.11)$$

With $C_{1L} = 2hc^2$. L is the quantity detected by the optical instrumentation, thus the recorded temperature T was corrected with T_λ in order to distinguish between the real temperature (T) and the radiance temperature T_λ measured by the device.

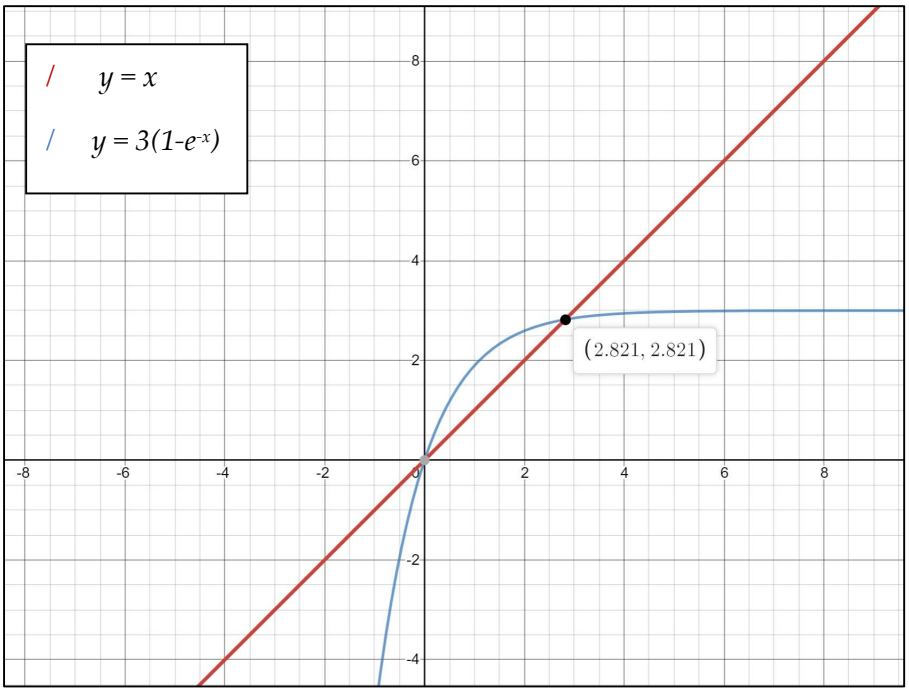

Figure 2.20: Graphical solution of eq. (2.7).

Now if the definition of emissivity is considered, we obtain:

$$\tau\varepsilon = \frac{L_\lambda}{L_\lambda^0} \qquad (2.12)$$

Where τ is the optical path transmittance, ε is the spectral emissivity, L_λ is the spectral radiance at the considered wavelength and temperature detected by the instrumentation and L_λ^0 is the spectral radiance of a black body at the same temperature and wavelength. The transmittance was taken into account in order to correct for the optical path attenuation on the photodetectors (i.e. T_λ). If one substitutes eq. (2.11) into eq. (2.12) obtains:

$$\tau\varepsilon = \frac{e^{\frac{c_2}{\lambda T_\lambda}} - 1}{e^{\frac{c_2}{\lambda T}} - 1} \qquad (2.13)$$

Now if the approximation (2.9) is considered, eq. (2.13) becomes:

$$\tau\varepsilon = e^{\frac{c_2}{\lambda}\left(\frac{1}{T_\lambda} - \frac{1}{T}\right)} \qquad (2.14)$$

Which can be easily rearranged as:

$$\frac{1}{T_\lambda} = \frac{1}{T} - \frac{\lambda}{c_2} ln(\tau\varepsilon) \qquad (2.15)$$

That underlines how, in the present case, linearity on λ can be exploited to obtain information on emissivity. In fact, λ, c_2, and τ are known, $\frac{1}{T_\lambda}$ is recorded directly by the spectrometer as stated in eq. (2.2), so if the latter result is to be well approximated by a straight line, like:

$$y = ax + b \qquad (2.16)$$

emissivity can be obtained by the slope computed by linearization:

$$\varepsilon = \frac{1}{\tau} e^{-c_2 a} \qquad (2.17)$$

While b is the inverse of the real temperature. An example is reported in figure 2.21, in which a typical experimental $\frac{1}{T_\lambda}$ curve obtained in this work is plotted against a linear fit, from which the slope is obtained, and emissivity is calculated with eq. (2.17). As it can be seen, the fitting is very well approximating the curve, meaning that the initial hypothesis is attained, and that the overall procedure is consistent, similarly to analogous relevant literature results [6] [25]. The curve obtained in figure 2.21 is representative of a portion of the emission spectra of between 550 nm e 850 nm at one specific time. Thus, by performing more subsequent acquisitions, it is possible to plot the emissivity as a function of time (or equivalently temperature in the present case), examples are reported in the following chapter (figures 3.1 – 3.3).

Another major concern linked to the data analysis was the exact assessment of the PTT that was often hard to identify, due to the very reduced amount of material involved. Whenever possible an undercooling shoulder was exploited to recognise the solidification temperature [10]. This phenomenon is widely used in literature and is directly dependent from the Gibbs phase law (2.18):

$$F = C - P + 2 \qquad (2.18)$$

Where F is the number of independent intensive quantities, C is the number of components in the system and P is the number of phases.

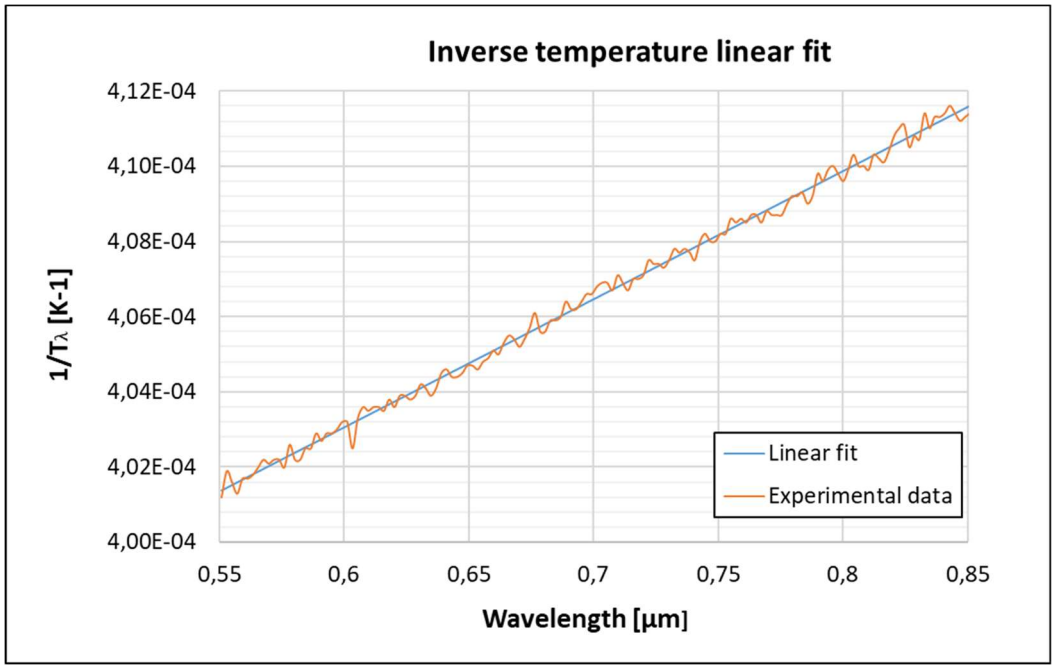

Figure 2.21: Linear fit of the $\frac{1}{T_\lambda}$ experimental data. As it can be seen, the fitting is very well approximating the curve, meaning that the initial hypothesises are attained.

In a system with 1 component the number of degrees of freedom reaches 1 as soon as 2 phases are present in the system (i.e. at melting point), so if the pressure is constant, the temperature must remain constant, generating a plateau that is called thermal arrest. In the present case the number of components is 2, thus the number of independent quantities reaches a minimum of 2 when 2 separate phases are present in the system, so a complete thermal arrest is impossible even controlling the pressure. What is observed then, is an abrupt changing in the temperature gradient in correspondence of two points defining the beginning (solidus) and the end (liquidus) of the PT, that is due to the beginning of latent heat being released (or absorbed) during the process. These points can be very difficult to detect if the mass undergoing PT is reduced and the resulting slope change is not very evident, luckily this problem can be solved taking advantage of a property of the solidification process. Whenever a liquid is undergoing cooling at a sufficiently high rate (3E03~6E03 K/s), the solidification temperature can be reached and passed through, generating what is called to be an

undercooled state. This is possible because the solidification process is not given enough time to properly develop starting from the first solid seeds, which, by growing, would release latent heat and slow down the cooling rate. Of course, the higher the undercooling, the faster will be the resulting grain growth (i.e. heat release) and therefore the smaller will be the time required to compensate for the undercooling effect. The temperature then rises to a value and then starts again to decrease following the normal PT cooling rate. This phenomenon creates shoulders in thermograms, similar to the one reported in figure 2.22, which clearly identifies the PTT, since the induced accelerated grain growth will compensate the undercooling effect up to the liquidus point but not further. Although this is known to be a very easy and precise method, it revealed to be not extremely reliable at the extremes compositions (i.e. 20 and 80 at% Pu), where, due to low concentration of one of the two species, either the solidus or the liquidus couldn't be observed clearly by this mean. Whenever the thermal arrest technique was not available, the PTT was determined by exploiting the Reflected Light Signal technique (RLS).

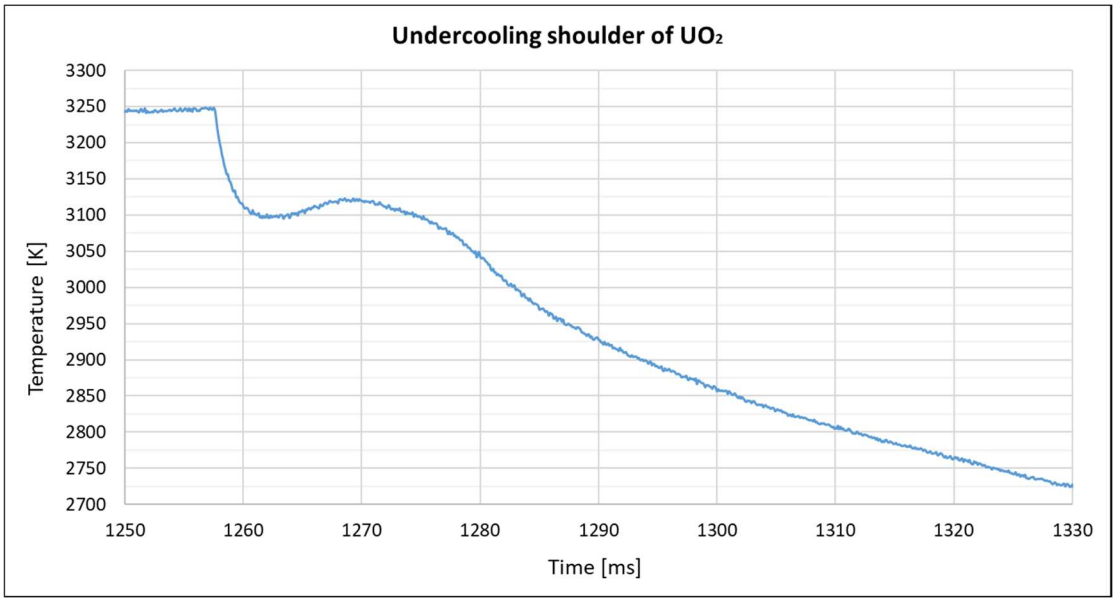

Figure 2.22: Typical example of undercooling shoulder. The present case is the calibration test of OLGA performed on stoichiometric UO_2, the maximum of the shoulder is close to 3120 K, which matches literature data of PTT for this compound within uncertainties margins.

This method [9] [25] [26] is based on the main idea that during every phase transition some superficial properties of the sample are expected to change. In particular, as soon as the first liquid drop is formed during melting, the reflectivity of the surface is expected to increase abruptly, thus if one is capable of detecting the exact moment in which this happens, can easily obtain the PTT from the recorded thermogram. During the heating stage the liquid mass will vibrate, creating a very blurry signal that will drop to a constant level as soon as the first solid seed is generated in the focus spot of the pyrometer. This is why in the previous paragraph the blue laser was introduced and the second channel of the pyrometer tuned at 488 nm. By doing so and with careful alignment, the direct reflection of the blue laser from the sample could be detected, thus the second channel pyrometer voltage is directly proportional to the light intensity coming from the sample, i.e. its reflectivity. Plotting then the derivative of this signal against a thermogram a result like the one in figure 2.23 is obtained. If the temperature profile and the RLS derivative plots have the same timescale, it is possible to directly superimpose them in order to detect the solidus or the liquidus in correspondence of each sharp change of the signal during cooling. Nevertheless, also by this mean, it was not always straightforward to clearly identify the signal from the noise, indeed due to the presence of a low melting point phase (Fe oxide) that was brought at the higher melting point (Pu oxide) PTT, generating a considerable amount of liquid in the molten pool that induces high level of disturbances to the measurement. In fact, the sample's surface could undergo radical changings during solidification that obviously affected its angular reflectivity, either reducing or distorting the signal of the blue laser recorded by the pyrometer. In practice, this led to only a reduced availability for this technique, that yet was capable of delivering interesting results.

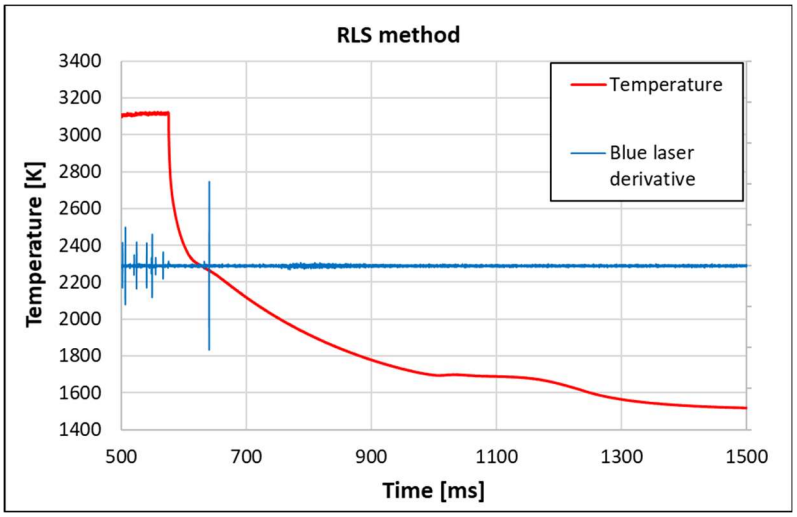

Figure 2.23: Typical thermogram for the RLS method. In the present case the liquidus PT is highlighted via RLS technique and the solidus by a small thermal arrest.

As last available option the thermogram slope change was used to visually determine the most probable PTT. The reduce sensitivity of this method is a common problem whenever dealing with multi-phase systems in which one component will always be cooling down, regardless of the thermal arrest of the other one [26]. What results is rather a slope change more than a clear arrest, nevertheless, identifying the exact point of the slope variation should deliver accurate enough result for PD determination. In this work this latter method was solely used as a confirmation of repeatability of the solidus points for some compositions. Since the solidus point revealed to be an eutectic line it is enough to have one clear measure for all the compositions in order to obtain the exact value, the close vicinity of the other registered points works as a confirmation of that measure.

2.4 Uncertainty estimation

Since the main result of this work is not only the improvement in the state of the art of the melting point assessment, but also the experimental evaluation of thermal properties, a good estimation of the relative uncertainties is vital for

further exploitation of the data obtained in this framework. Unluckily, some usual solutions in experimental science could not be exploited on this regard, due to the specificity of the project and its intrinsic limits (i.e. high costs, material and time availability, etc). For example, the model presented in this chapter could not take advantage of a high number of statistical relevant points, for the measurements could be performed only a limited number of times before the collapse of the sample. Nonetheless, many precautions were taken at different stages, both during calibration and test performing, in order to reduce uncertainties to the lowest extent possible.

As described in literature [25] [28], estimation of the uncertainty relative to optical pyrometry for applications alike the presented one is based on several factors, namely the propagation of the calibration uncertainty on the measured data and the estimation of the error on the emissivity calculation, considered as totally independent. Moreover, a separate contribute will be taken into account for the intrinsic inaccuracy of the analogic to digital signal converter, obtaining:

$$\delta T(T_\lambda, \varepsilon, \delta T_{rel}, \delta V) = T^2(\lambda, T_\lambda, \varepsilon)\sqrt{\left(\frac{1}{T_\lambda^2}\delta T_\lambda(T_\lambda)\right)^2 + \left(\frac{\lambda}{C_2}\delta\varepsilon\right)^2} + \delta V \quad (2.19)$$

Where δV is the abovementioned contribute of the relative error for the I/O converter to the overall uncertainty. This term was calculated as prescribed by its manufacturer as follows:

δv = Reading · (gain error) + Range · (offset error) + Noise Uncertainty

Where all the terms apart from the reading are known a priori. It is interesting to note also that this formulation inherently takes into account statistic noise uncertainty on a sample of N points, considering a 3-σ coverage and averaging:

$$\text{Noise uncertainty} = \frac{Random\ noise \times 3}{\sqrt{N}} \quad (2.20)$$

Thus, obtaining a more statistically accurate value. δv is referring to an error on the voltage obtained by the NI 6366, it is necessary to propagate it as temperature uncertainty via eq. (2.3), so:

$$\delta V = \frac{B}{(v+\beta\, lo\ _{10}(\tau\varepsilon)-A)^2}\,\delta v \qquad (2.21)$$

The two terms inside the square root of eq. 2.19 are representative of two different contributions coming from different devices and methods, then they were calculated separately. The first term of eq. (2.19) is the uncertainty on the radiance temperature obtained by the OLGA pyrometer, thus it is mainly dependent on the calibration of the device and its operative conditions and was calculated as follows:

$$\delta T_\lambda = T_\lambda^2 \sqrt{\left(\frac{1}{T_\lambda}\frac{\Delta B}{B}\right)^2 + \left(\frac{\Delta A}{B}\right)^2 + \left(\frac{\Delta\beta \log\tau}{B}\right)^2 + \left(\frac{\beta\Delta \text{ lo}}{B}\right)^2} \qquad (2.22)$$

Where A, B, and β are calibration parameters for the pyrometer, τ is the transmittance of the optical path and with Δ is intended their absolute uncertainties, always assuming that every contribute is independent.

The second term in the square root of eq. (2.19) is related to the uncertainty on emissivity and how this impacts the overall measure. Since emissivity was found indirectly, $\delta\varepsilon$ can be obtained estimating the error during the linearization process. To compute this value, we define:

$$ss_y = \sum_{i=1}^{n}(y_i - \bar{y})^2 \qquad (2.23)$$

$$ss_x = \sum_{i=1}^{n}(x_i - \bar{x})^2 \qquad (2.24)$$

As the Sum of Squares, which represents the scatter of each experimental point compared to the average of the spectrum both for x and y. While we also define:

$$ss_E = \sum_{i=1}^{n}(y_i - \hat{y}_i)^2 \qquad (2.25)$$

That is the Sum of Squares relative to the error between the real value (y_i) and the one predicted by the linear model ($\hat{y}_i$). From these we can easily obtain:

$$\sigma = \frac{1}{n-2}\sum_{i=1}^{n}(y_i - \hat{y}_i)^2 = \frac{ss_E}{n-2} \qquad (2.26)$$

Which is the variance of the function *y(x)*. From that we can compute the standard error of the slope, which delivers:

$$\delta\varepsilon = \sqrt{\frac{\sigma}{ss_x}} \qquad (2.27)$$

That represent the uncertainty induced by the linearization process on the emissivity. This value was then propagated in the (1.19) accordingly to error propagation law, obtaining the uncertainty on temperature. Performing the calculations listed above the numerical values reported in table 2.1 are obtained considering a coverage factor of 2 on δT so to have a 95% confidence interval on the resulting values:

Table 2.1: Uncertainty estimation at the temperature range extremes with the relative contribution of each term of eq. 2.19

T = 3000 K				
Composition	**Uncertainty [K]**	**Acquisition %**	**Emissivity %**	**Analog conversion %**
20%	**26,52030251**	50,55879621	10,82417378	38,61703001
40%	**26,47262508**	50,02764591	11,35532408	38,61703001
60%	**26,44529816**	49,68574384	11,69722615	38,61703001
80%	**26,40572618**	49,12463801	12,25833198	38,61703001
Relative error = 0.88%				

T = 1500 K				
Composition	**Uncertainty [K]**	**Acquisition %**	**Emissivity %**	**Analog conversion %**
20%	**7,740139037**	60,1191491	6,802218544	33,07863235
40%	**7,735010277**	59,75346225	7,167905399	33,07863235
60%	**7,73225695**	59,51633474	7,405032907	33,07863235
80%	**7,728610627**	59,12419769	7,797169954	33,07863235
Relative error = 0.51%				

Given the abovementioned equations, it is clear that the resulting uncertainty is both temperature and concentration (i.e. emissivity) dependent. For the sake of brevity only the extreme temperatures of the considered range are reported, highlighting instead the dependence on concentration. As could be expected, nonlinear behaviours are shown, both for the total value of the uncertainty (increasing with temperature, and slightly decreasing with emissivity) and for

the relative weight of each term. In fact, at higher temperatures the contributions of emissivity and the inaccuracy induced by the converter increase considerably, due to the higher voltage output and the emissivity uncertainty enhanced by non-linear detection efficiency at high count rates of the spectrometer. On the contrary, fixing emissivity, the higher the temperature the lower the influence of the pyrometer calibration on the measured value, reduced by the increased number of counts on the photodetector (i.e. statistical scatter reduction due to increased sample population). The described formulas are the ones that will be used in the following paragraphs to compute the uncertainty relative to every reported data. When reporting values relative to emissivity, calculation showed that the expanded relative uncertainty (2-σ) is around 0.85~0.9% thus, for the sake of simplicity, this value is going to be rounded up to 1% so to be conservative while maintaining a high confidence interval.

Concluding remarks. The second chapter of the present work fully describes the preliminary part of the experimental work performed at JRC Karlsruhe. In particular, the samples fabrication process is explained, together with the preliminary evaluation of their quality by means of XRD and SEM, confirming the suitability of pellets for melting point assessment. In the second part of the chapter the experimental set-up was shown, passing through a detailed overview of the instrumentation, the relative calibration and the model used to work on the experimental data to obtain the results discussed in the following chapter. Not only the main equations were shown, but also the underlying hypothesis, together with the demonstration of their validity in the present framework. At last, a complete overview of the uncertainties of the presented method is discussed, reporting how the problem of error propagation was dealt with both for temperature and emissivity estimation.

3. Results and discussion

3.1 Introduction

The present chapter shows the result obtained while studying the PuO_2-Fe_3O_4 system, most of them regard the study of the effects of oxidation state changings on PTTs and the interpretation of the thermograms obtained from the experimental set-up described before, in order to obtain the PD in different atmospheres. Together with this, a brief examination of the sample emissivity will be performed exploiting data obtained from the 256 channels spectro-pyrometer. At the end of the chapter the after-melting sample characterisation with SEM and XRD is reported.

Experiments were performed on samples of different concentrations, in order to characterize the whole spectrum of compositions in different atmospheres (air and argon). As already stated in the preliminary part of this thesis, the importance of this system in nuclear engineering is critical for several reasons, on the one hand because of the lack of specialised literature, and therefore the almost complete absence of experimental data, on the other hand because of its future applications for fuel design and in the modelling of fuel behaviour under accidental conditions [1] [2] [14]. The studying of plutonium as possible alternative to uranium in nuclear engineering has always been a relevant subject, which saw increasing interest by the scientific community after the introduction of MOX fuels, of which full knowledge of chemico-physical properties is not available yet.

On that regard, an interesting improvement of the melting point experimental method will be shown in this chapter, in order to keep trace of the oxidation changings of the sample during measurements.

This is known to be a fundamental parameter to have under control during melting point examination, because of the strong dependence of the melting point on chemical composition.

3.2 Emissivity of PuO_2-Fe_3O_4

When dealing with optical thermometry, the evaluation of the spectral emissivity ε of the sample is of primary importance to properly correct the Planck's law of radiation (eq. 2.5) and obtain the true surface temperature from the radiance temperature recorded by the instruments (eq. 2.15) [28]. This can be assessed in several ways depending on the accuracy needed, the instrumentation availability and the specific application. In this case, emissivity was obtained by means of a 256 channels spectro-pyrometer and the implementation of the resulting data into a specific program.

In general, emissivity is to be considered a function of wavelength, angle and temperature, thus its determination is usually very complicated. Nevertheless, in the present work several simplifications may be applied to reduce the order of the problem. In particular, it is well established in literature that the grey body assumption is reasonably valid when applied to oxides like those used in the present work [10] [20] [23] [27], practically removing wavelength dependence on ε and justifying the exploitation of Wien's approximation on Planck's law. The applicability of this hypothesis was also confirmed by the linearity check performed on the $1/T_\lambda$ spectra, as mentioned in section 2.3.2. Angle dependence can be also disregarded for small deviations from normal as in this specific case, contributing only as a secondary effect [23]. Unfortunately, nothing could be stated a priori on the temperature dependence, which had to be investigated experimentally.

The results obtained showed a slight dependence on composition, that was attributed to the different structure of the two species constituting the surface

during each measure. That is coherent with the emissivity being a superficial property and thus predictably affected by relative composition.

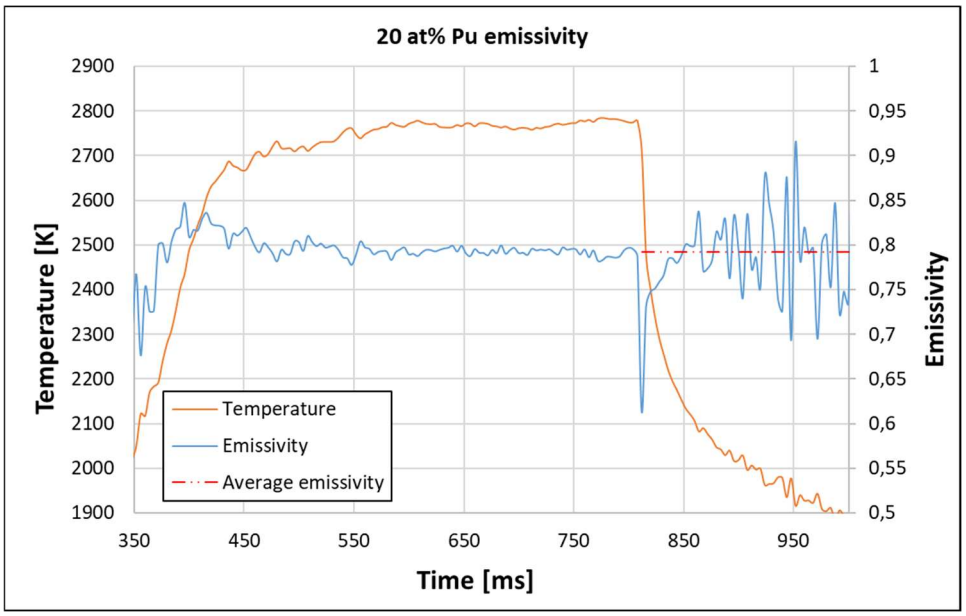

Figure 3.1: Emissivity of the 20 at% Pu composition, obtained by linearization of the inverse of the radiant temperature.

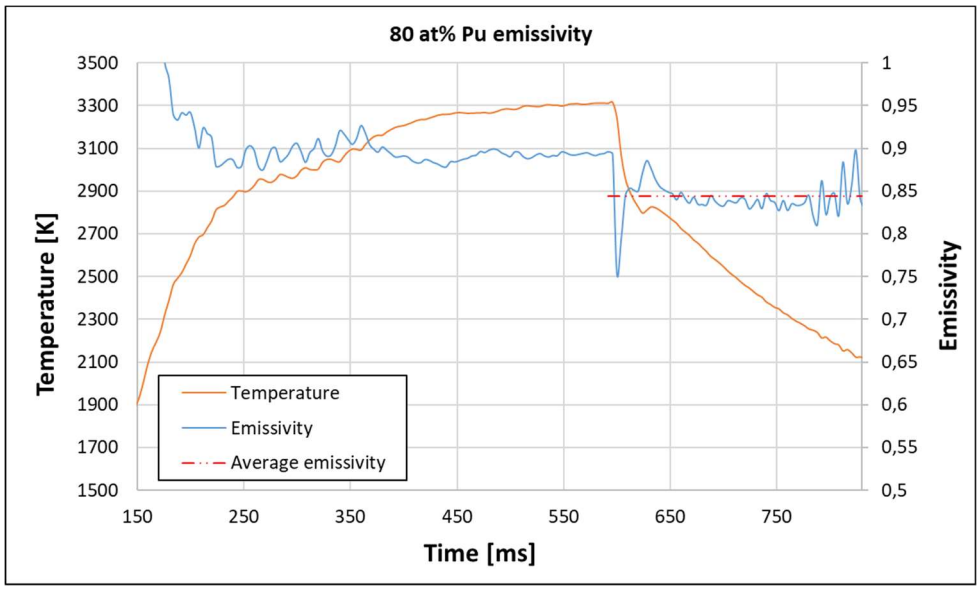

Figure 3.2: emissivity of the 80 at% Pu composition, obtained by linearization of the inverse of the radiant temperature.

As reported in figures 3.1 and 3.2 the recorded values range from 0.782 ± 0.008 for the 20 at% of Pu to 0.845 ± 0.008 for the 80 at% of Pu composition and are observed to be constant during the PT in the whole temperature range of interest, further simplifying the computation of the temperature. It is important to point

out that the emissivity value was chosen as the average of the points obtained after the end of the laser pulse. This criterion showed to be reliable in this kind of experiments, because not only cuts off the increasing noise in the right part of the curve (due to decreasing temperature), but also delivers a value that is representative for the whole cooling down process. It is interesting to note, in fact, that emissivity of the liquid could be significantly different (usually higher for these compounds) than the one taken into consideration.

Due to this regularity, a linear dependence was hypothesised exploiting a Vegard's law, that could be expressed as follows:

$$E_{1+2} = E_1 x + E_2(1 - x) \qquad (3.1)$$

Where E_1 and E_2 represent the emissivity of PuO_2 and Fe_3O_4 respectively, while x is the molar concentration of PuO_2 in the mixture. Pure PuO_2 emissivity has already been estimated in previous works [27] and it's known to be close to 0.83 ± 0.05. Pure Fe_3O_4 emissivity data were hard to find and relative to less precise measurements than the one reported in this work, so its emissivity was experimentally investigated as shown in figure 3.3. Since emissivity is (in general) temperature dependent, it was decided to assess it as close as possible to the melting point, in order to have a reference value for the Fe_3O_4 solid at high temperature. The technique exploited was the same used for the PuO_2 - Fe_3O_4 system, with the only difference being the longer integration time used. In fact, since the measurement carried out on the binary system is involving very small time scales and higher temperatures, it is thus necessary to use the shortest integration time allowed by the instrument, in our case 4 ms. This allows not only to possibly highlight some feature of the PT (like the small undercooling shoulder visible in figure 3.2), but also to avoid saturation of the photodetectors.

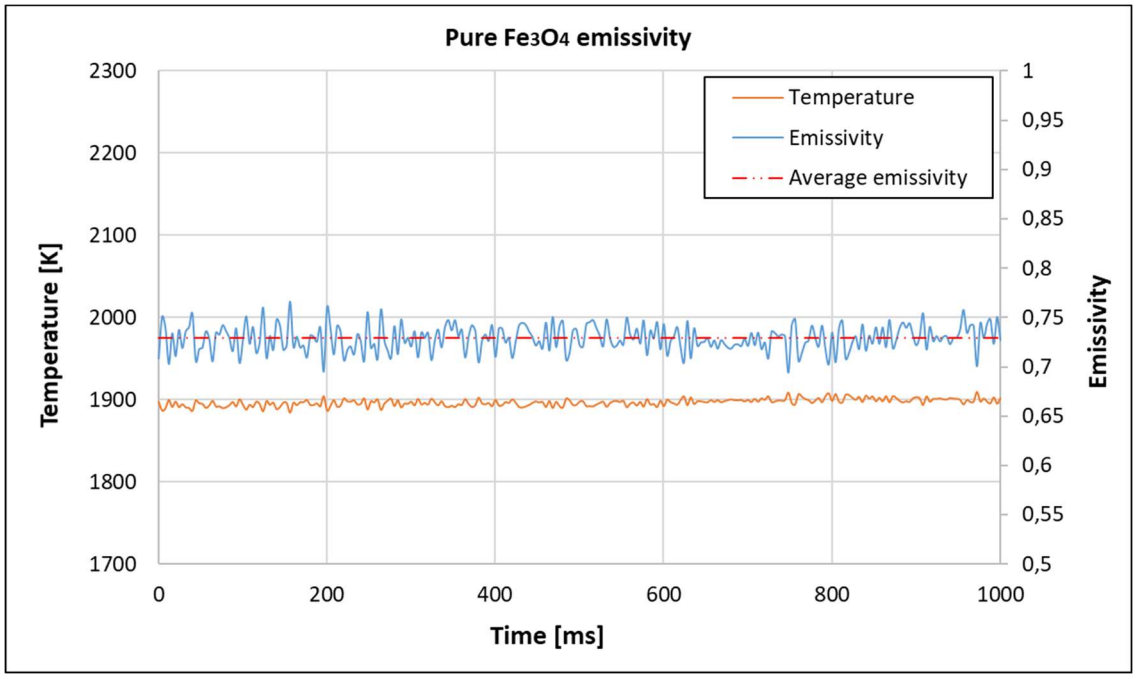

Figure 3.3: Pure Fe_3O_4 emissivity measured at constant temperature, close to the melting point.

For pure iron oxide this was not necessary, because of the lower temperature a wider integration time (up to 24 ms) was used in order to increase the number of counts on photodetectors. This value was chosen because it represents a good compromise between number of counts registered and the total measurement time. As it is evident in figure 3.3, temperature was kept constant during the experiment to increase accuracy of the measurement, nevertheless, maintaining a temperature close to melting point for long times could affect the sample's structure, thus it is essential to avoid unnecessary wide integration times. Since the spectro-pyrometer records 256 spectra the total measuring time is then 6.1 sec, definitely higher than 1.024 sec necessary for fast measurements with 4 ms integration time, but still bearable by the sample. As reported in the figure above, the emissivity obtained for pure Fe_3O_4 at about 1900 K was 0.729 ± 0.0073, below the emissivity of the 20 at% Pu composition (as expected), and consistent with the hypothesis of composition dependence and coherent with a linear Vegard's law as shown in figure 3.4.

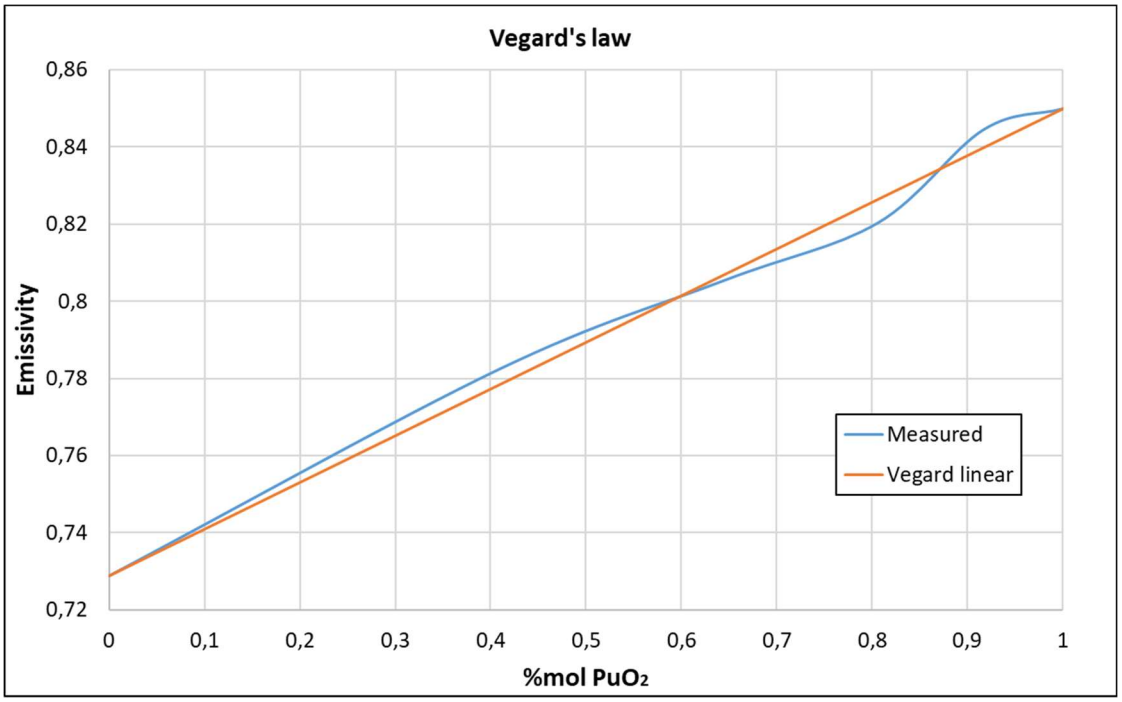

Figure 3.4: Emissivity expressed as a function of %mol of Puo_2. It appears clear that a linear correlation could be extrapolated from the data exploiting a Vegard's law.

Vegard's law delivers good approximated results, especially at low PuO_2 concentration. For the present work the results found are within the requirements for a precise estimation of the liquid-solid transition, however the experimental determination of the emissivity for such infrequent compounds should be matter of deeper analysis in order to broaden availability of optical thermometry data for similar applications.

3.3 Phase transition temperature dependence on atmosphere

The PTT is a property depending strongly on the composition of the sample under consideration. For this reason, many precautions were taken in the present work in order to avoid external contamination. Self-crucible conditions are guaranteed by a small laser spot compared to the sample diameter, resulting in uniform melting on a very limited area, which by no means gets in contact with external media apart from the atmosphere gas.

Notwithstanding the relevant difficulties linked to the sample characterisation during melting point assessment, in the present work an interesting

improvement was done in this direction: the experimental apparatus was set in such a way undergoing reduction of the sample could be detected and quantified non-destructively a posteriori. To do so, parallel to the optical thermometry scheme, an oxygen gauge was mounted feeding a constant flux of 5 l/h at 2 bars from the experiment vessel to the gauge, recording the oxygen partial pressure in the flow (figure 2.15). If the sample undergoes reduction during the experiment, oxygen is supposed to be released in the chamber and then inevitably detected by the gauge, resulting in a sudden increase in the oxygen partial pressure up to a maximum that slowly fades until the minimum threshold value is reached and the registration is stopped. This technique allows to disregard completely complex phenomena of mixing and transport that are expected to happen in the close vicinity of the sample's surface during reduction at high temperatures which must be taken into account in any numerical model of superficial dispersion [16]. Since the measurement is indirect, and based on the exiting flow composition, a certain time is required for it to be completed depending on the amount of oxygen released, i.e. stronger reductions lead to longer measuring times. Moreover, a fixed delay is observed due to the diffusion processes of O_2 in the chamber atmosphere and the time required for the gas to reach the gauge trough piping.

In order to investigate the effects on the PTT of the experimental environment, measurements were taken in inert (argon) and oxidising (air) atmospheres.

The necessity of the apparatus described above became evident when it was clear that no repeatable measure could be registered on a fresh sample in argon, while that was not the case for air measurements. In fact, what was recorded in inert atmosphere was a progressive decrease of the PTT with every subsequent pulse from the Nd:YAg laser. This behaviour was attributed to a possible undergoing reduction of the sample during the experiment. To investigate this phenomenon

an appropriate trial was set, on a fresh sample of 80 at% Pu measures were performed in air and the results (pulses 1 – 2, fig 3.5), which showed low scattering (below 0.5%) and good repeatability, were taken as a reference value. The atmosphere in the chamber was then changed to argon, eliminating every trace of air by means of a high vacuum turbo pump (up to 1E-06 hPa), and multiple measurements were taken (pulses 3 – 6, fig 3.5), recording a clear decreasing of the PTT, down to 80 K less than the reference value. At this point the atmosphere was changed again to air, after vacuum was made likewise stated above, and new shots were performed on the same surface (pulses 7 – 10, fig 3.5). What was recorded was an evident subsequent increase of the PTT from the lower value found in argon up to the reference value in air. After only 3 laser pulses the measures returned well into the scatter band of the initial reference values, proving that the influence of the gas in the chamber could not be neglected. The resulting thermograms are reported in figure 3.5.

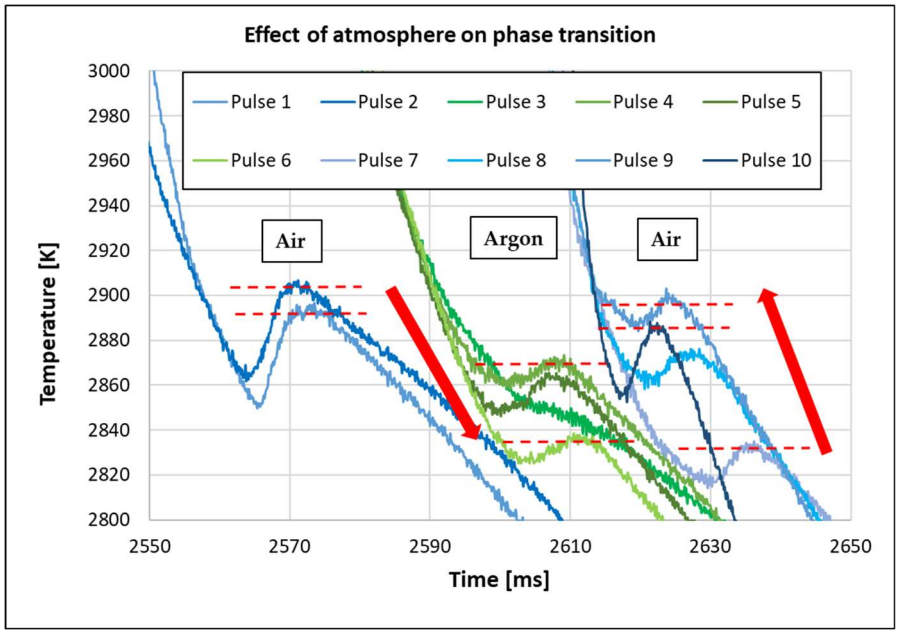

Figure 3.5: Effects of atmosphere on PTT. It can be seen in blue the reference values(1-2), in green the successive reduction of the sample (3-6) and in blue again its re-oxidation to the original state (7-10), PTTs are highlighted with red lines. It is interesting to note how the PTTs first decrease and then increase back to the original value.

Alongside with temperature, for the first time, the amount of oxygen released was recorded too, as shown in figure 3.6. The gauge detected an increase of O_2 in the flow after every shot performed in Ar, confirming that the sample is actually losing oxygen during the experiment, coherently with the lowering of the PTT at every subsequent measure. As reported, the partial pressure growth in the gas flow following the sample reduction is very small and thus hard to detect if equilibrium conditions with low O_2 concentrations are not granted. Unfortunately, due to its constitution, the oxygen gauge accuracy is relative to the value recorded, strictly reducing its utilisation range at only suitable atmospheres (i.e. low O_2 concentrations) and delivering unusable results in air due to high background noise.

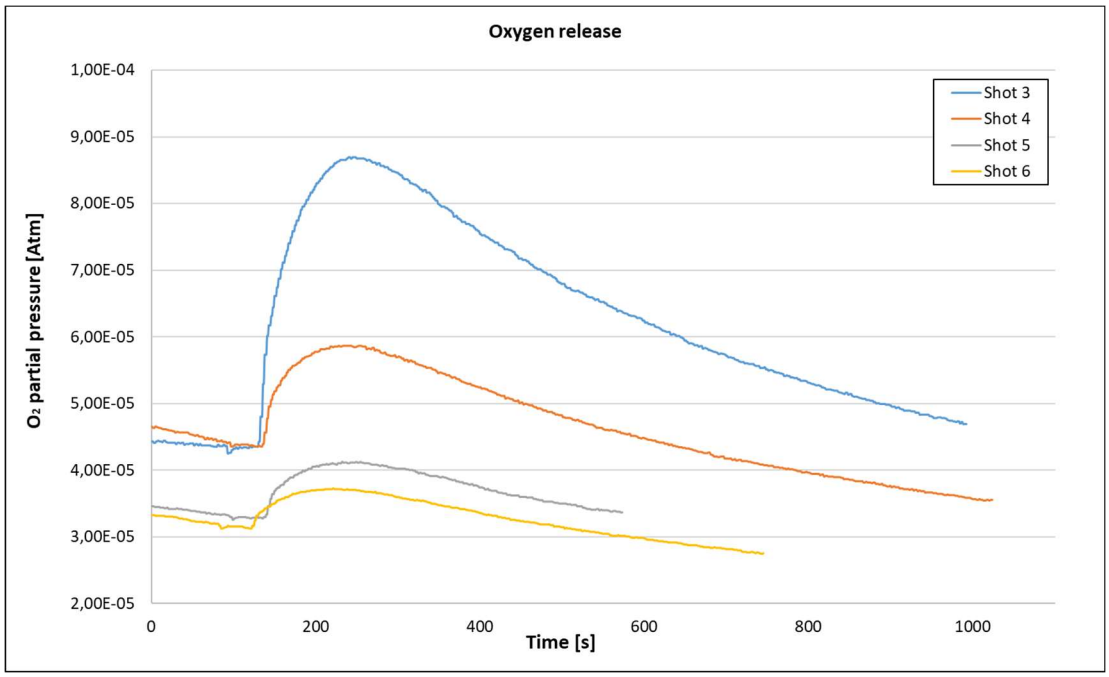

Figure 3.6: Oxygen partial pressure increase in the atmosphere measured by the gauge after every subsequent laser pulse in argon. This increase is to be attributed to a direct O_2 release at high temperature from the sample.

Nevertheless, the sequential raising of the measured PTT is delivering a cross check that something similar to what recorded in inert atmosphere is undergoing in the oxidising environment but in the opposite direction, thus is logical to assume that the sample surface, exposed to high temperatures for relatively long

period of time in an oxygen-rich environment, re-oxides delivering again the same results as the reference values. It is worth noting that the values recorded during this trial are in perfect agreement with the results obtained for the 80 at% Pu concentration reported in table 3.1 and appendix A. Another confirmation of this hypothesis comes from the direct observation of the sample after every measure. By means of the camera inside the glovebox pictures were taken, showing interesting results, as reported in figure 3.7. After the reference pulses were performed the molten pool surface appears to be matt-like, then as soon as the gas composition is changed to Ar and shots are performed a more glossy aspect is shown, coherent with the tipycal features of oxides and metals.

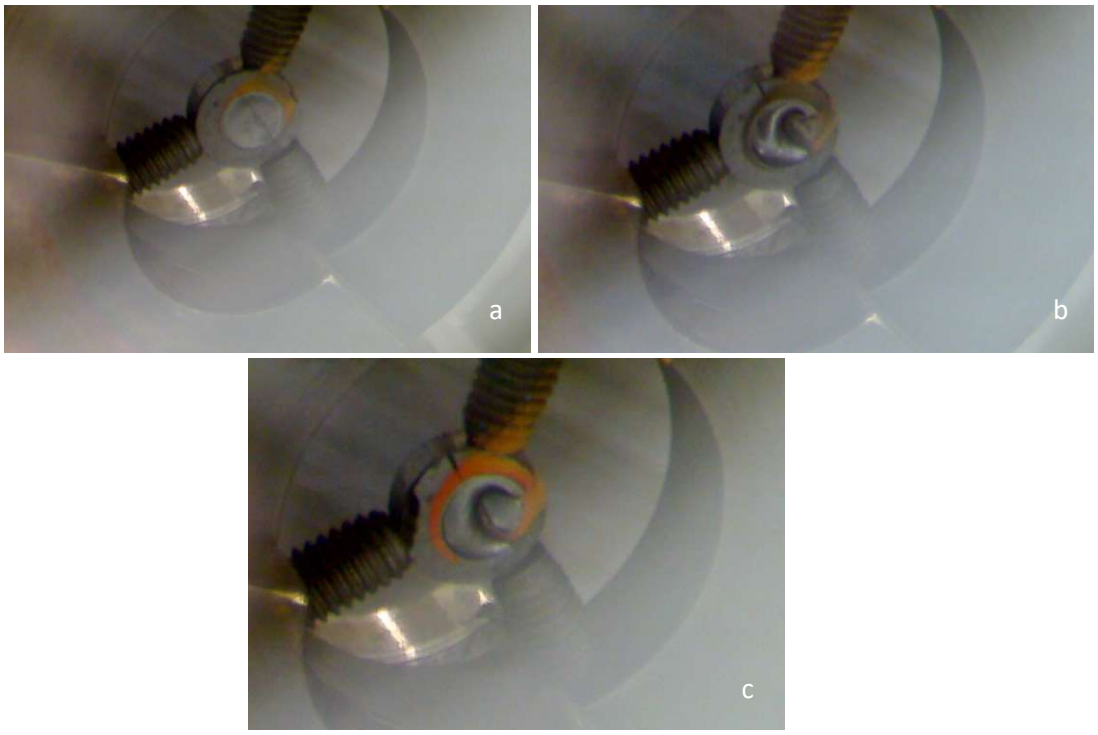

Figure 3.7: Evolution of the trial sample surface with the progressive change of atmosphere: a) air b) argon c) air. It can be seen that the aspect of the surface changed evidently from an oxide-like (a) to a metal-like (b) and the again oxide-like (c).

Again, as soon as the atmosphere is switched back to air and measurements are taken, the sample's surface returned similar to its original state. Concluding, it may also be observed in the above pictures that all the experiments were performed exploiting a self-crucible setting, granting that no chemical

contamination could take place between the molten zone and any other external media.

3.4 PTT determination

Coherently with what exposed in the previous paragraph it is clear that not one, but two PDs need to be traced, remarking the effects of oxidising and reducing atmospheres on the PTT.

We can start now analysing the experimental results of this work; all the experimental measures have been carried out with the instrumentation and methods exposed in chapter 2, a typical example is reported in figure 3.8. Thermograms consist of the computed temperatures profiles detected by the 2-channel fast pyrometer fed with the emissivity value obtained from the analysis of spectrometer data.

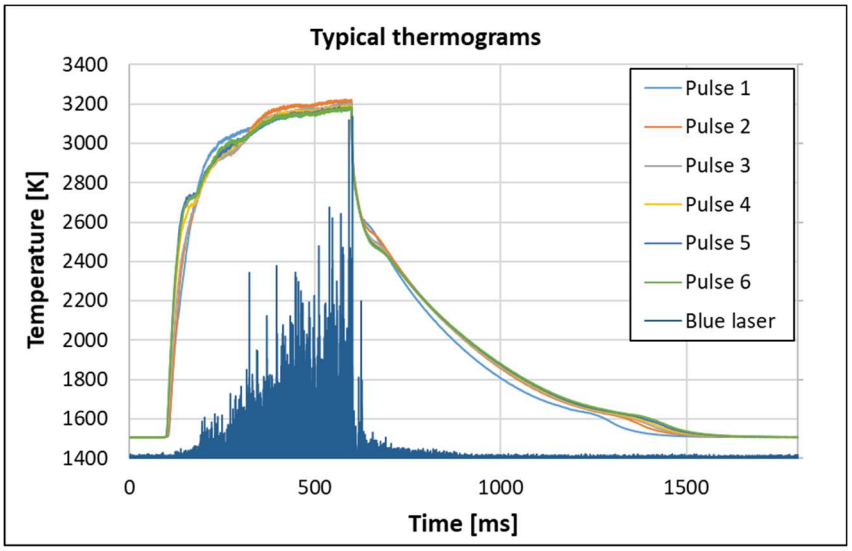

Figure 3.8: Example of resulting thermograms from the melting experiments on a 60 at% Pu in air. Thermograms are overlapped in order to show the repeatability of the results and their characteristics. In the plot are also reported the recorded blue laser signal and its first derivative, often used to identify the PTT.

As it can be noticed, the lower recordable value for this pyrometer is 1500K, so in order to check linearity of the instrument close to its operation limit another low-temperature pyrometer was used in parallel. What appears in the graph is a step increase in temperature due to the beginning of the laser pulse that will heat the

sample up to a stationary value in which the energy delivered by the laser equals thermal losses. After 500 ms, which was observed to be enough to both reach equilibria and high enough temperatures, the pulse finishes and temperature decreases with a gradient of approx. 10^4 K/s. At this time both species are liquid but, as soon as the liquidus point is reached, one of the two starts solidifying, inducing an effect resembling a thermal arrest. This actually appears more like a slope change than a real thermal arrest, due to the high cooling rate of the other component which is still liquid and then still subjected to intense cooling [10]. Since pulses were performed in air, it can be noted that all the temperature profiles almost overlap perfectly delivering consistent results. This will not be the case for the inert atmosphere as discussed above and shown the following part of the chapter. For the sake of simplicity, the analysis of only one composition for each atmosphere and the relative interpretations of the results obtained from the oxygen gauge are reported, leaving the remaining part of the data in appendix A.

3.4.1 Melting experiments in Air atmosphere

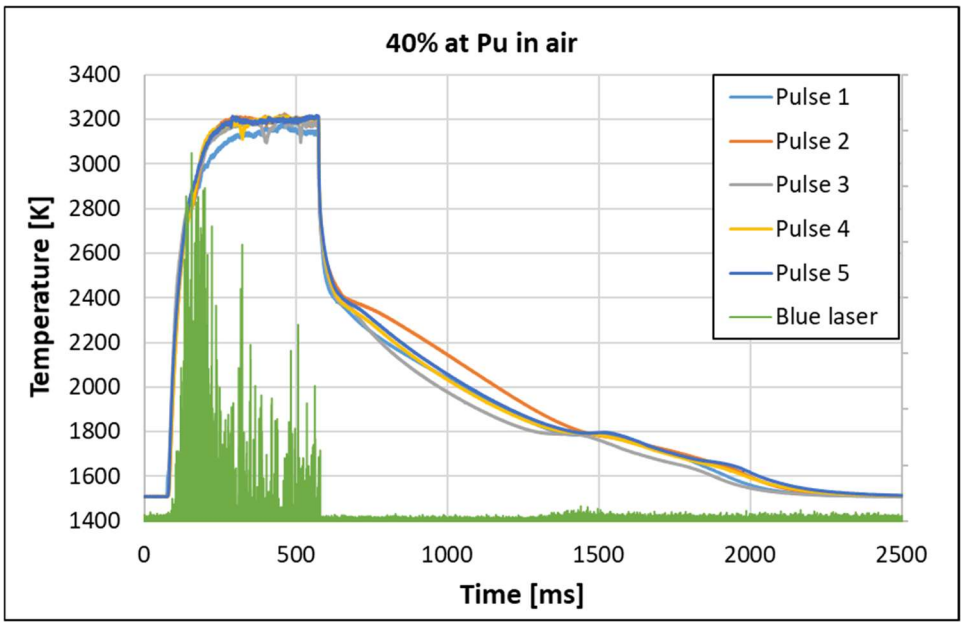

Figure 3.9: General overview of the thermograms measured for the 40 at% Pu sample in air atmosphere.

The first measures that will be considered are the one regarding a non-reducing environment, i.e. air, in figure 3.9 the overall outgoing for the 40 at% of Pu is reported. The present composition was chosen because it falls in between the available batches and could be considered neither Fe_3O_4 nor PuO_2 poor, thus both PTTs can be easily identified. As it can be seen, thermograms show a very similar behaviour overall; although it might seem that they tend to diverge in close vicinity of the PTT, this will be proved false from an accurate analysis of the liquidus and solidus points as reported in figure 3.10 and 3.11. Even if the RLS method couldn't be used for both PTs, the determination of the PTT was quite straightforward because of the good repeatability of the measures. Therefore, an average was performed on all 5 PTT detected via thermal arrest according to what indicated in figure 3.10, thus 2386 K ± 17 K was identified as the most probable PTT for the liquidus at this particular concentration in air.

For what concerns the solidus point, the thermal arrest technique was used again, this time exploiting the appearance of small undercooling shoulders in figure

3.11. As for the previous case, the various thermograms show very similar behaviours with an overall scatter of less than 10 K, thus remaining well below 1% deviation, confirming the good repeatability of measures in air. The dashed line is inserted to easily identify the solidus PTT, which has been estimated to be 1792 K ± 11 K. It is interesting to notice that this value is in very good agreement with the 20 at% Pu composition, that is to be considered the reference value for the eutectic temperature because of its Fe_3O_4 rich composition.

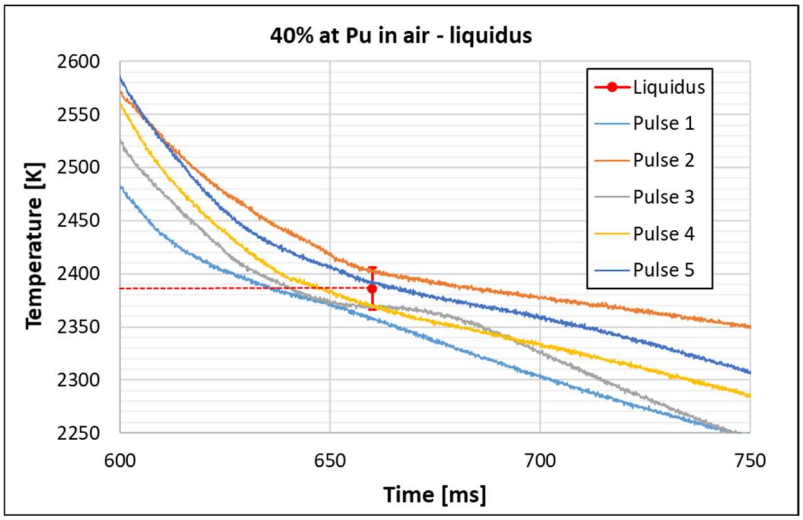

***Figure 3.10: Liquidus transition point determination by means of the thermal arrest technique for the 40 at% Pu sample in air atmosphere. The average of all pulses is taken as reference, the dotted line visually helps to determine the right value, taken as* 2386 K ± 17 K.**

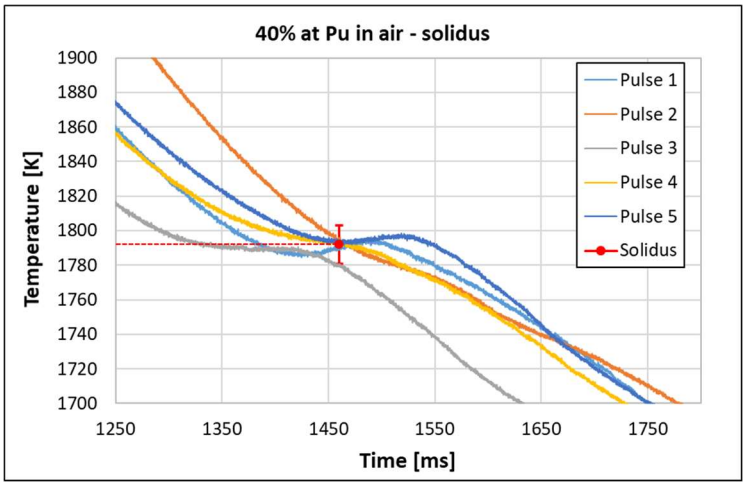

Figure 3.11: Solidus transition point determination by means of the thermal arrest technique for the 40 at% Pu sample in air atmosphere. In this case it is possible to observe a small undercooling effect that confirms the temperature registered at 1792 K ± 11 K, in good agreement with the eutectic point clearly identified at lower Pu concentrations.

3.4.2 Melting experiments in Argon atmosphere

In order to obtain a consistent comparison between the effects of the different atmospheres, in this section it will be reported the analysis of the 40 at% Pu composition experiments performed in inert atmosphere. By analysing the thermograms in the same way of the previous section, several differences can be pointed out. Although the overall shape of the graph in figure 3.12 is similar to the one in figure 3.9, it is evident that the reproducibility of every laser pulse is greatly reduced compared to the latter case. As it may be observed, the RLS technique should be employed to determine the PTT for the liquidus because of the absence of a clear plateau, resulting in a very clear and comparable signal.

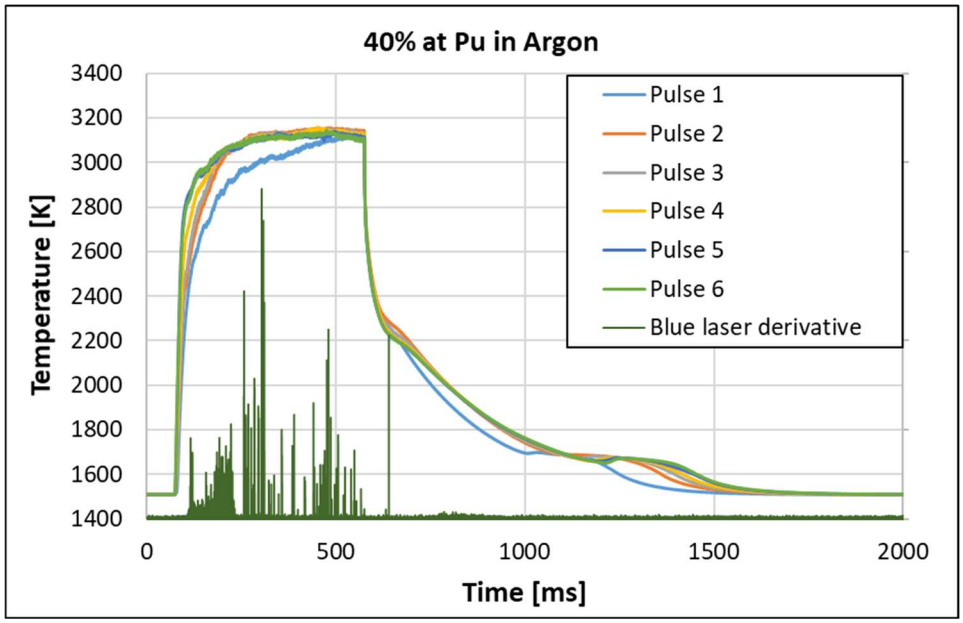

Figure 3.12: General overview of the thermograms measured for the 40 at% Pu sample in argon atmosphere.

To better understand the reduction effect, it is useful to perform a comparison between the experimental results obtained in argon for various liquidus and solidus points at different compositions. In figure 3.13 it can be observed that the PTT shift, due to the Ar atmosphere, shows a dependence on the sample composition. Actually, the more the sample is Pu rich, the more the liquidus PTT is changing pulse after pulse while the solidus remained almost unvaried; on the

other hand, the more Fe rich is the sample, the more the solidus PTT is affected by ongoing reduction, with a lower impact on the liquidus. This effect can be clearly seen comparing figure 3.13 resembling the liquidus PT for the 60 and 20 at% Pu compositions.

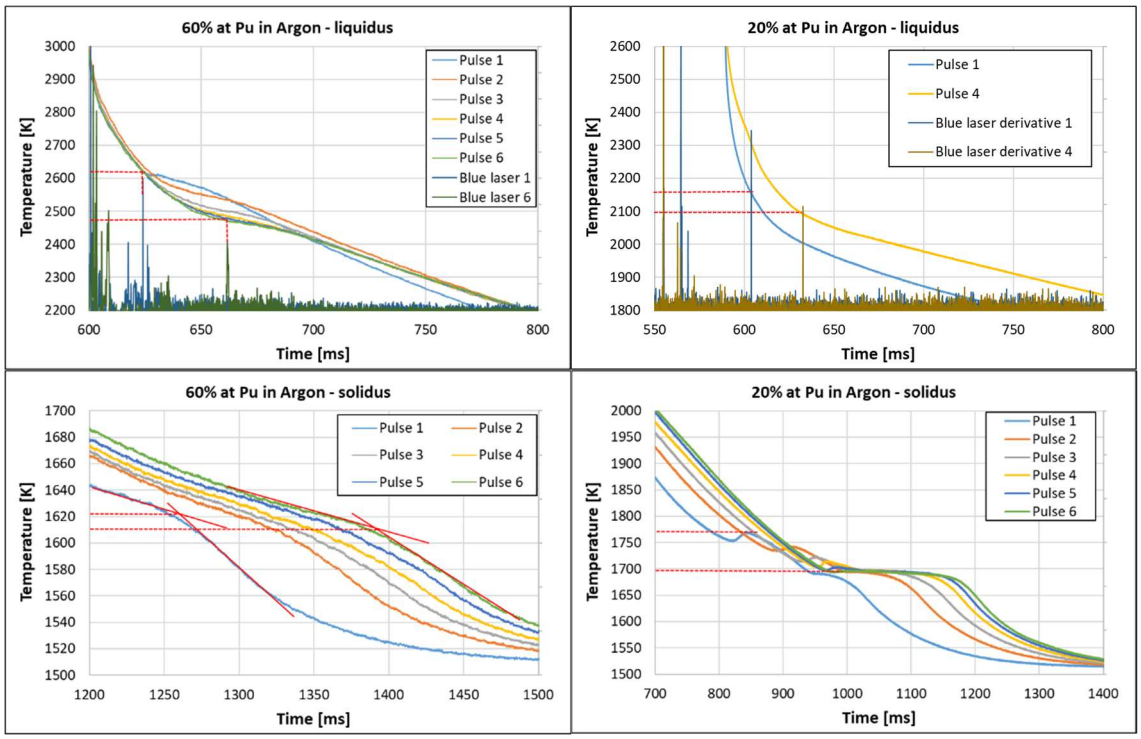

Figure 3.13: liquidus and solidus point determination for the 60 at% Pu and 20 at% Pu in Ar. The effect of the inert gas atmosphere can be observed with the visual aid of the red dashed lines, reporting the PTTs recorded for the first and the last laser pulses.

As it appears evident, the liquidus PTT for the 20 at% Pu decreases of less than 60 K in 4 pulses, for the 40 at% Pu passes from 2325 K to 2230 K ± 15 K in only 6 shots (figure 3.14), while finally the liquidus point for the 60 at% Pu lowers of 135 K, from the first to the sixth recording. Conversely, the solidus point varies of only 20 K for the 60 at% Pu, of 30 K for the 40 at% Pu and 70 K for the 20 at% Pu, showing a greater influence on iron presence in the sample. The final value recorded for the solidus point is then 1671 K ± 9 K and will be discussed later.

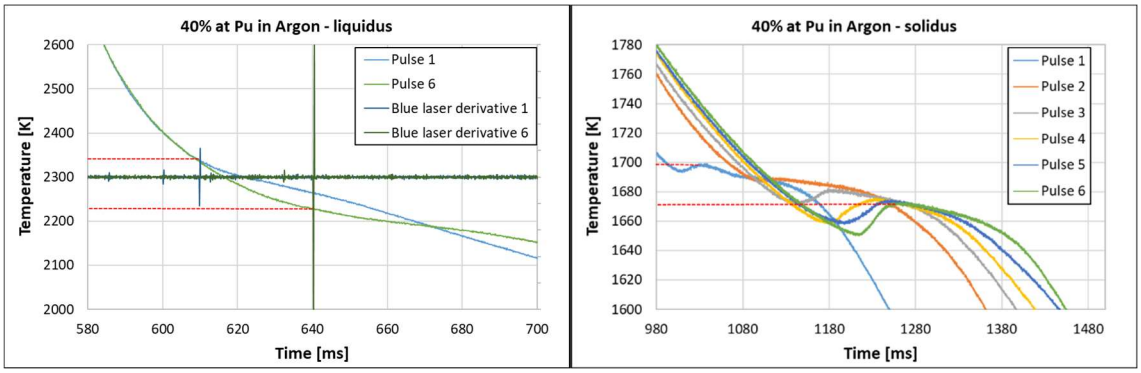

Figure 3.14: Liquidus and solidus point for the 40 at% Pu batch. The liquidus point was identified via RLS technique as 2230 K ± 15 K while the solidus point was detected with undercooling shoulders as 1671 K ± 9 K

The trial test suggests that this phenomenon is to be attributed to the ongoing reduction of the sample during measurement, that is now proven to be directly dependent on relative composition of the sample as expected [9] [7]. The 80 at% Pu showed good agreement with this trend, nonetheless, the relative thermograms are not reported in this chapter for brevity but can be found in their respective paragraphs in appendix A.

As it was explained, in figure 3.14 thermograms reports the first and the last pulses performed, both representative of the two extremes of the oxidation states of the sample during the overall measures. Now a new problem is posed, since no measure could be clearly repeated in Ar, what pulse is to be considered representative of the PT. This problem was never faced in literature and was solved with the help of the oxygen analyser that was able to deliver useful information on the reduction of the specimen. In figure 3.15 the output of the oxygen analyser i.e. the O_2 partial pressure in the gasses exiting the chamber, is plotted against time and it shows a clear peak briefly after each laser pulse. This confirms what was shown in figure 3.6, that at extremely high temperatures, even in presence of a slight overpressure, the specimen under consideration releases oxygen in the surrounding atmosphere, undergoing a chemical reduction. Furthermore, a qualitative and quantitative estimation of this phenomenon can

be performed, based on the resulting data. It is interesting to note the strictly decreasing behaviour of each maximum, with a tendency to plateau to a minimum value that is closely repeatable. Thus, since each of the peaks reported in figure 3.15 is directly proportional to the amount of O_2 released by the sample, in order to answer to the initial question, we can infer that, because of this decreasing behaviour, it is reasonable to consider the last shot performed as representative of the liquidus PT.

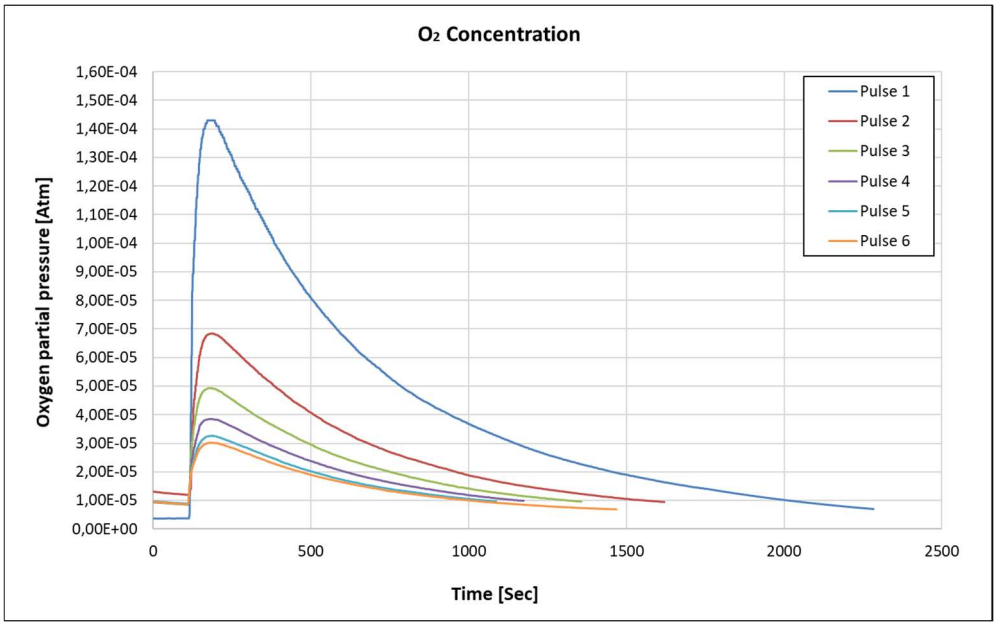

Figure 3.15: Oxygen partial pressure in the gas flow exiting the chamber, as a function of time, for 40at% Pu sample. It can be observed that a sharp peak was measured shortly after every laser pulse, revealing an O_2 release from the sample. It is interesting to note also that this release is rapidly decreasing shot by shot down to a stationary value.

Since argon and oxygen at normal pressure are still in good approximation ideal gasses, the ideal gasses law holds, so we can try to perform an estimation of the oxygen released writing:

$$PV = nRT \qquad (3.1)$$

Where P is the partial pressure of the gas (measured by the gauge in atm), V is the volume, n is the number of moles, R is the universal gas constant (in this case expressed in suitable units of measure, so R=0.0821 $\left[\frac{l \cdot atm}{mol \cdot K}\right]$)and T is the

temperature of the gas at the moment of the measurement (known to be 650°C by the manufacturer of the oxygen analyser). Thus, we can write:

$$\frac{n_{o_2}}{V} = \frac{P_{o_2}}{RT} \qquad (3.2)$$

Where n_{O2} is the number of moles of oxygen and P_{O2} is the oxygen partial pressure in the gas flow. We can also write:

$$G(t) = \frac{n(t)}{V} \cdot M_m \cdot \Gamma \cdot \frac{1}{3600} \qquad (3.3)$$

Where G(t) is the amount of oxygen released in grams as a function of time, M_m is the molar mass of O_2 and Γ is the volume flux (fixed by means of a mass flow controller to 5 l/h) and the scaling factor is for converting l/h in l/s. Substituting eq. 3.2 into 3.3:

$$G(t) = \frac{P_{o_2}(t)}{RT} \cdot M_m \cdot \Gamma \cdot \frac{1}{3600} \qquad (3.4)$$

At this point G(t) is known and we could obtain G by integrating the profile obtained from the oxygen gauge.

So:

$$G = \int_{t_0}^{t^*} G(t)\, dt \qquad (3.5)$$

represents the overall release (in grams) of oxygen during the laser pulse. The integral is performed from t_0 to t^*, that represent the beginning and the end of the peaks showed in figure 3.15. In order to have a repeatable and reasonable criterion it was decided to adopt 1E-05 atm as threshold to detect the beginning and the ending of the release. Integration of the curves was performed numerically exploiting the trapezoid method, the results are resumed in figure 3.16.

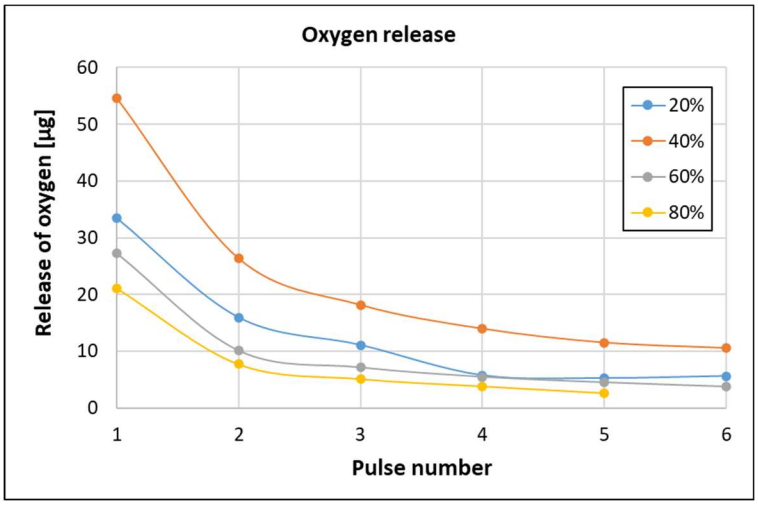

Figure 3.16: overall outgoing of the amount of oxygen released by the 40 at% Pu sample. It is evident how the reduction is decreasing after every shot with an exponential-like curve.

As it may be seen in the graph, the ongoing reduction follows an exponential-like curve, showing a saturation behaviour reaching a plateau around 10 µg of O_2 released to the environment per shot. Another interesting fact noted is that a very close repeatability of this behaviour could be observed, not only in its overall outgoing (always being closely exponential), but also on the plateau value, usually stabilising between 5 – 10 µg released per shot, regardless of the composition in consideration. This is indicating that the amount of oxygen released is mostly independent from the composition, suggesting that, although the measured effects on temperature depend on the relative abundancy, the main driver of reduction in this case may not be the species into consideration, but mostly the thermodynamic kinetics, because of the very small time scale. This interpretation is coherent with the results found experimentally, in fact, the PTT shift was more evident in the liquidus in Pu-rich samples and in the solidus in Fe-rich samples, but the overall release was almost the same, consistent with a very fast time-driven dynamic rather than chemical dependent. Continuing the analysis of the 40 at% Pu composition the PTT thermograms are reported in figure 3.14. Observing the graph, the reducing behaviour mentioned above appears evident, with the solidus temperature decreasing from pulse to pulse of

over 30 K overall. The determination of the solidus PTT was straightforward and obtained exploiting very evident undercooling shoulders that led to the identification of 1671 K ± 9 K as reference eutectic temperature. This latter value is in good agreement with both higher and lower concentration measurements (see appendix A). For the liquidus point at the present concentration, the RLS technique was exploited identifying 2230 K ± 15 K as PTT.

As last part of this paragraph a preliminary PD for the PuO_2-Fe_3O_4 system was drawn in figure 3.17, reporting the solidus and liquidus temperature for all the compositions, as listed in table 3.1.

Table 3.1: phase transition temperatures measured for the PuO_2-Fe_3O_4 system

Transition point	Sample [at%Pu]	melting in **air**		Melting in **argon**		
		PT temperature [K]	N° shots	PT temperature [K]	ΔT max [K]	N° shots
liquidus	20	2180 ± 14	3	2100 ± 14	10	4
	40	2386 ± 17	5	2230 ± 15	100	6
	60	2725 ± 22	6	2470 ± 18	135	6
	80	2884 ± 25	4	2790 ± 23	95	5
solidus	20	1790 ± 10	3	1696 ± 9	70	6
	40	1792 ± 11	5	1671 ± 9	30	6
	60	1731 ± 10	6	1610 ± 8	20	6
	80	1769 ± 10	4	1690 ± 9	10	5

Nevertheless, it is worth pointing out that the diagram reported in figure 3.17 represents more a comparison between experimental results rather than a proper PD. This is due to the fact that, since oxidation states changing were assessed, it is theoretically imprecise to assume the system as binary when a ternary approach would be more correct (although more complex), taking into consideration all the possible local composition changes, to do so, the present data should be fitted as inputs for a CALPHAD model [26] [4]. Anyway, looking at this comparison, it appears clear that the different atmosphere during the experiments resulted in a down-shift of the graph in argon, suggesting that a lower PTT is to be expected in reducing conditions for both the liquidus and the solidus.

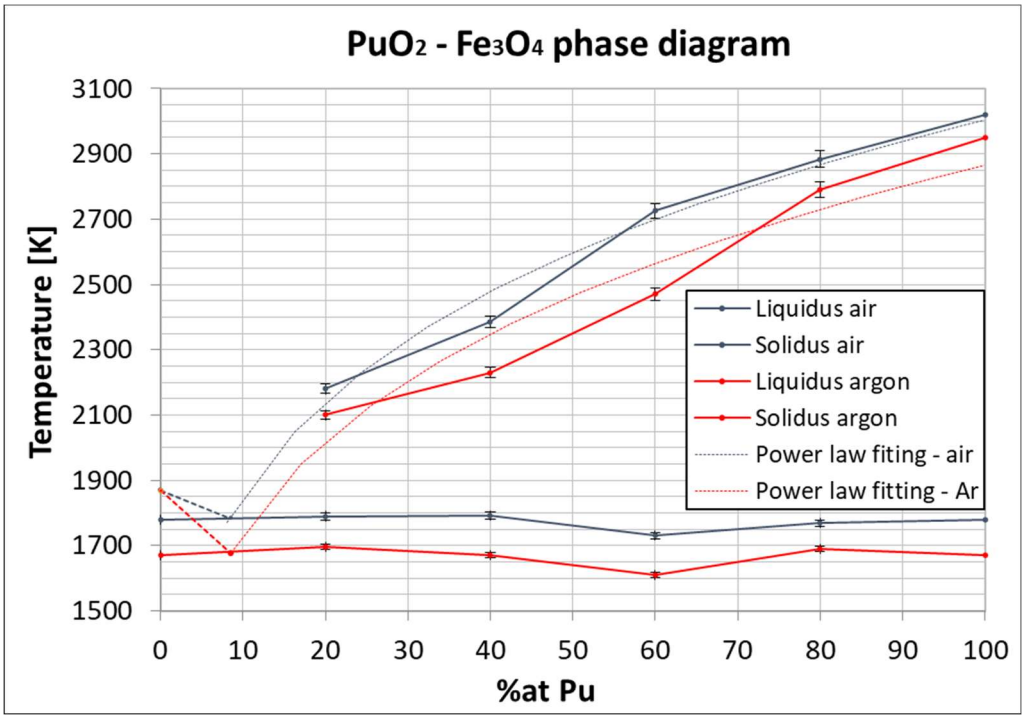

Figure 3.17: Binary PD for the PuO_2-Fe_3O_4 system. As it appears clear the different atmospheres during the experiments resulted in a down-shift of the graph, suggesting that a lower PTT is to be expected in reducing conditions. Trend lines were added in order to help identifying the probable eutectic point.

This latter information is vital during the design stage of a nuclear reactor because allows the right safety margins to be taken against cladding damage and core meltdown. Notwithstanding the relevant differences in temperatures, the overall outgoing for the two PDs is identical and is highlighted by means of empirical power law fitting lines for the liquidus points. Starting from a Pu poor composition, soon what seems to be a eutectic point is reached around 9-10 at% Pu, coherently with similar works in literature [5], then the liquidus point increases abruptly when moving towards Pu rich compositions, while the solidus point remains almost constant, further confirming the hypothesis of eutectic solidification structure. This latter hypothesis was confirmed by the SEM analysis as it will be shown in the next paragraph. Although this information may be very useful during design and accidental scenario analysis no experimental data could be obtained in that range because of time and material constrains.

3.5 After-melting sample characterisation

In order to gain a better understanding of the phenomena involved in the experiment, characterisation was performed before (as reported in the previous chapter) and after melting point assessment.

In particular, analyses were performed with the purpose of investigating both the chemical composition and the structural changings of the samples. To do so the same apparatuses discussed in section 2.2.1 were used, so both XRD and SEM analyses will be reported below.

As already mentioned before, the X-Ray Diffraction apparatus at JRC is exploiting a copper detection tube, the resolution of which was disturbed by the fluorescence effect due to the presence of iron in the samples. Nonetheless, the main goal of the XRD analysis was trying to identify the reduced phase in the samples melted in inert atmosphere, which in practice resulted unfeasible because of the reduced precision of the machine available. Another key factor that determined the impossibility of obtaining clear results regarding the chemical reduction was the relative amount of material taken into consideration. In fact, to correctly perform XRD the molten pool had to be separated from the rest of the sample and milled into powder in a mortar, introducing some random uncontrollable factors like external contamination and material loss due to manual operation. Moreover, as mentioned in the previous paragraph, the overall release of oxygen for every sample was about 20 μg, with a subsequent formation of an amount of reduced specie (of the kind Fe_xO_y) of the same order of magnitude.

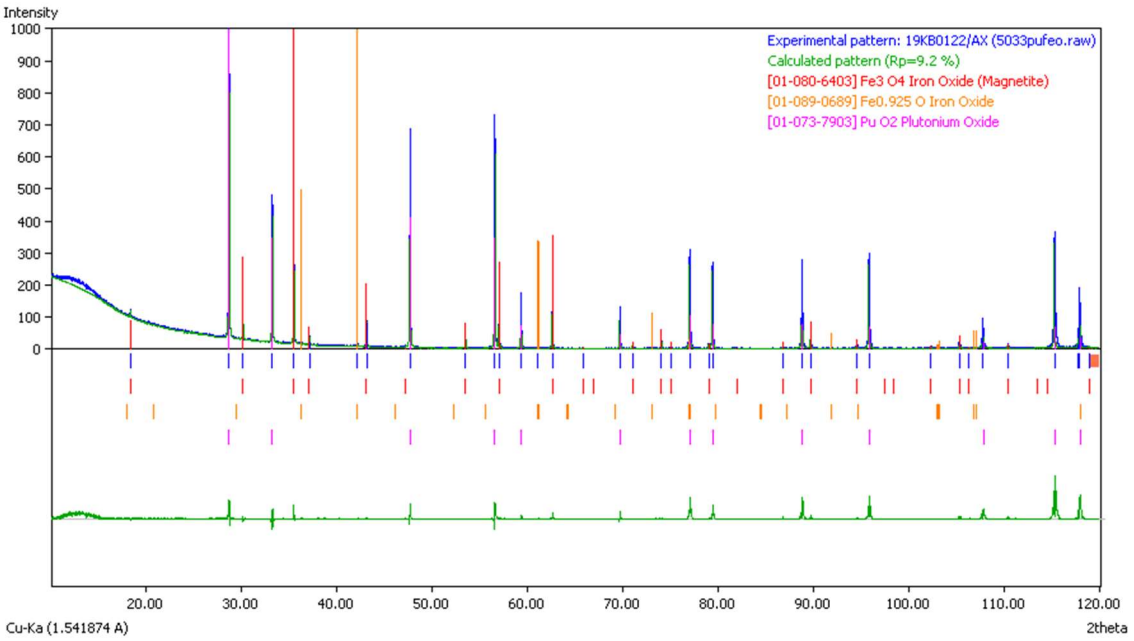

Figure 3.18: X-Ray Diffraction pattern obtained from the 40 at% Pu sample melted in inert atmosphere. No clear difference can be spotted from the spectra showed in the second chapter and this one, meaning that reduction could not be assessed by this means.

Thus, due to all these effects combined together, the reduction detected by the oxygen gauge could not be distinguished by this means. Figure 3.18 reports the pattern obtain for the 40 at% Pu sample melted in inert atmosphere. As it can be observed, the similarity with the previous one showed in chapter 2 is so stringent that nothing relevant could be assessed. Actually, the reader should not be misled by the presence of FeO peaks in the spectra, that are not representative of any reduction, as already explained in section 2.2.1. Firstly, because Fe_3O_4 is a spinel, so both oxidation states of Fe might be present in small amounts in the sample and secondly because FeO is the further reduced form of Fe_3O_4, the formation of which was detected in small amounts yet in the pre-melting characterisation, consistently with the sintering in reducing environment.

Scanning Electron Microscopy was also performed on samples after melting producing interesting results. It was decided to investigate the surface longitudinally, in order to have an overview of the structure along the cross section of the sample, so to catch how high temperatures would affect the inner

Figure 3.19: Samples after polishing embedded in a silicon matrix.

structure of a nuclear fuel pellet at various depths. Because of the brittle behaviour of the samples due to the high temperature reached and the sintering, machine cutting was excluded in order not to destroy the pellets. Splitting was then performed manually, resulting in a very uneven cross section surface. In order to allow for the analysis to be done properly, preliminary sample preparation was necessary, so to polish and flatten the surface to be scanned. Samples were then embedded in a silicon matrix by means of a special glue and polished against a fine sand brusher, obtaining a very clear and flat surface, as shown in figure 3.19.

After preparation, samples were moved to the SEM where high vacuum was made in order for the characterization to be correctly performed. Figure 3.20 and 3.21 report the pictures taken of the surface for the 40 at% Pu composition, respectively in air and in argon with a 200 times magnification.

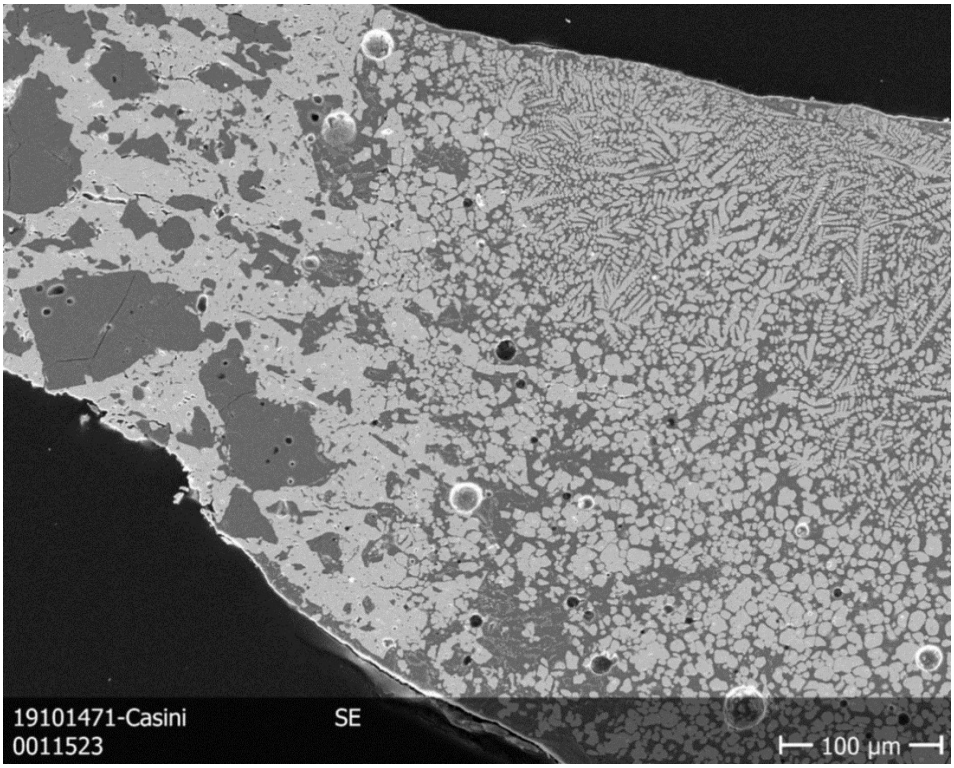

Figure 3.20: 200x SEM longitudinal picture of the 40 at% Pu sample after melting in air. The eutectic structure appears clear with very evident dendrite growth following the heat dissipation paths.

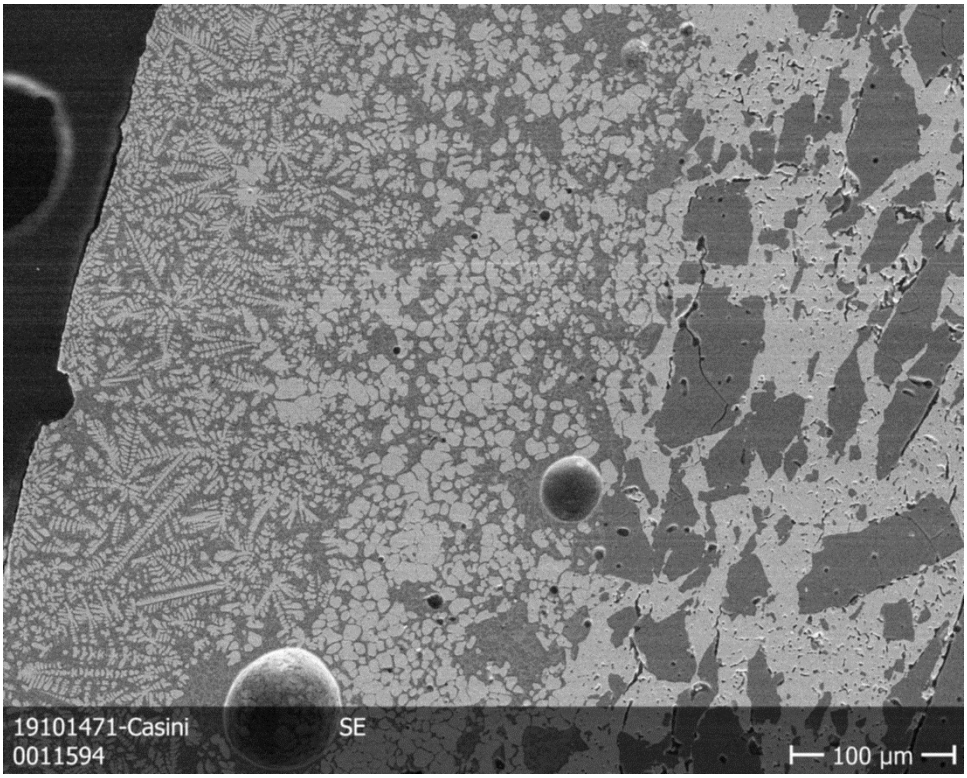

Figure 3.21: 200x SEM longitudinal picture of the 40 at% Pu sample after melting in argon. The eutectic structure appears very similar to the one obtained in the other atmosphere.

This latter composition was chosen for consistency with the data showed in the previous paragraphs. As it can be seen, no clear difference can be spotted depending on the atmosphere. The presence of dendrites is evident and is in perfect agreement with the horizontal solidus lines reported for both compositions in figure 3.17 and with similar studies [4], suggesting an eutectic behaviour. The structure is observed to be dendritic, displaying a preferential growth direction parallel to the heat flux paths from the melting centre to the non-molten region. It is also interesting to report that the melting didn't affected the whole cross section of the sample, showing a transition zone from dendritic to non-molten that seems to be granular. This latter structure was attributed to a short permanence slightly above the liquidus point in that region that allowed for partial melting but not the complete growth of the dendrites.

Another remarkable result is the evidence of temperature driven diffusion of PuO_2 in the Fe_3O_4 matrix in the close vicinity of the molten zone. This is shown in figure 3.22 where, with subsequent magnifications up to a 5000x, the plutonium dioxide diffusion at grain boundaries in the iron oxide lattice is highlighted. Notably, the diffusion structure is lamellar, and observable only in the close vicinity of the melting transition zone, similarly to what observed for the U – Zr - Fe – O system [4]. For completeness EDS was performed in the concerned area to confirm the presence of Pu in the iron matrix.

Table 3.2: EDS scan of the lamellar structure reported in figure 3.22.

Elem.	Line	Int.	W%	A%
O	Ka	17.8	8.41	47.16
Fe	Ka	108.7	15.46	24.84
Pu	Ma	478.3	76.14	28.00
			100.00	100.00

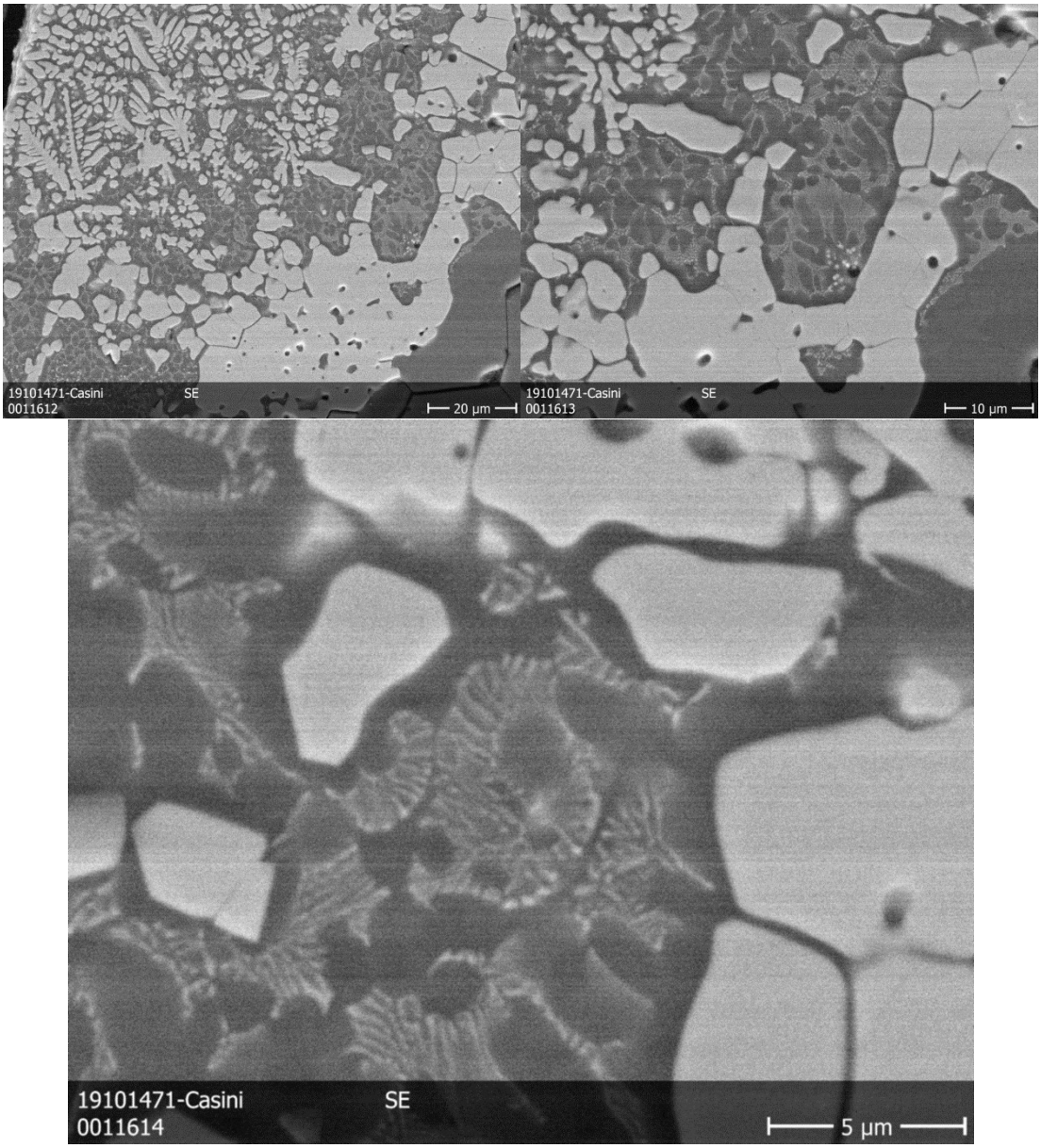

Figure 3.22: Increasing magnification of PuO_2 lamellae inside iron oxide (white stripes on the black matrix).

Unfortunately, due to the high oxygen content of the sample, the measurement reports very imprecise values. The reason behind this is that the result of the EDS technique is strongly dependent on the weight percentage of each element, thus, being Oxygen a light element (compared to Fe or Pu), smaller ionisation effects are produced by the same electronic beam, reducing the overall counts and the subsequent detection. This is a very well-known problem in literature [29], in order to obtain good resolution on light elements (such as oxygen or carbonium)

a more precise photodetector should be used than the one available at JRC Karlsruhe or a completely different coating material [30].

Nevertheless, a more sensitive photodetector would suffer of saturation because of the intense counts produced by heavier species present in the sample, making a trade-off necessary. Furthermore, because of the very unique applications involving the JRC, the photodetector was set in order to have good resolution on heavy elements (i.e. transuranium elements), obtaining information on the oxidation state by different means. For this reason, the EDS analysis reported above need to be considered only on a qualitative basis, only confirming the presence of PuO_2 in the iron matrix in the form of lamellae. Further works could take advantage of TEM analysis to confirm the presence of eutectic structure.

Concluding remarks. The experimental results of this work were discussed in the above paragraphs. At first the emissivity assessment of both pure Fe_3O_4 and the PuO_2 – Fe_3O_4 system, at various relative concentrations, was shown, explaining in detail the properties and the underlying hypothesis of the present case. Then, the effect of atmosphere gas in melting point measurement was explained, showing the results of an interesting trial and the relative conclusions, together with the introduction to the oxygen analysis in the ambient gasses. Subsequently, exploiting the information on the previous paragraphs, a complete overview of the recorded data is reported, resulting in the preliminary PD estimation for the system in consideration. Moreover, for the first time, the atmosphere gas was taken into consideration, offering the opportunity to clearly identify the role of the environment in melting point, resulting in the downshift of the PD obtained in inert atmosphere. At the end of the chapter a summary of the characterisation tests performed on the samples is shown, illustrating the eutectic structure and highlighting the intergranular diffusion of plutonium dioxide in the form of lamellae.

4. Conclusions

The present work has led to important steps forward both for the employed experimental laser heating setup and for the Pu-Fe-O system assessment.

From an instrumental viewpoint, a long-time existing laser heating technique [6] [25] was improved with the successful implementation of a zirconia-probe based oxygen analysis. This permitted a reliable estimation of the oxygen released from the sample during the laser-heating experiments, leading to a more complete understanding of the interaction between fuel and cladding in different atmospheres. In particular, the effect of atmosphere on the melting behaviour of several mixed Pu-Fe-O compositions was proven experimentally, evidencing a clear role of Pu concentration on the reduction/oxidation behaviour of the sample. A comprehensive summary of all the data collected is reported in figure 3.17 and table 3.1, which represents the isopleth plane determined for the PuO_2 – Fe_3O_4 system.

Emission of oxygen by the sample was detected after each pulse in inert atmosphere, monotonically decreasing down to a stationary repeatable value of about 5 μg per cycle. Correspondingly, the measured solidification temperature decreased until it stabilised at a repeatable value, reported in Table 3.1 and Figure 3.17.

Measured PTTs were more repeatable from the very first shots for samples melted in air. This shows that the presence of extra oxygen in the atmosphere has a stabilising effect of the high-temperature chemistry of the current compounds. As already largely addressed in previous literature [9] [7], this is certainly due to the high oxygen potential of plutonium dioxide, which easily tends to be reduced to PuO_{2-x} at high temperature, unless oxygen losses are compensated for in the atmosphere.

The final values recorded for the solidus PTTs showed to be within 5% in the whole range, varying from 1610 K to 1696 K in Ar and from 1731 K to 1792 K in air. This observation suggests that eutectic phases are most probably formed after solidification, as observed in similar works [9] [5] [4]. The presence of eutectic phases are further suggested by SEM analysis, which revealed solidification structures typical of eutectics, such as dendrites and lamellae of plutonium oxide. On the other hand, the nearly constant solidus temperatures observed for all Pu-Fe-O mixed compositions in the present investigation systematically differ by more than 100 K depending on the experimental atmosphere. This suggests that two eutectics may exist in the ternary Pu-Fe-O system: the first richer in oxygen with a eutectic temperature around 1760 K, the second with a more reduced composition and a eutectic temperature closer to 1670 K.

In both cases of oxidising or inert/reducing atmosphere, it was observed that mixing iron oxide to plutonium dioxide results in a melting point decrease for both species, as suggested from figure 3.17, with a foreseen eutectic point around 8at % – 10 at % Pu.

In general, lower PTTs were systematically observed in reducing conditions for both liquidus and the solidus/eutectic. This information is vital for the definition of the core safety margins during the design stage of a nuclear reactor.

The set of results collected here constitute, in the authors' knowledge, the first experimental data ever reported for Pu-containing mixed compositions in the Pu – Fe – O system. They certainly pave the way to a sounder understanding of the high-temperature behaviour of fundamental material systems for the safety assessment of fast-neutron nuclear reactors.

Future work will imply a precise CALPHAD determination of phase boundaries in the ternary Pu – Fe – O, whereby the experimental data presented here can serve as validation benchmark.

APPENDIX A – Complete results discussion

Abstract. For completeness in the present section all the experimental results obtained in the frame of this thesis work are reported. Nonetheless, for the sake of brevity, it will be assumed that the reader already went through section 3.4, thus only a brief interpretation will be given for each composition following always the same scheme (i.e. air atmosphere, argon atmosphere, oxygen release analysis).

A.1.1 20 at% Pu - air

Proceeding with order, the 20 at% Pu composition will be the first to be reported, with the overall outgoing shown in figure A.1. As already seen in the previous chapters the results in air show very good repeatability, with almost overlapping thermograms.

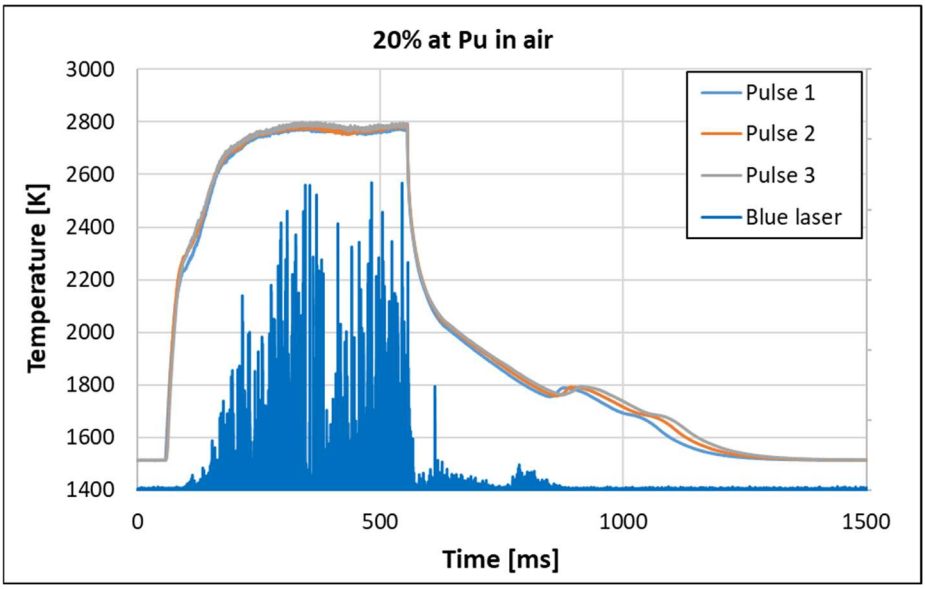

Figure A.1: Overall outgoing for the 20 at% Pu concentration in air. The results are perfectly matching with almost overlapping thermograms.

In the present case the RLS technique could be deployed to easily determine the PTT for the liquidus point as shown in figure A.2. Unfortunately, during the solidus PT the recorded signal faded, nonetheless the determination of the PTT

was quite straightforward because of the very evident undercooling shoulders, as shown in figure A.3. Thus, the recorded PTT are 2180 K ± 14 K for the liquidus point and 1790 K ± 11 K for the solidus point. As already mentioned, this latter value will be taken as reference for the eutectic temperature in the present composition, for this measure is the clearest obtained among all.

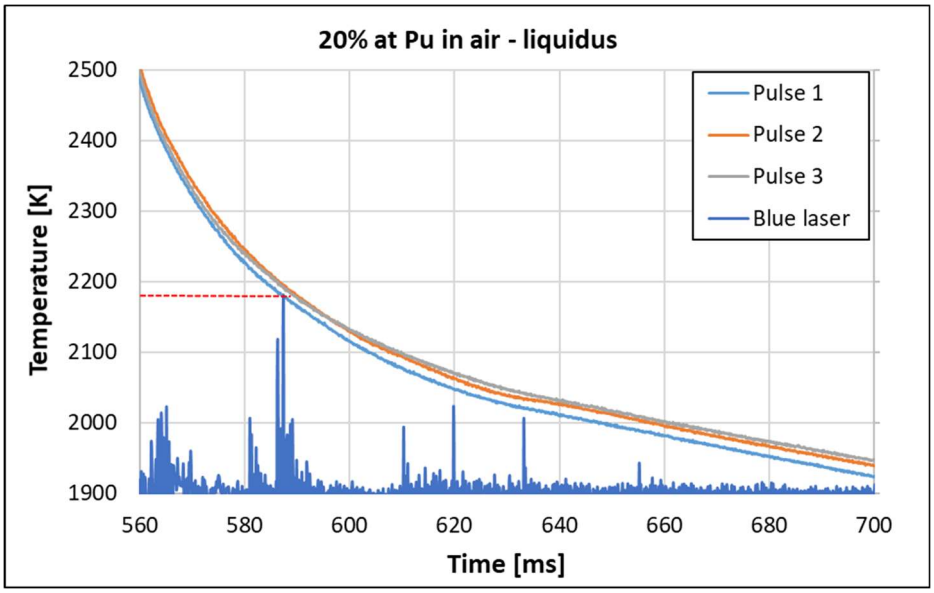

***Figure A.2: Liquidus PT point for the 20 at% Pu in air. In the present case the RLS technique could be deployed to determine the exact PTT of* 2180 K ± 14 K.**

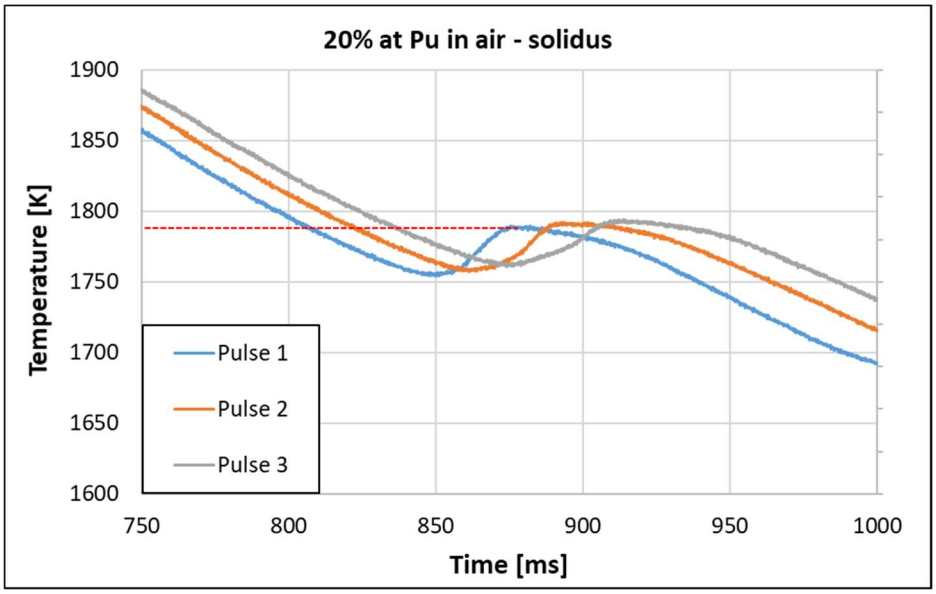

***Figure A.3: Solidus PT point for the 20 at% Pu composition in air. In this case the PTT was determined via the evident undercooling shoulders as 1790* K ± 11 K.**

A.1.2 20 at% Pu – argon

For the 20 at% Pu composition the recordings obtained in inert atmosphere are reported in figure A.4, where the overall trend can be observed, together with a reference plot of the blue laser signal. The difference with the previous composition can already be spotted by eye, with the present thermograms hardly matching each other, pulse after pulse. The following figures A.5 and A.6 report the liquidus and solidus PT respectively. The liquidus point was determined via RLS technique with the consideration already described in paragraph 2.4 on the reduction state of the specimen, so the PTT is considered to be 2100 K ± 14 K. The solidus point instead shows very evident reduction shoulders, with the PTT determined via thermal arrest around 1696 K ± 9 K. As for the oxidising atmosphere, this temperature will be taken as reference for the eutectic point for the present atmosphere since this measure is the clearest and affected by the lowest uncertainty.

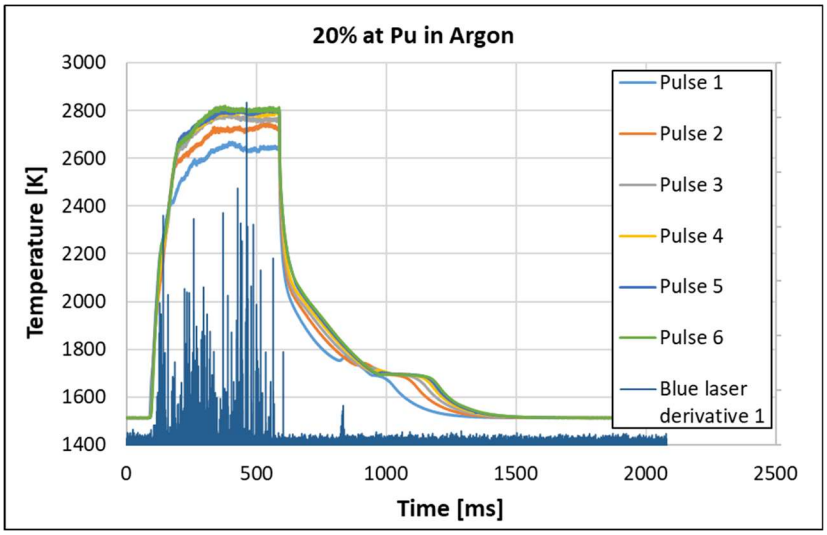

Figure A.4: Overall outgoing of the thermograms for the 20 at% Pu in inert atmosphere. The reducing behaviour can easily be spotted by eye on the solidus PT.

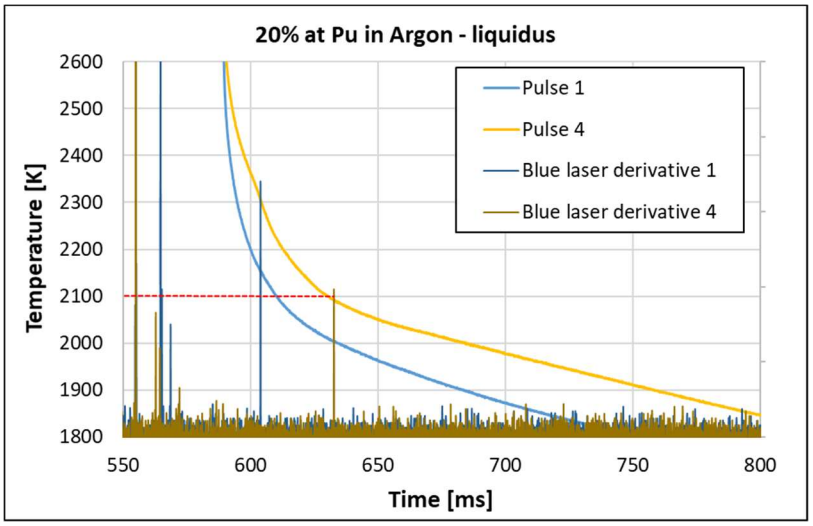

***Figure A.5: Liquidus PT for the 20 at% Pu. The PTT is obtained through the RLS technique and taken as 2100 K* ± 14 K.**

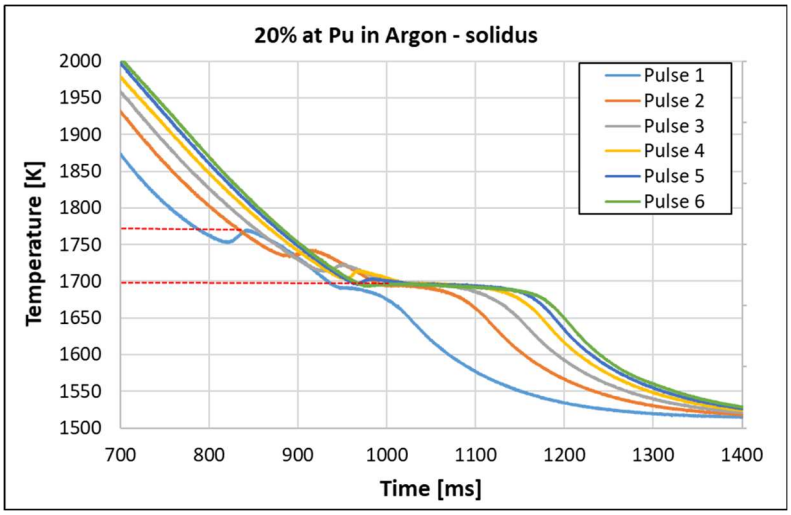

***Figure A.6: Solidus PT for the 20 at% Pu composition. The PTT was obtained trough the very evident thermal arrest of the last laser pulse and is considered to be 1696 K* ± 9 K.**

A.1.3 20 at% Pu – oxygen release analysis

In the present paragraph the analysis of the data coming from the Gen'Air oxygen analyser will be presented, the results are reported in figure A.7 and A.8. As it can be seen, the overall trend is coherent with the description given in section 3.4, clearly identifying an oxygen release during each shot in reducing environment. Not only this was confirmed, but also the release outgoing is following the same pseudo exponential behaviour, strictly decreasing shot after shot down to a stationary value around 5 μg.

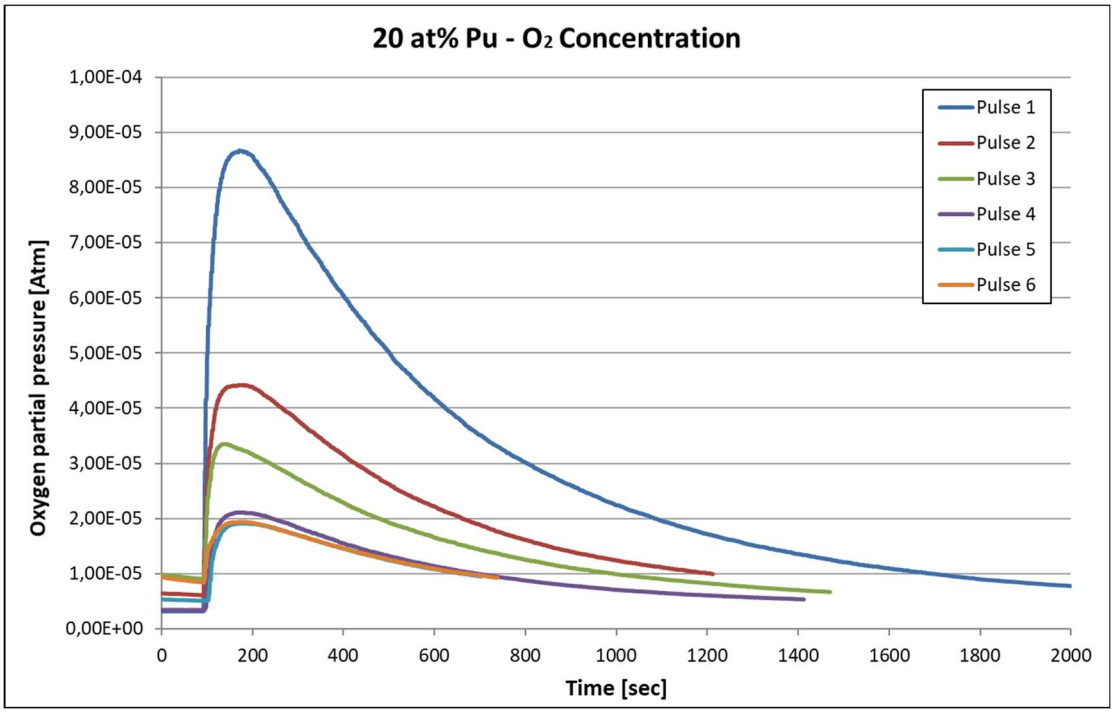

Figure A.7: Oxygen partial pressure in the gas flow exiting the experimental vessel after each laser pulse. As it can be seen a release of oxygen was detected, following a strictly decreasing behaviour pulse after pulse.

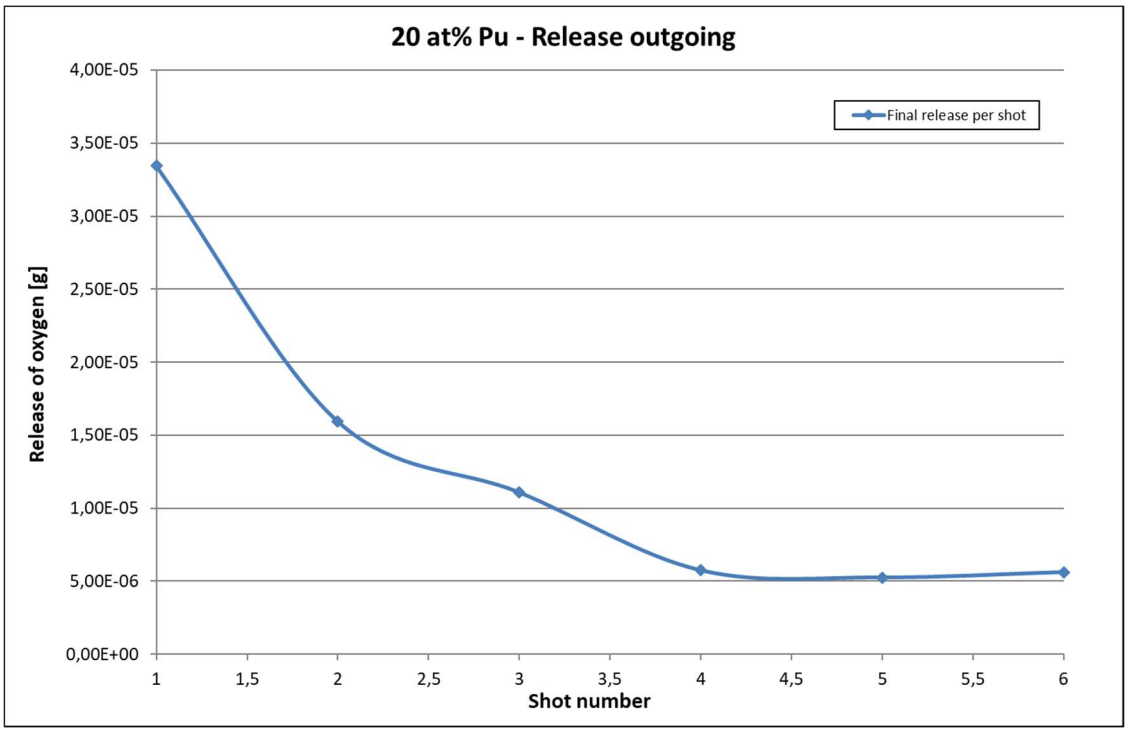

Figure A.86: Release outgoing of oxygen compared to the pulse number. Coherently with the previous figure, the overall release of oxygen is decreasing after every pulse, justifying the impossibility to repeat any measure before the stationary value is reached.

A.2.1 60 at% Pu – air

Since the 40 at% Pu was already fully described in paragraph 3.4 we can move directly to the 60 at% Pu composition. The overall outgoing is shown in figure A.9.

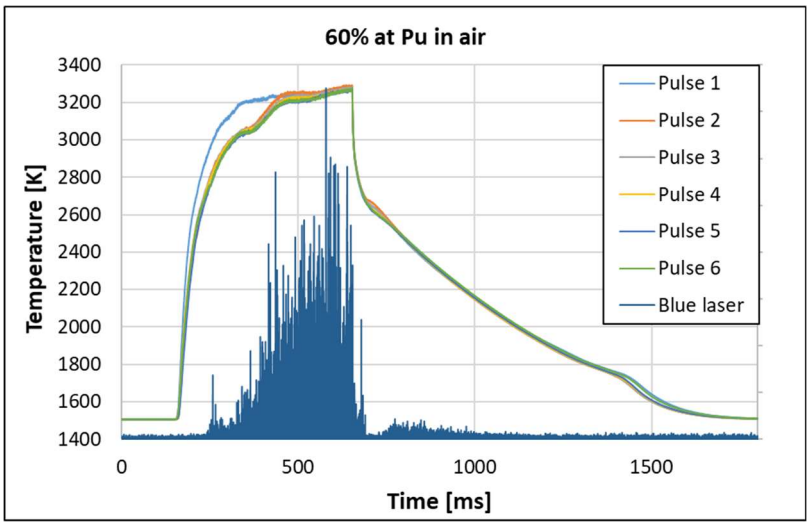

Figure A.9: Overall outgoing of the temperature profiles for the 60 at% Pu composition in air.

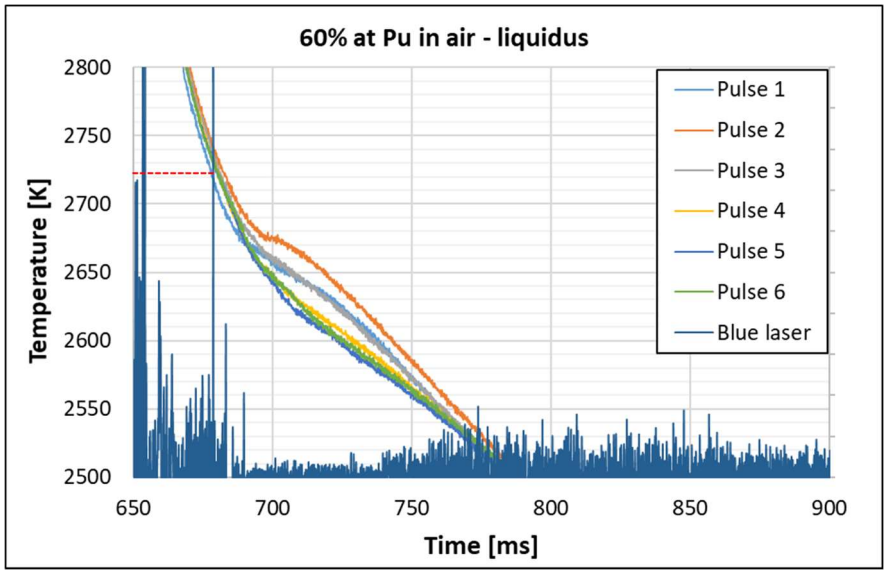

***Figure A.10: Liquidus point PT for the 60 at% Pu composition in air. The PTT was determined easily by exploiting the RLS technique. As it might be noticed, there is a sudden spike in correspondence of 2725 K* ± 22 K, considered the liquidus temperature.**

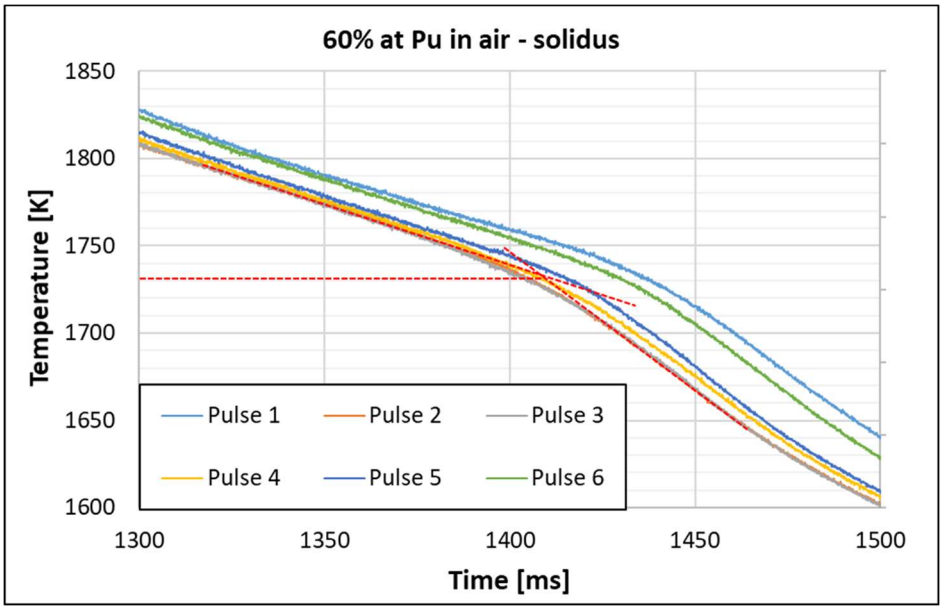

***Figure A.11: Solidus point PT for the 60 at% Pu composition in air. The PTT was very hard to detect because of the small presence of iron oxide in the sample, nevertheless, exploiting slope changes 1731 K* ± 10 K was identified as the solidus temperature.**

Once again, the repeatability of the experiment in air is well confirmed by the measured data. Figures A.10 and A.11 report the liquidus and solidus PTs respectively. The liquidus point was determined via RLS technique, identifying 2725 K ± 22 K as the most probable PTT, confirmed by multiple measures with very low scatter. The solidus PT was much harder to identify because of the very reduced amount of iron oxide in the sample. Nonetheless the slope change presented in the thermogram was exploited with straight lines in order to identify the curvature center identified to be around 1731 K ± 10 K. Obviously, this method delivers only approximate results, and although the registered value is considerably lower than the reference one, the scatter is below than 5%, and data show good consistency and repeatability.

A.2.2 60 at% Pu – argon

For the 60 at% Pu composition in inert atmosphere the overall outgoing is reported in figure A.12

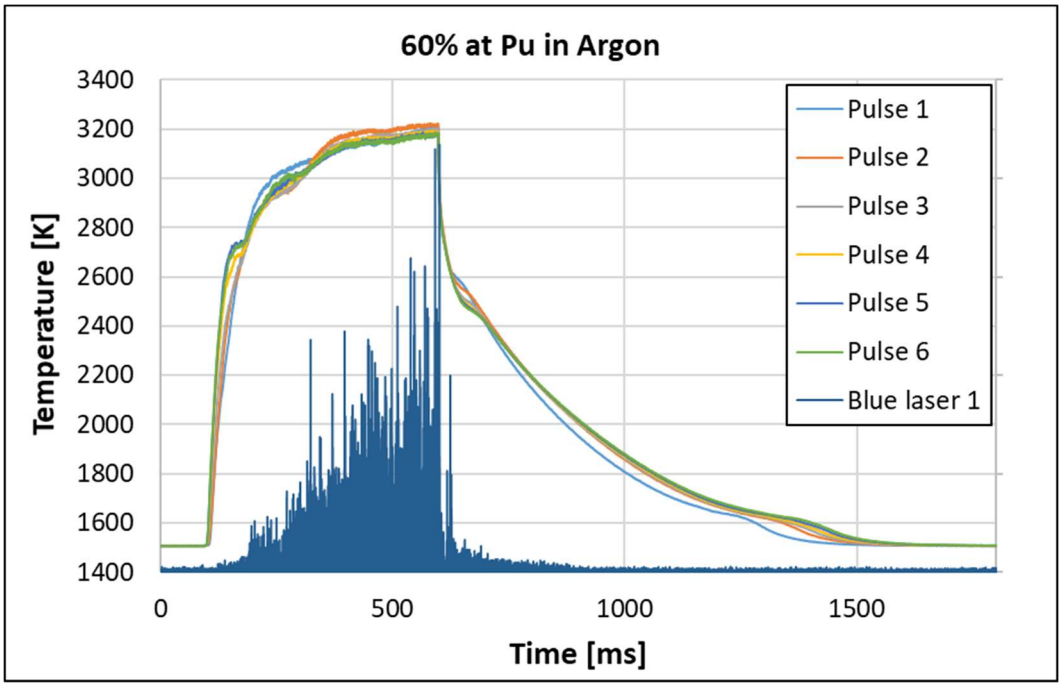

Figure A.12: Overall outgoing for the 60 at% Pu measurements in inter atmosphere. As it can be seen the influence of the reducing effect is more evident on the liquidus point rather than solidus.

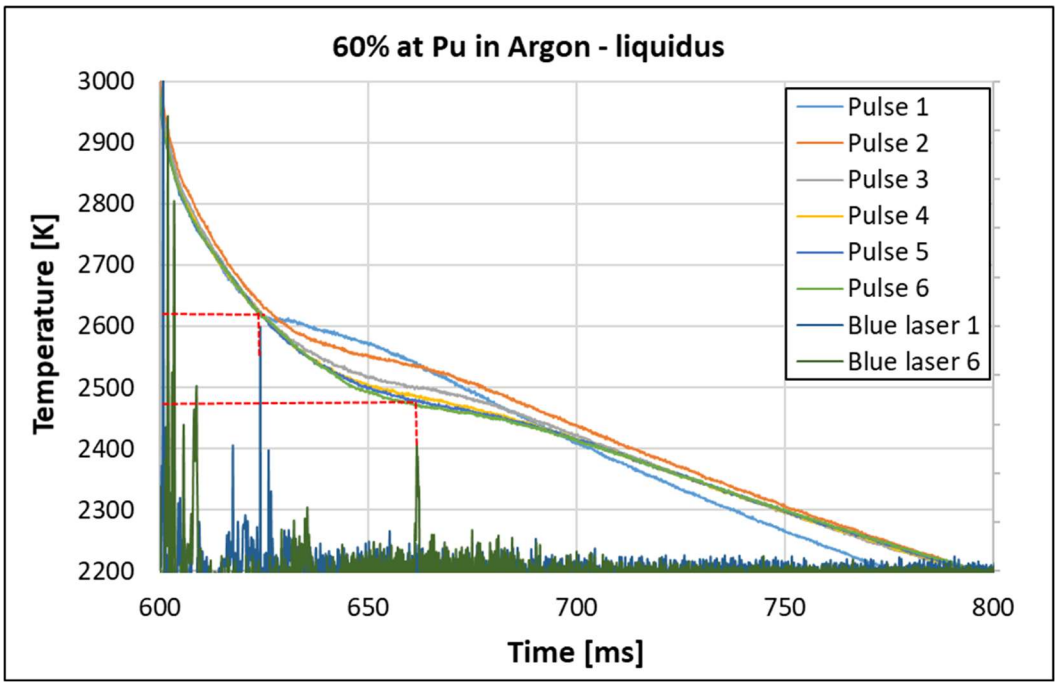

***Figure A.13: Liquidus point for the 60 at% Pu composition in argon. As it appears evident, the influence of the oxygen release is becoming more and more relevant on this PT. In the present figure the RLS technique was deployed to clearly identify this effect and the relative PTT as* 2470 K ± 18 K.**

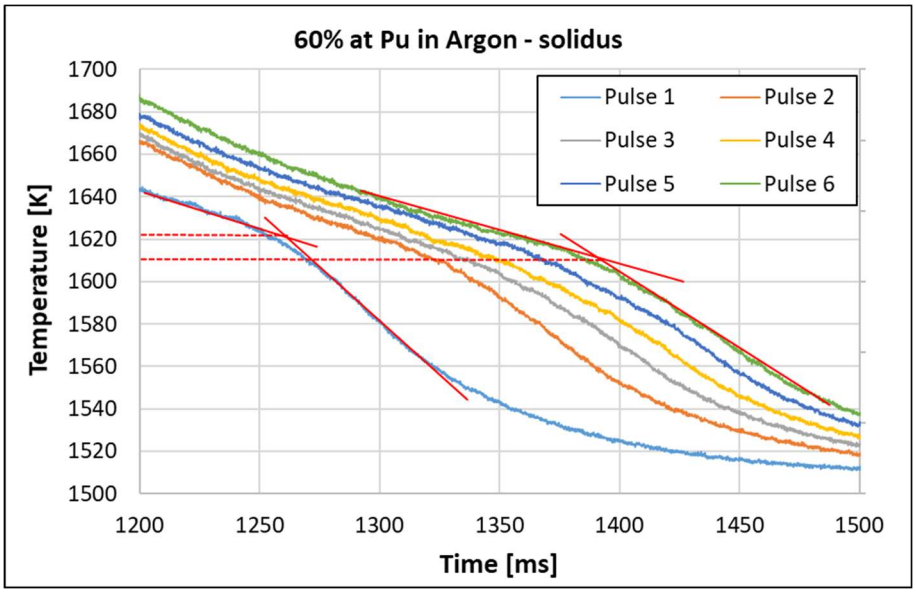

Figure A.14: Solidus PT for the 60 at% Pu in argon. The PTT was determined via slope change, exploiting straight lines to identify the curvature center. The reference temperature in this case was taken as 1610 K ± 8 K. In this picture the fading effect of the sample reduction is highlighted by the relatively low scatter of the identified points.

As it can be seen, the effect of the environment is moving from the solidus PT to the liquidus PT, inducing more evident effects on the latter, while almost disappearing from the former, compared with the previous compositions. The two points are shown in figures A.13 and A.14 respectively. For the upper PT the RLS technique was used very efficiently to identify the PTT as 2470 K ± 18 K. The thermograms also highlight the increased effect of downshift of the repeatable value of PTT.

For the solidus point instead, the slope change analysis was performed with the visual aid of straight lines to identify the curvature center. These points proved to be relatively close to each other, although still following a decreasing behaviour as in the previous compositions. The identified value is 1610 K ± 8 K, which is in good agreement with the foreseen eutectic point in Ar atmosphere.

A.2.3 60 at% Pu – Oxygen analysis

To complete the analysis on this composition, data relative to the oxygen released during the experiments in argon are reported in figures A.15 and A.16.

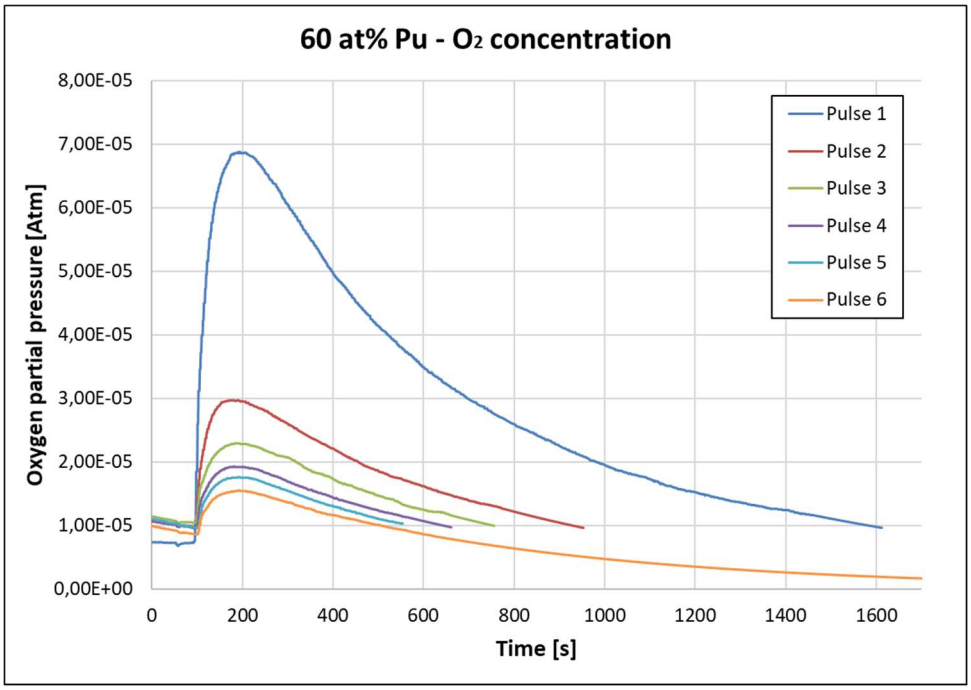

Figure A.157: Overall profile of the oxygen partial pressure during the 60 at% Pu sample melting in argon.

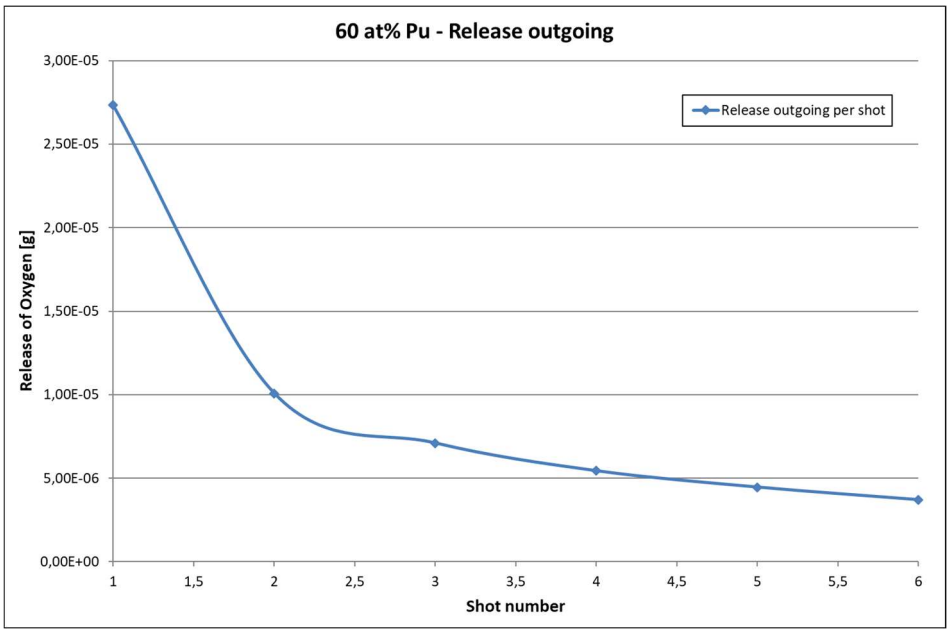

Figure A.16: General outgoing of the oxygen released by each of the laser pulses performed during the experiment.

The inert atmosphere induces a reduction in the sample that therefore releases oxygen in the surrounding environment. The kinetics of the released was already described in section 3.4 and is identical to the one shown in the previous pictures. A sharp peak in the oxygen partial pressure could be detected following each melting experiment, the trend of these released appears to be strictly decreasing with a pseudo-exponential behaviour down to a stationary value, that showed to be repeatable.

A.3.1 80 at% Pu – air

The last composition to be analysed is the 80 at% Pu, the results of the measurements performed in air are reported in figures A.17 to A.20. As shown, the undercooling shoulder due to the liquidus PT became very evident while the solidus point resulted to be undetectable; for this reason, a new experiment was performed heating the sample to a temperature lower than the liquidus to highlight the lower PT, as shown in figures A.19 and A.20.

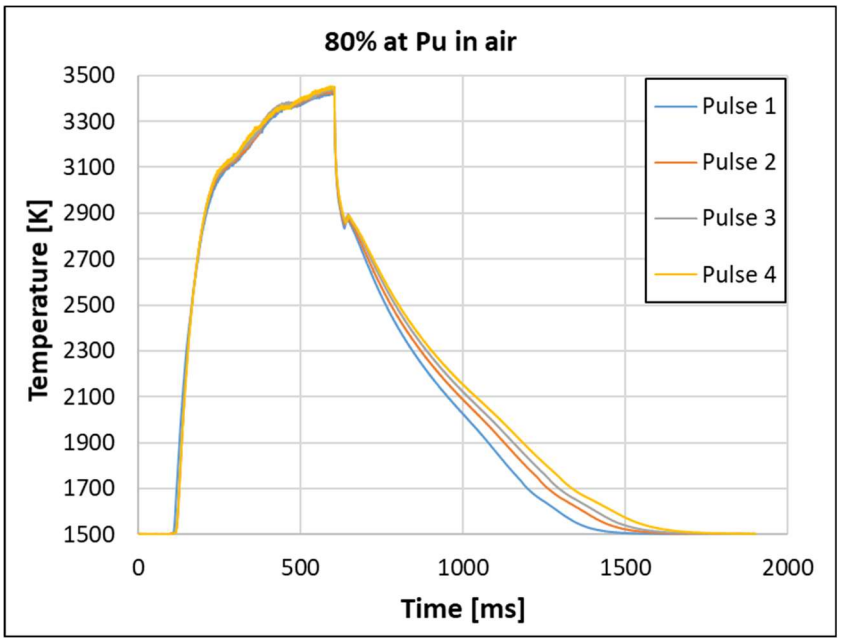

Figure A.17: Overall outgoing for the 80 at% Pu composition in air. No clear inflection due to the solidus point can be observed.

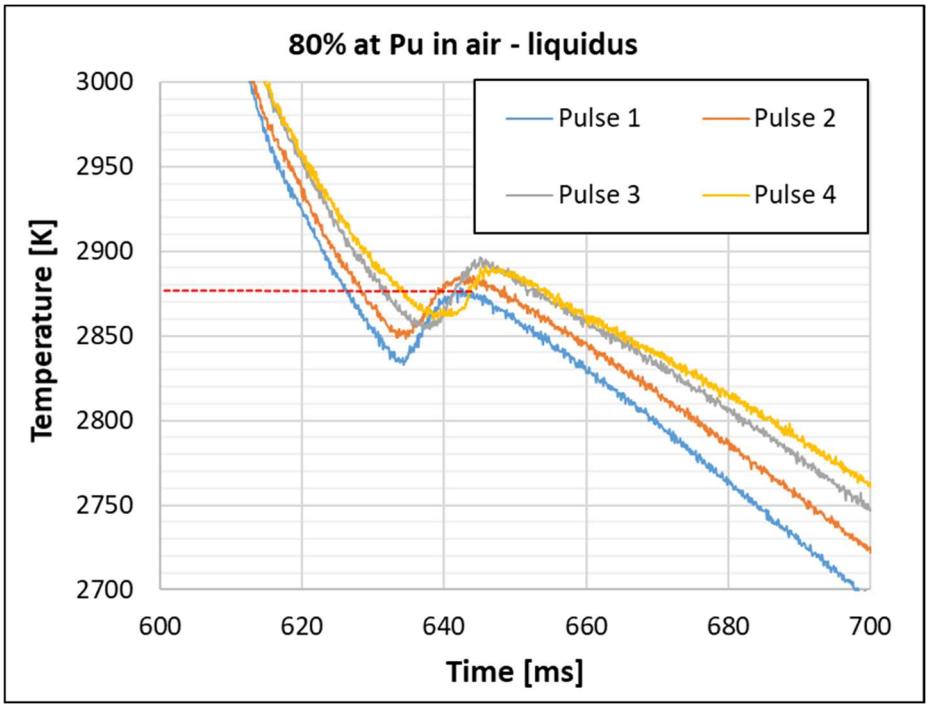

***Figure A.18: Liquidus PT for the 80 at% Pu in air. As for the other experiment the thermograms appear very close to each other, with a very low random scatter around the registered value of 2884 K* ± 25 K.**

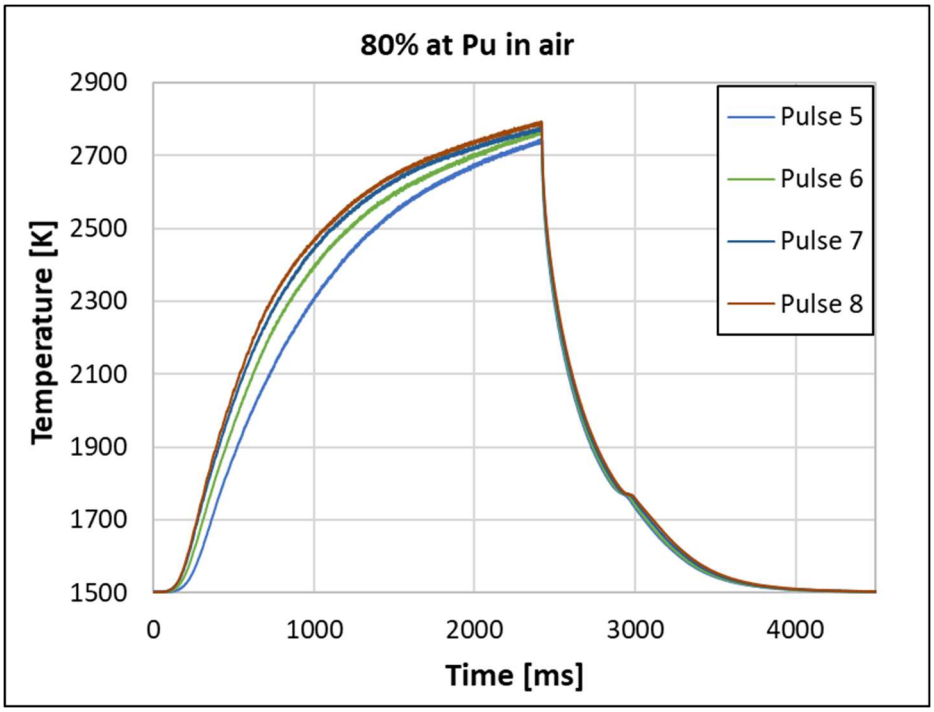

Figure A.198: Overall profile of the temperature in the experimental trial performed to highlight the solidus PT. As it can be seen, the temperature was kept below the liquidus point but higher than the expected eutectic for a longer time, thus inducing melting in a portion of material sufficient for detection.

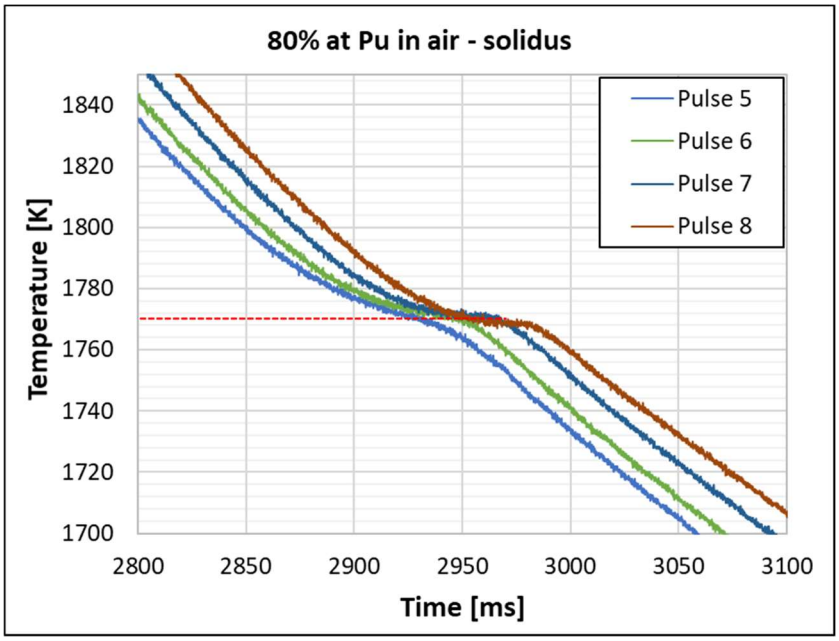

Figure A.209: Solidus point for the 80 at% Pu composition in air obtained with the modified laser pulse. The PTT recorded is 1769 K ± 10 K, which is in very good agreement with the reference value.

The liquids point reported in figure A.18 is highlighted by very evident undercooling shoulders, that led to the identification of 2884 K ± 25 K as most probable PTT. As already mentioned, the solidus point resulted impossible to determine from the initial thermograms reported in figure A.17, due to the very reduced amount of iron oxide in the sample. To compensate for this, other pulses were performed modifying the amount of energy delivered by the laser in order to keep the temperature profile as long as possible below the detected liquidus PTT but as higher as achievable of the expected eutectic point. This technique induced very clear thermal arrests in the temperature profiles allows the identification of the PTT at 1769 K ± 10 K, which is in excellent agreement with the expected value, further confirming the reliability of the reference temperature for the eutectic point. Notwithstanding the different experimental procedures, the data obtained with this method present all the features of the previous compositions in air, with very low relative scatter and excellent repeatability.

A.3.2 80 at% Pu – argon

The results of the 80 at% Pu composition in inert atmosphere are reported in figures A.21 and A.22. The reducing effect of the inert atmosphere appears very evident in the liquidus PT, with strictly decreasing undercooling shoulders highlighting the PTT of 2790 K ± 23 K, almost 100 K lower than the analogous in air. As for the previous case, the solidus point could not be detected clearly during the regular laser pulses, unfortunately the same technique exploited in the previous paragraph was unavailable because of the mechanical failure of the specimen during the test. Notwithstanding this, all the other results are in perfect agreement with the expected trend for the present composition, and the SEM characterisation suggests the presence of the foreseen eutectic point as well, thus it is reasonable to assume that the solidus PTT is around the reference value of 1690 K ± 9 K.

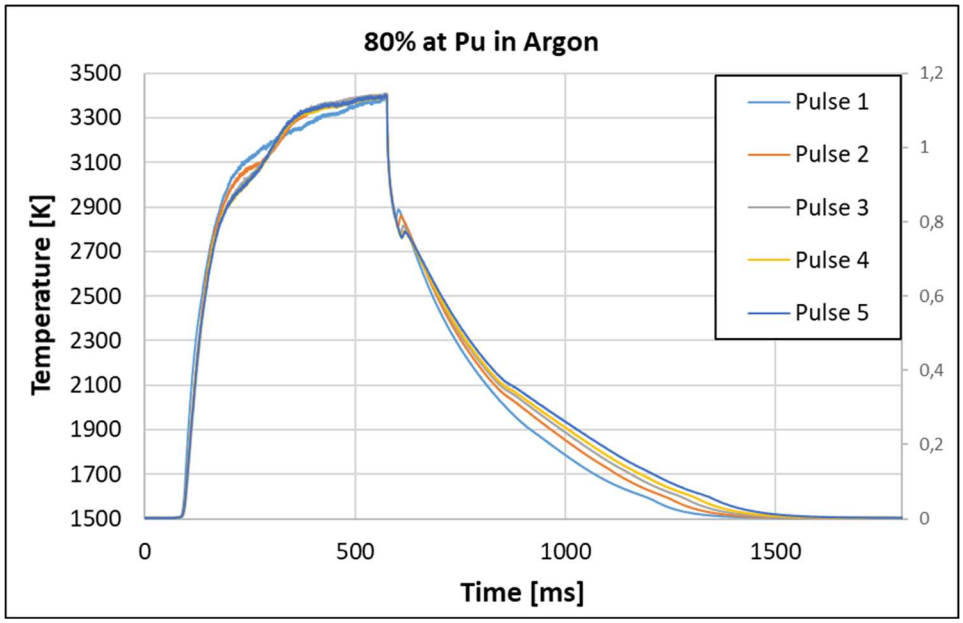

Figure A.21: Overall outgoing for the 80 at% Pu composition in argon. As it was expected, the liquidus point became very evident, showing clear reducing effects, while the solidus point resulted practically undetectable.

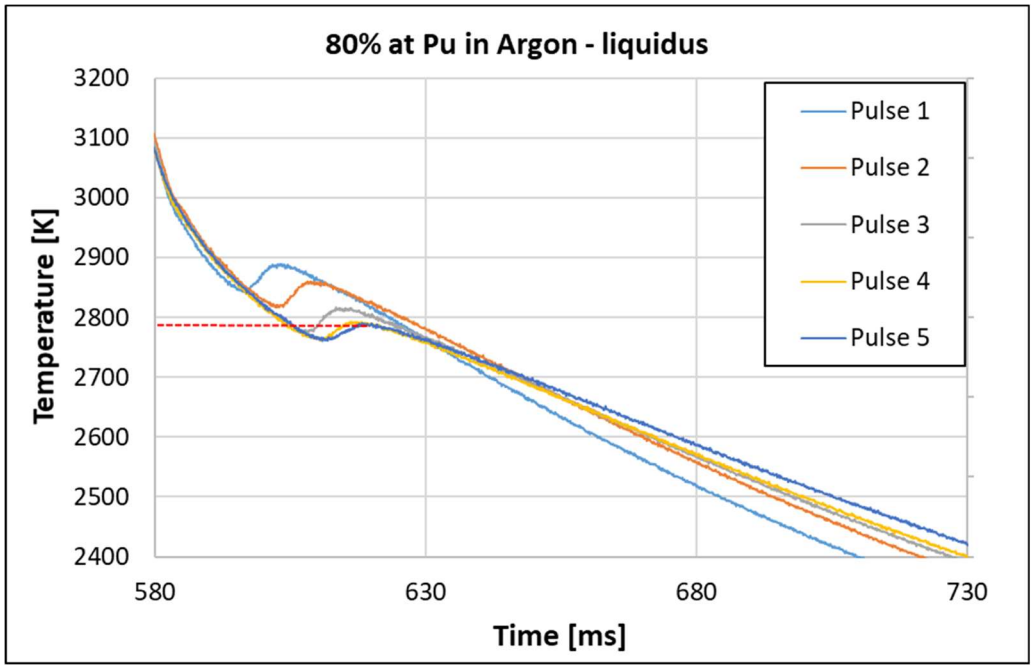

Figure A.2210: Liquidus point for the 80 at% Pu in argon. The PTT was determined to be 2790 K ± 23 K via very evident undercooling shoulders, since the RLS technique was unavailable due to the considerable amount of liquid material distorting the reflected light.

A.3.3 80 at% Pu – oxygen analysis

The concluding part of this appendix will be the analysis of the data coming from the Gen'Air, relative to the oxygen released by the sample in inert atmosphere. The recorded values are reported in figure A.23 and A.24, and as expected are perfectly matching the values of other compositions. Each laser pulse was followed by a release of oxygen, inducing a peak in its partial pressure in the exiting gasses, detected by the device with a fixed delay. This release was following a strictly decreasing behaviour until the stationary value of 5 μg was reached.

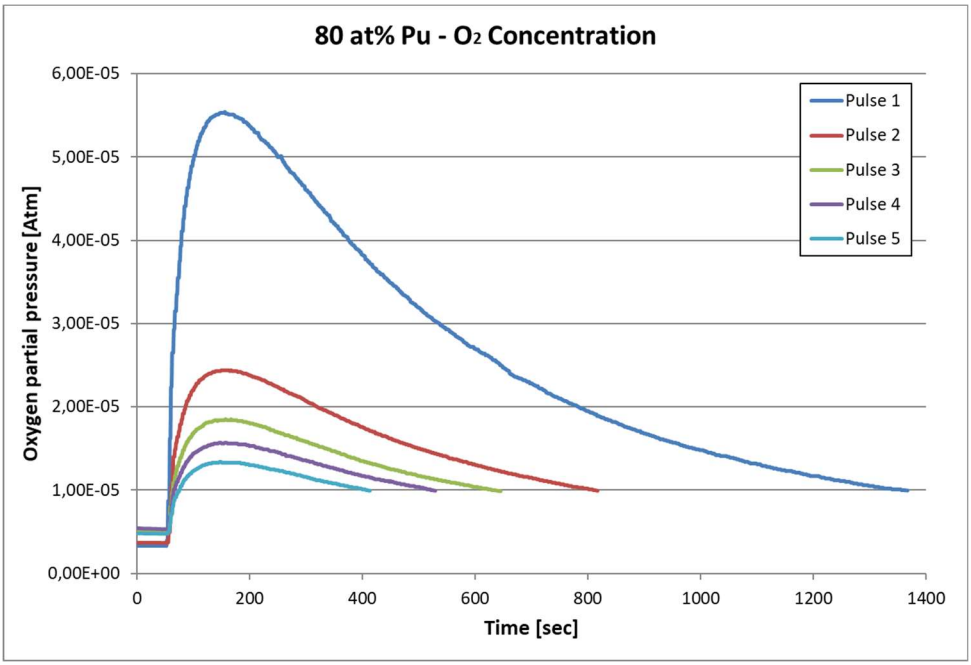

Figure A.23: Overall outgoing of the oxygen partial pressure after each laser pulse performed on the 80 at% Pu composition in argon.

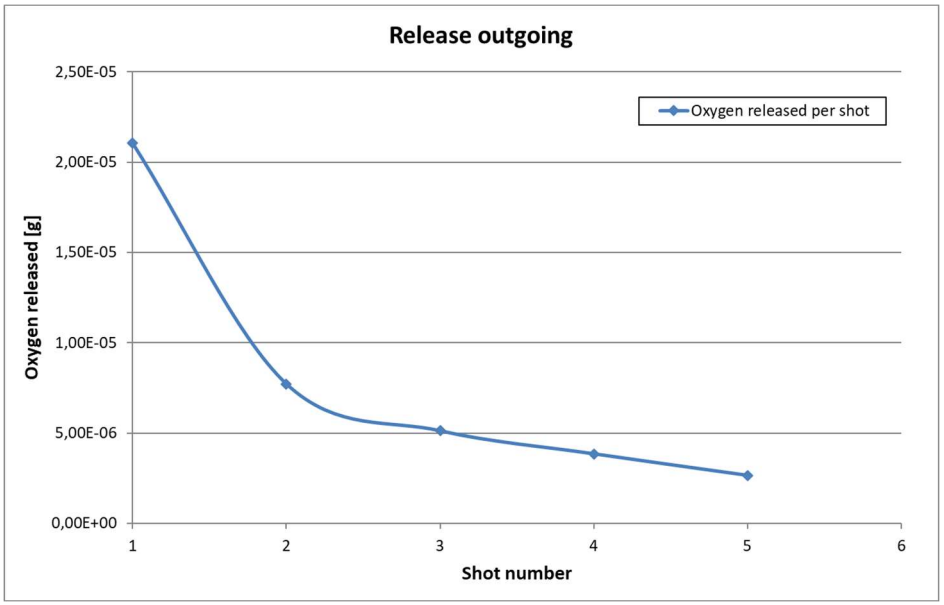

Figure A.24: General outgoing of the total amount of oxygen released by the sample following every laser shot, as expected this profile is following a pseudo-exponential behaviour, reaching an almost stationary value around 5 µg.

References

[1] N. T. G. Locatelli. M. Mancini, "Generation IV nuclear reactors: Current status and future prospects," *Energy policy,* vol. 61, 2013.

[2] e. a. D. Jacquemain, " Nuclear Power Reactor Core Melt Accidents. State of Knowledge," *EDP Science,* 2015.

[3] S. A. Bogatov, A. A. Borovoi, A. S. Lagunenko, E. M. Pazukhin and Strizhov, "Formation and spread of Chernobyl lavas Radiochemistry," *Khvoshchinski,* vol. 50, 2009.

[4] M. M.-F. D. M. T. w. B. C. C. B. P. L. V. R. P. Bottomley, "Investigations of the melting behaviour of the U–Zr–Fe–O system," *J. Nucl. Sci. Tech.,* vol. 52, pp. 1217-1225, 2015.

[5] S. B. e. al., " Phase diagram of the UO2-FeO1+x system," *J. Nucl. Mater.,* vol. 362, 2007.

[6] W. H. M. M. e. a. C. Ronchi, "A Universal Laser-Pulse Apparatus for Thermophysical Measurements in Refractory materials at very high temperatures," *International Journal of thermophysics,* vol. 20, 1999.

[7] R. B. K. B. e. a. Dario Manara, "The melting behaviour of oxide nuclear fuels: effects of the oxygen potential studied by laser heating," *Procedia Chemistry,* vol. 7, pp. 505-512, 2015.

[8] M. S. M. L. D. Manara, "Advances in Measurements of the Melting Transition in Non-Stoichiometric UO2," *International Journal of Thermophysics,* vol. 25, 2004.

[9] S. M. e. al, "Assessment of solid/liquid equilibria in the (U, Zr)O2+y system," *Journ. of Nuc. Mat.,* vol. 494, pp. 368-379, 2017.

[10] C. R. M. S. D. Manara, "Solidus and liquidus of UO2±x from high-pressure melting experiments,," *High Temperatures - High Pressures,* vol. 35/36, p. 25 – 33, 2003/2004.

[11] J. R. D.P. DeWitt, "Thermal radiative properties of materials," *Theory and Practice of Radiation Thermometry,* p. 91–187, 2007.

[12] D. M. C.M. Herzfeld, " Temperature: its measurement and control in science and industry," *Phys. Today* , vol. 317, p. 63, 2009.

[13] Kleykamp, "Phase equilibria in the UO2-austenitic steel system up to 3000°C," *Journal of nuclear materials,* vol. 247, 1997.

[14] S. Ushakov, B. Burakov, S. Shabalev and E. Anderson., "Interaction of UO2 and Zircaloy During the Chernobyl Accident," *Mater. Res. Soc. Symp.,* 1997.

[15] L. S. S. M. K. B. D. R. L. V. R. K. D. Manara, "Laser-heating and Radiance Spectrometry for the Study of Nuclear Materials in Conditions Simulating a Nuclear Power Plant Accident.," *J. Vis. Exp,* vol. 130, 2017.

[16] D. R. C. S. M. L. M. B. M. Manara, "Melting of stoichiometric and hyperstoichiometric uranium dioxide," *J. Nucl. Mater.,* vol. 342, p. 148–163, 2005.

[17] F. D. B. K. B. O. T. R. E. M. M. D. Manara, "High temperature radiance spectroscopy measurements of solid and liquid uranium and plutonium carbides," *J. Nucl. Mater.,* vol. 426, 2012.

[18] M. W. D. P. P. C. T. V. T. P. I. P. C. H. C. G. R. K. D. M. R. Böhler, "Recent advances in the study of the UO2–PuO2 phase diagram," *J. Nucl. Mater,* vol. 448, pp. 330-349., 2014.

[19] D. P. R. B. D. M. U. Carvajal-Nunez, "Melting point determination of uranium nitride and uranium plutonium nitride : A laser heating study," *J. Nucl. Mater.,* vol. 449, pp. 1-8, 2014.

[20] S. G. C. G. L. S. D. M. A. Quaini, "Laser heating investigation of the high-temperature interaction between zirconium and UO2," *J. Nucl. Mat.,* vol. 509, pp. 517-526, 2018.

[21] C. R. M. S. D. Manara, "Pressure Dependence of UO2 melting measured by Double-Pulse Laser Heating," *International Journal of Thermophysics,* vol. 23, 2002.

[22] A. C. V. C. J. N. B. e. a. Yvonne M. Mos, "X-Ray Diffraction of Iron Containing Samples: The Importance of a Suitable Configuration," *Geomicrobiology Journal,* vol. 35, 2018.

[23] B. M, "Spectral reflectivity and emissivity of solid and liquid UO2 as a function of wavelength, angle of incidence, and polarization," *High temperatures - high pressures,* vol. 12, 1980.

[24] L. V. D. S. e. a. T. Pavlov, "Experimental evaluation of the high temperature thermophysical properties of UO2," in *Top fuel*, Boise, 2016.

[25] R. P. M. S. D. Manara, "Advances in the Experimental Determination of the Uranium–Oxygen Phase Diagram at High Temperature," *International Journal of Thermophysics,* vol. 26, 2005.

[26] C. S. G. A. Quaini, "High temperature investigation of the solid/liquid transition in the PuO2-UO2-ZrO2 system," *Journ. of Nuc. Mat.,* vol. 467, 2015.

[27] K. B. D. M. e. a. Franck De Bruycker, "Reassessing the melting temperature of PuO2," *Materials today,* vol. 13, 2010.

[28] P. B. Coates, "Multy-wavelegth pyrometry," *Metrologia,* vol. 17, 1981.

[29] M. L. d. O. R. V. M. L. D. d. L. Flavio Costa Miguens, "A new protocol to detect light elements in estuarine sediments by X-ray microanalysis (SEM/EDS)," *Journ. of electron microscopy,* vol. 59, 2010.

[30] M. Y. Hiroaki OHFUJI, "EDS quantification of light elements using osmium surface coating," *Journ. of Mineralogical and petrological sciences,* vol. 110, 2015.